



DEVELOPMENT OF A DEEP CONVECTIVE CLOUD REFERENCE MODEL FOR VICARIOUS CALIBRATION

FINAL REPORT

Prepared by: Rayference

Date: 23/05/2017

Client: Eumetsat

Ref.: Rayference ITT 16_212841 Final Report V1.1

Document status

Validation of the EUMETSAT Geostationary Surface Albedo Climate Data Record - 2			
Issue	Revision	Date	Reason of the revision
0.0		09/02/2017	Original version
1.0		15/04/2017	First final version
1.1		23/05/2017	Final version

SOMMAIRE

1. INTRODUCTION.....	12
1.1. SCOPE OF THE DOCUMENT	12
1.2. APPLICABLE AND REFERENCE DOCUMENTS.....	12
2. DEFINITION OF DCC IDENTIFICATION CRITERIA	14
2.1. DEFINITION OF A SET OF CRITERIA	14
2.1.1. <i>Set of geographical conditions</i>	15
2.1.2. <i>Set of geophysical conditions</i>	16
2.1.2.1. Brightness temperature threshold	16
2.1.2.2. Spatial uniformity	16
2.1.3. <i>Set of geometrical conditions</i>	17
2.1.4. <i>Duration of the accumulation period</i>	18
2.2. SUMMARY OF THE IDENTIFICATION CRITERIA	18
3. DEFINITION AND VALIDATION OF A STANDARD DCC REFERENCE MODEL.....	19
3.1. OVERVIEW OF THE APPROACH	19
3.2. MOST RELEVANT PARAMETERS	20
3.2.1. <i>Cloud Optical Thickness</i>	20
3.2.2. <i>Ice crystal effective radius</i>	20
3.3. PROPOSED MICROPHYSICAL AND OPTICAL PARAMETER VALUES.....	20
3.4. DCC RM SENSITIVITY ANALYSIS.....	21
3.4.1. <i>Experimental Setup</i>	21
3.4.2. <i>Sensitivity to COT</i>	21
3.4.3. <i>Sensitivity to effective radius</i>	26
3.4.4. <i>Sensitivity to surface reflectance</i>	32
3.4.5. <i>Sensitivity to ozone</i>	35
3.4.6. <i>FCI sensitivity analysis</i>	36
3.4.6.1. Experimental setup.....	36
3.4.6.2. Sensitivity to Cloud Top Height.....	36
3.4.6.3. Water vapour content	38
3.4.7. <i>Analysis of the actual observation conditions</i>	39
4. ALGORITHM CONCEPT	42
4.1. IDENTIFICATION PROCESS OF THE DCC PIXELS	42
4.2. CONSTRUCTION OF THE HISTOGRAMS	42
4.3. (HR)VIS BAND CONSIDERATION	43
4.4. SETUP PARAMETERS	45
5. CONSISTENCY ANALYSIS AND EVALUATION	46
5.1. EXPERIMENTAL SETUP.....	46
5.2. SENSITIVITY ANALYSIS TO THE IDENTIFICATION CRITERIA.....	46
5.2.1. <i>DCC identification criteria</i>	46
5.2.1.1. Brightness temperature threshold	46
5.2.1.2. Latitude Coverage: Rapid Scan Mode.....	50
5.2.2. <i>DCC RM parameters</i>	52
5.2.2.1. Cloud Optical Thickness.....	52
5.2.2.2. Effective Radius.....	56
6. SYSTEMATIC ALGORITHM EVALUATION	60
6.1. EFFECT OF HRVIS SCANNING MODE	60
6.2. TIME SERIES	65
6.2.1. <i>Meteosat-7 data (IODC/ZDS)</i>	65
6.2.1.1. ZDS (2005).....	65
6.2.1.2. IODC (2007).....	66
6.2.2. <i>Meteosat-8 data (IODC/ZDS)</i>	67
6.2.2.1. ZDS (2005).....	67
6.2.2.2. IODC (2016 - 2017).....	70

6.2.3. *Meteosat-10 data (ZDS – Land and Sea)* 72

6.3. COMPARISON WITH OTHER SSCC TARGETS 75

6.3.1. *Overview*..... 75

6.3.2. *Accuracy of the Libya-4 TOA radiance simulations*..... 75

6.3.3. *Results*..... 82

7. TOWARDS INTEGRATION IN THE VICARIOUS CALIBRATION SYSTEM SSCC84

8. RECOMMENDATIONS AND WAY FORWARD86

8.1. OVERVIEW 86

8.2. FURTHER IMPROVEMENTS OF THE DCC METHOD 86

8.3. INTEGRATION WITHIN SSCC 87

8.4. POTENTIAL SSCC IMPROVEMENTS 87

List of Figures

Figure 1 - Mean location of the ITCZ in January (blue) and July (red) (Source: Wikipedia, after Mats Halldin) 14

Figure 2 – Location of the sea (blue) and land (red) DCC pixel search areas over the ZDS (left) and IODC (Meteosat-7) areas. The green diamond indicates the location of the sup-satellite point..... 15

Figure 3 - Brightness temperature of MODIS products identified as DCC, from various geographic zones. Source: [DR5]. 16

Figure 4 - DCC effective radius and optical thickness vertical profile after [DR5]. Ice crystals are shown in red and water droplet in blue. 19

Figure 5 - Effective radius of the same MODIS products from Africa (in red), South America (in blue), Western Pacific over land (in dotted black) and Western Pacific over ocean (in solid black) - Source: [DR5]..... 20

Figure 6 - Top Of Atmosphere Bi-Directional Factor in the Principal Plane for Meteosat 10 band, VIS0.6, with different COT on land, at a fixed effective radius of 23 μ m. The vertical dotted line is the zenithal sun angle at 25°, while the solid lines mark maximal viewing zenithal angle allowed. 22

Figure 7 - Same as Figure 6, in the band VIS0.8..... 23

Figure 8 - Same as Figure 6, in the band NIR1.6..... 23

Figure 9 - Same as Figure 6, in the band HRVIS. 24

Figure 10 - Top Of Atmosphere Bi-Directional Factor in the Principal Plane for Meteosat 10 band, VIS0.6, with different COT on sea, at a fixed effective radius of 25 μ m. The vertical dotted line is the zenithal sun angle at 25°, while the solid lines mark maximal viewing zenithal angle allowed. 25

Figure 11 - Same as Figure 10, in the band VIS0.8..... 25

Figure 12 - Same as Figure 10, in the band NIR1.6..... 26

Figure 13 - Same as Figure 10, in the band HRVIS. 26

Figure 14 - Top Of Atmosphere Bi-Directional Factor in the Principal Plane for Meteosat 10 band, VIS0.6, with different effective radii on land, at a fixed COT of 100. The vertical dotted line is the zenithal sun angle at 25°, while the solid lines mark maximal viewing zenithal angle allowed. 27

Figure 15 - Same as Figure 14, in the band VIS0.8..... 28

Figure 16 - Same as Figure 14, in the band NIR1.6..... 28

Figure 17 - Same as Figure 14, in the band HRVIS. 29

Figure 18 - Top Of Atmosphere Bi-Directional Factor in the Principal Plane for Meteosat 10 band, VIS0.6, with different effective radii on sea, at a fixed COT of 100. The vertical dotted line is the zenithal sun angle at 25°, while the solid lines mark maximal viewing zenithal angle allowed. 30

Figure 19 - Same as Figure 18, in the band VIS0.8..... 30

Figure 20 - Same as Figure 18, in the band NIR1.6..... 31

Figure 21 - Same as Figure 18, in the band HRVIS. 32

Figure 22 - Top Of Atmosphere Bi-Directional Factor in the Principal Plane for Meteosat 10 band, VIS 0.6, with two different kinds of surface: land (red) and sea (orange). The vertical dotted line is the zenithal sun angle at 25°, while the solid lines mark the maximal viewing zenithal angle allowed..... 33

Figure 23 - Same as Figure 22, for the band VIS0.8..... 33

Figure 24 - Same as Figure 22, for the band NIR1.6. 34

Figure 25 - Same as Figure 22, in the HRVIS band. 34

Figure 26 - Top Of Atmosphere Bi-Directional Factor in the Principal Plane for Meteosat 10 band, VIS0.6, with different values of the ozone total column concentration. The vertical dotted line is the zenithal sun angle at 25°, while the solid lines mark maximal viewing zenithal angle allowed. 35

Figure 27 - Top Of Atmosphere Bi-Directional Factor in the Principal Plane for MTG1 band, VIS0.4, with different values for the cloud top height. The vertical dotted line is the zenithal sun angle at 25°, while the solid lines mark maximal viewing zenithal angle allowed. 37

Figure 28 – Same as Figure 27, for MTG1 band, VIS0.5..... 37

Figure 29 – Same as Figure 27, for MTG1 band, VIS0.6..... 38

Figure 30 - Top Of Atmosphere Bi-Directional Factor in the Principal Plane for Meteosat MTG1 band, NIR1.3, with different values for the total amount of water vapour in the atmospheric column. The vertical dotted line is the zenithal sun angle at 25°, while the solid lines mark maximal viewing zenithal angle allowed. 39

Figure 31: Distribution of the SZA and VZA values for the DCC pixels contributing to the calibration of MSG3 between 2013 and 2015. Red (blue) curve shows the DCC pixels identified over land (sea). 40

Figure 32 – Example of accumulated calibration coefficient histograms for Meteosat-10 over land for period 116 – 120 in 2013. The blue line indicates all the accumulated pixels, the red line the fitted Gaussian curve on this histogram, the green lines shows the pixels that fulfil the multi-spectral conditions and the orange curve the fitted Gaussian of the multi-spectral population. 43

Figure 33 – Example of HRVIS acquisition mode for slot 48 (12h) acquired 01/06/2013 by Meteosat-10..... 44

Figure 34 - Calibration coefficient computed with Meteosat 10 data of the first 6 months of 2013, over the ZDS region, on land, in the VIS 0.6 band. The following colour code is used: 205K (red), 200K (coral), 195K (orange), 190K (yellow). The black horizontal dashed line gives the value of the calibration coefficient as obtained Libya-4 CEOS PICS for comparison purposes. The dotted lines represent the uncertainties associated with this reference value, within a 3% margin. 47

Figure 35 – Same as Figure 34, in the VIS 0.8 band. 47

Figure 36 - Same as Figure 34, in the NIR 1.6 band. 48

Figure 37 - Same as Figure 34, in the HRVIS band. 48

Figure 38 - Calibration coefficient computed with Meteosat 10 data of the first 6 months of 2013, over the ZDS region, on sea, in the VIS 0.6 band for threshold brightness temperature varying from 205K to 190K by step of 5K. The lighter the blue, the colder the threshold temperature. The black horizontal dashed line is mean calibration coefficient obtained over Libya-4 CEOS PICS. The dotted lines represent the $\pm 3\%$ uncertainties. 49

Figure 39 – Same as Figure 38, in the VIS 0.8 band. 49

Figure 40 - Same as Figure 38, in the NIR1.6 band. 50

Figure 41 - Same as Figure 38, in the HRVIS band. 50

Figure 42 - Calibration coefficient computed with Meteosat 10 data of the years 2013, 2014, 2015, over the ZDS region and the Rapid Scan Mode area, on land, in the VIS0.6 band. Red curve: normal acquisition mode, yellow : rapid scan acquisition area. The black horizontal dashed line is mean calibration coefficient obtained over Libya-4 CEOS PICS. The dotted lines represent the $\pm 3\%$ uncertainties. 51

Figure 43 – Same on Figure 42, in the VIS0.8 band. 51

Figure 44 - Same on Figure 42, in the NIR1.6 band. 52

Figure 45 - Same on Figure 42, in the HRVIS band. 52

Figure 46 - Calibration coefficient computed with Meteosat 10 data of the first 6 months of 2013, over the ZDS region, on land, in the VIS0.6 band. The following colour code is used: COT = 80 (light brown), COT = 100 (red), COT = 120 (dark brown). The black horizontal dashed line is mean calibration coefficient obtained over Libya-4 CEOS PICS. The dotted lines represent the $\pm 3\%$ uncertainties. 53

Figure 47 – Same as Figure 46, in the VIS0.8 band. 53

Figure 48 – Same as Figure 46, in the NIR1.6 band. 53

Figure 49 - Same as Figure 46, in the HRVIS band. 54

Figure 50 - Calibration coefficient computed with Meteosat 10 data of the first 6 months of 2013, over the ZDS region, on sea, in the VIS0.6 band. The following colour coding is used: COT =80 (cyan), COT = 100 (blue) COT = 120 (navy blue). The black horizontal dashed line is mean calibration coefficient obtained over Libya-4 CEOS PICS. The dotted lines represent the $\pm 3\%$ uncertainties. 54

Figure 51 – Same as Figure 50, in the VIS0.8 band. 55

Figure 52 – Same as Figure 50, in the NIR1.6 band. 55

Figure 53 - Same as Figure 50, in the HRVIS band. 56

Figure 54 - Calibration coefficient computed with Meteosat 10 data of the first 6 months of 2013, over the ZDS region, on land, in the VIS0.6 band. 56

Figure 55 – Same as Figure 54, in the VIS0.8 band. 57

Figure 56 - Same as Figure 54, in the NIR1.6 band. 57

Figure 57 - Same as Figure 54, in the HRVIS band. 57

Figure 58 - Calibration coefficient computed with Meteosat 10 data of the first 6 months of 2013, over the ZDS region, on sea, in the VIS0.6 band. 58

Figure 59 – Same as Figure 58, in the VIS0.8 band. 58

Figure 60 - Same as Figure 58, in the NIR1.6 band. 59

Figure 61 - Same as Figure 58, in the HRVIS band. 59

Figure 62 - Times series for the calibration coefficient of Meteosat 10, using land-borne DCCs, in the band VIS0.6, during the year 2013. The red points are the calibration coefficients computed with the mutli-spectral test activated in the VIS0.6, VIS0.8 and NIR1.6, while the yellow points are computed with a spectral filtering activated in all 4 bands (VIS0.6, VIS0.8, NIR1.6 and HRVIS). The black horizontal dashed line is mean calibration coefficient obtained over Libya-4 CEOS PICS. The dotted lines represent the $\pm 3\%$ uncertainties. 61

Figure 63 - Same as Figure 62, in the band VIS0.8. 61

Figure 64 - Same as Figure 62, in the band NIR1.6. 62

Figure 65 - Same as Figure 62, in the band HRVIS. 62

Figure 66 - Times series for the calibration coefficient of Meteosat 10, using sea-borne DCCs, in the band VIS0.6, during the year 2013. The dark green points are the calibration coefficients computed with the mutli-spectral test activated in the VIS0.6, VIS0.8 and NIR1.6, while the light green points are computed with a spectral filtering activated in all 4 bands (VIS0.6, VIS0.8, NIR1.6 and HRVIS). The black horizontal dashed line is mean calibration coefficient obtained over Libya-4 CEOS PICS. The dotted lines represent the $\pm 3\%$ uncertainties..... 63

Figure 67 - Same as Figure 66, in the band VIS0.8..... 64

Figure 68 - Same as Figure 66, in the band NIR1.6..... 64

Figure 69 - Same as Figure 66, in the band HRVIS..... 64

Figure 70 - Positions of the selected pixels during winter. Dark green pixels are acquired without filtering in the HRVIS band, while light green pixels are selected with the 4-bands filtering. 65

Figure 71 - Positions of the selected pixels during summer. Dark green pixels are acquired without filtering in the HRVIS band, while light green pixels are selected with the 4-bands filtering. 65

Figure 72: Calibration coefficient in $Wm^{-2}sr^{-1}\mu m^{-1}/DC$ for Meteosat-7 VIS band derived in 2005 over land (red) and ocean (blue)..... 66

Figure 73: Same as Figure 72 but for year 2007..... 67

Figure 74: Localization of the identified DCC pixels in January – June 2007 (magenta) and July – December 2007 (orange). The search area is indicated in red and the sub-satellite point in green..... 67

Figure 75: Calibration coefficient in $Wm^{-2}sr^{-1}\mu m^{-1}/DC$ for Meteosat-8 VIS0.6 band derived in 2005 over land (red) and ocean (blue). The black horizontal dashed line is mean calibration coefficient obtained over Libya-4 CEOS PICS. The dotted lines represent the $\pm 3\%$ uncertainties..... 69

Figure 76: Calibration coefficient in $Wm^{-2}sr^{-1}\mu m^{-1}/DC$ for Meteosat-8 VIS0.8 band derived in 2005 over land (red) and ocean (blue). The black horizontal dashed line is mean calibration coefficient obtained over Libya-4 CEOS PICS. The dotted lines represent the $\pm 3\%$ uncertainties..... 69

Figure 77: Calibration coefficient in $Wm^{-2}sr^{-1}\mu m^{-1}/DC$ for Meteosat-8 NIR1.6 band derived in 2005 over land (red) and ocean (blue). The black horizontal dashed line is mean calibration coefficient obtained over Libya-4 CEOS PICS. The dotted lines represent the $\pm 3\%$ uncertainties..... 69

Figure 78: Calibration coefficient in $Wm^{-2}sr^{-1}\mu m^{-1}/DC$ for Meteosat-8 HRVIS band derived in 2005 over land (red) and ocean (blue). The black horizontal dashed line is mean calibration coefficient obtained over Libya-4 CEOS PICS. The dotted lines represent the $\pm 3\%$ uncertainties..... 70

Figure 79: Calibration coefficient in $Wm^{-2}sr^{-1}\mu m^{-1}/DC$ for IODC Meteosat-8 VIS0.6 band derived during the Sept. 2016 – March 2017 period over land (red) and ocean (blue)..... 71

Figure 80: Calibration coefficient in $Wm^{-2}sr^{-1}\mu m^{-1}/DC$ for IODC Meteosat-8 VIS0.8 band derived during the Sept. 2016 – March 2017 period over land (red) and ocean (blue)..... 71

Figure 81: Calibration coefficient in $Wm^{-2}sr^{-1}\mu m^{-1}/DC$ for IODC Meteosat-8 NIR1.6 band derived during the Sept. 2016 – March 2017 period over land (red) and ocean (blue)..... 72

Figure 82: Calibration coefficient in $Wm^{-2}sr^{-1}\mu m^{-1}/DC$ for IODC Meteosat-8 HRVIS band derived during the Sept. 2016 – March 2017 period over land (red) and ocean (blue)..... 72

Figure 83 - Calibration coefficient in $Wm^{-2}sr^{-1}\mu m^{-1}/DC$ for Meteosat-10 VIS0.6 band derived in 2013-2015 over land (red) and ocean (blue). The black dashed line gives the value of the mean calibration coefficient obtained over Libya-4 CEOS PICS. The dotted lines represent the $\pm 3\%$ uncertainties. 73

Figure 84 – Same as Figure 83, for the VIS0.8 band. 73

Figure 85 - Same as Figure 83, in the NIR1.6 band. 74

Figure 86 - Same as Figure 68, in the HRVIS band. 74

Figure 87: Mean ratio between ACQUA/MODIS observations acquired over Libya4 between 2006 and 2009 and simulations as a function of the viewing directions. Top panel: sun zenith angles in the 0 – 30° interval. Bottom panel : sun zenith angles in the 30 – 60° interval..... 76

Figure 88: Same as Figure 87 but for MERIS observations. 77

Figure 89 - Total gaseous transmittance within the 0.4 – 1.1 μm spectral region. 78

Figure 90: Comparisons with GOME 2b band -3 and -4 (black) and simulation (green). Top panel: TOA BRF. Medium Panel: relative bias between observations and simulations in per cent. Bottom panel: Standard deviation of the relative bias in percent. 80

Figure 91: Details of molecular transmittance in the 560 – 585nm spectral interval..... 81

Figure 92: Overall relative bias between observations and simulations for MODIS (red), MERIS (blue) AND GOME-2b (green). Illumination and viewing zenith angles are restricted to a maximum value of 40°. 81

Figure 93 – Example of overall scatterplot of MSG3 count values against simulated radiances in band VIS0.6 (blue), VIS0.8 (green), NIR1.6 (green) and HRVIS (violet) for Meteosat-10 in 2013 for day-of-the-year 116-120. The slope provides the calibration coefficient expressed in $Wm^{-2}\mu m^{-1}sr^{-1}/DC$ over sea, Libya-4 and DCC. In the NIR band, count values over Libya-4 exceed the DCC values. 82

Figure 94: SSCC overall flowchart. 84

List of Tables

<i>Table 2-1 - Literature review of the set of geographical conditions and acquisition time.....</i>	<i>15</i>
<i>Table 2-2 - Literature review of the brightness temperature threshold used</i>	<i>16</i>
<i>Table 2-3 - Literature review of the spatial uniformity criteria used</i>	<i>17</i>
<i>Table 2-4 - Literature review of the angular range restriction</i>	<i>17</i>
<i>Table 2-5 - Literature review of the temporal criteria used.....</i>	<i>18</i>
<i>Table 2-6 Identification criteria and their values in this study.....</i>	<i>18</i>
<i>Table 3-1 Literature review of the microphysical parameters used in various DCC reference models</i>	<i>21</i>
<i>Table 3-2 - Comparison of TOA BRF in the principal plane for different values of the COT, from 80 to 120.</i>	<i>22</i>
<i>Table 3-3 - Comparison of TOA BRF in the principal plane for different values of the COT 80 to 120.</i>	<i>24</i>
<i>Table 3-4 - Comparison of TOA BRF in the principal plane for different values of the effective radius at 18, 23 and 28µm.</i>	<i>27</i>
<i>Table 3-5 – Comparison of TOA BRF in the principal plane for different values of the effective radius at 20, 25 and 30µm.</i>	<i>29</i>
<i>Table 3-6 - Comparison of TOA BRF in the principal plane for different surface types, with a COT at 100 and an effective radius of 25µm</i>	<i>32</i>
<i>Table 3-7 – Comparison of TOA BRF in the principal plane for different amounts of ozone in the atmosphere, with a COT at 100 and an effective radius of 23µm, over land.</i>	<i>35</i>
<i>Table 3-8 – Comparison of TOA BRF in the principal plane for two cloud top heights, with a COT at 100 and an effective radius of 23µm, over land.....</i>	<i>36</i>
<i>Table 3-9 - Comparison of TOA BRF in the principal plane for different amounts of water vapour in the atmosphere, with a COT at 100 and an effective radius of 23µm, over land</i>	<i>38</i>
<i>Table 3-10: Relative uncertainties due to an uncertainty of ±5µm for the radius and ±20 for the COT accounting for the actual observation geometry for DCC identification during the 2013-2015 period.....</i>	<i>40</i>
<i>Table 6-1 - List of data on which the DCC identification will be applied in the framework of this study.....</i>	<i>60</i>
<i>Table 6-2: Mean relative difference between the calibration coefficient derived with and without the use of the HRVIS band in the multi-spectral filtering.</i>	<i>62</i>
<i>Table 6-3 – Comparison of DCC calibration results derived of sea, Libya-4 and DCC for Meteosat-10 in 2013 for day-of-the-year 116-120. Calibration coefficients are given in $Wm^{-2}\mu m^{-1}sr^{-1}/DC$. The offset column provides the retrieved space count value.</i>	<i>83</i>

List of Acronyms

AOT	Aerosol Optical Thickness
ASD	Algorithm Specification Document
AVHRR	Advanced Very High Resolution Radiometer
BRF	Bidirectional Reflectance Factor
COT	Cloud Optical Thickness
DC	Digital Count
DCC	Deep Convective Clouds
ECMWF	European Centre for Medium range Weather Forecasts
HRVIS	High Resolution Visible
IODC	Indian Ocean Data Coverage
IR	Infra-Red
ITCZ	Inter-Tropical Convergence Zone
LUT	Look-up Table
MARF	Meteorological Archive Retrieval Facility
MARS	Meteorological Archive and Retrieval System
MPEF	Meteorological Product Extraction Facility
MHM	Modified Hapke Model
MSG	Meteosat Second Generation
MTP	Meteosat Transition Programme
NIR	Near-Infrared
OOR	Out-Of-Range
PICS	Pseudo-Invariant Calibration Sites
PP	Principal Plane
RM	Reference Model
RT	Radiative Transfer
RTM	Radiative Transfer Model
SAA	Sun Azimuth Angle
SEVIRI	Spinning Enhanced Visible and Infrared Imager
SoW	Statement of Work
SSP	Sub-Satellite Point
SSCC	SEVIRI Solar Channel Calibration
SSR	Sensor Spectral Response
SZA	Sun Zenith Angle
TOA	Top of Atmosphere
TOMS	Total Ozone Mapping Spectrometer
VAA	View Azimuth Angle
VIS	VISible
VZA	View Zenith Angle
WP	Working Package
ZDS	Zero-Degree Service
TBC	To Be Completed
TBD	To Be Defined

1. INTRODUCTION

1.1. SCOPE OF THE DOCUMENT

This document presents the progresses of the Development of a Deep Convective Cloud Reference Model For Vicarious Calibration for the Mid-Term Review. This report covers the following WPs:

- WP1 : Definition of DCC identification criteria (Section 2);
- WP2 : Definition and validation of a standard DCC RM (Section 3);
- WP3 : Consistency analysis and evaluation (Sections 4 to 6);
- WP4 : Towards integration in the vicarious calibration system SSCC (Section 7);
- WP5 : Recommendation and way forward.

The ASD has been updated in a separate document.

1.2. APPLICABLE AND REFERENCE DOCUMENTS

N°	Reference	Title
[DA1]	EUM/RSP/SOW/16/855480 v1, 29 April 2016	Statement of Work: Development of a Deep Convective Cloud Reference Model for Vicarious Calibration
[DA2]	EUM/COS/STC/16/863103 v1, 28 June 2016	Special Tender Conditions
[DA3]	RD1	Operational Calibration of the Meteosat Radiometer VIS Band, 2004, IEEE Transactions on Geoscience and Remote Sensing, 42, 1900
[DA4]	RD2	GSICS ATBD for Deep Convective Cloud technique of calibrating GEO sensors with Aqua-MODIS August 19, 2011
[DA5]	RD3	SEVIRI Solar Channel Calibration – Algorithm Specification Document, EUM/MSG/SPE/411, Version 3, 27.05.2014

N°	Reference
[DR1]	Baum, B. A., Yang, P., Heymsfield, A. J., Bansemmer, A., Merrelli, A., Schmitt, C., and Wang, C.: Ice cloud bulk single-scattering property models with the full phase matrix at wavelengths from 0.2 to 100 μm , J. Quant. Spectrosc. Radiat. Transfer, special Issue ELS-XIV, 2014.
[DR2]	Govaerts, Y. M., A. Arriaga, and J. Schmetz. 2001. "Operational Vicarious Calibration of the MSG/SEVIRI Solar Channels." <i>Adv. Space Res.</i> 28 (1): 21–30.
[DR3]	Govaerts, Yves, S. Sterckx, and Stefan Adriaensen. 2013. "Use of Simulated Reflectances over Bright Desert Target as an Absolute Calibration Reference." <i>Remote Sensing Letters</i> , 523–31. doi:10.1080/2150704X.2013.764026.

[DR4]	Govaerts, Yves, S. Sterckx, and Stefan Adriaensen. 2013. "Use of Simulated Reflectances over Bright Desert Target as an Absolute Calibration Reference." <i>Remote Sensing Letters</i> , 523–31. doi:10.1080/2150704X.2013.764026.
[DR5]	Sohn, B.-J., M.-J. Choi, and J. Ryu. 2015. "Explaining Darker Deep Convective Clouds over the Western Pacific than over Tropical Continental Convective Regions." <i>Atmos. Meas. Tech.</i> 8 (11): 4573–85. doi:10.5194/amt-8-4573-2015.
[DR6]	P. Minnis, D. R. Doelling, L. Nguyen, W. Miller, and V. Chakrapani, "Assessment of the visible channel calibrations of the TRMM VIRS and MODIS on Aqua and Terra," <i>J. Atmos. Ocean. Technol.</i> , vol. 25, no. 3, pp. 385–400, 2008
[DR7]	B. J. Sohn, S.-H. Ham, and P. Yang, "Possibility of the visible-channel calibration using deep convective clouds overshooting the TTL," <i>J. Appl. Meteorol. Climatol.</i> , vol. 48, no. 11, pp. 2271–2283, Nov. 2009
[DR8]	Y. B. Hu, B. A. Wielicki, P. Yang, P. W. Stackhouse, Jr., B. Lin, and D. F. Young, "Application of deep convective cloud albedo observation to satellite-based study of the terrestrial atmosphere: Monitoring the stability of spaceborne measurements and assessing absorption anomaly," <i>IEEE Trans. Geosci. Remote Sens.</i> , vol. 42, no. 11, pp. 2594–2599, Nov. 2004.
[DR9]	D. R. Doelling, D. Morstad, B. R. Scarino, R. Bhatt, A. Gopalan, "The characterization of deep convective clouds as an invariant calibration target and as a visible calibration technique", <i>IEEE Trans. Geosci. Remote Sens.</i> , vol. 51, no. 3, pp. 1147-1159, Mar. 2013.
[DR10]	G.-Y. Yang and J. Slingo, "The Diurnal Cycle in the Tropics", <i>Monthly Weather Review</i> , vol. 129, issue 4, p. 784, Aug. 2001.
[DR11]	Graybill, F.A., and R.B. Deal. "Combining Unbiased Estimators" 15 (1959): 543–50.

2. DEFINITION OF DCC IDENTIFICATION CRITERIA

2.1. DEFINITION OF A SET OF CRITERIA

This Section discusses the outcome of WP1 dedicated to the definition of DCC identification criteria. The approach to define criteria leading to the correct identification of Deep Convective Clouds (DCCs) is based on literature review, using the studies of Sohn et al. (2015), Minnis et al. (2008), Sohn et al. (2009), Hu et al., (2004) and finally Doelling et al. (2013), as well as existing work performed in the framework of the FIDUCEO (www.fiduceo.org) study and [DR2].

The capability to identify within the Meteosat images pixels that correspond to the DCC Reference Model (RM) represents a fundamental aspect of SSCC principles. By order of importance, these criteria are:

1. The identification is the latitudinal coverage, which is centred on the Equator where most DCCs are formed along the Inter-Tropical Convergence Zone (ITCZ);
2. The threshold temperature used in the thermal infrared band;
3. The uniformity and size of the extracted area;
4. The illumination and observation geometry. To minimize angular, i.e., Bidirectional Reflectance Factor (BRF) effects, the range of acceptable Sun and Viewing Zenith Angles (SZA and VZA) will be limited.
5. The duration of the accumulation period.

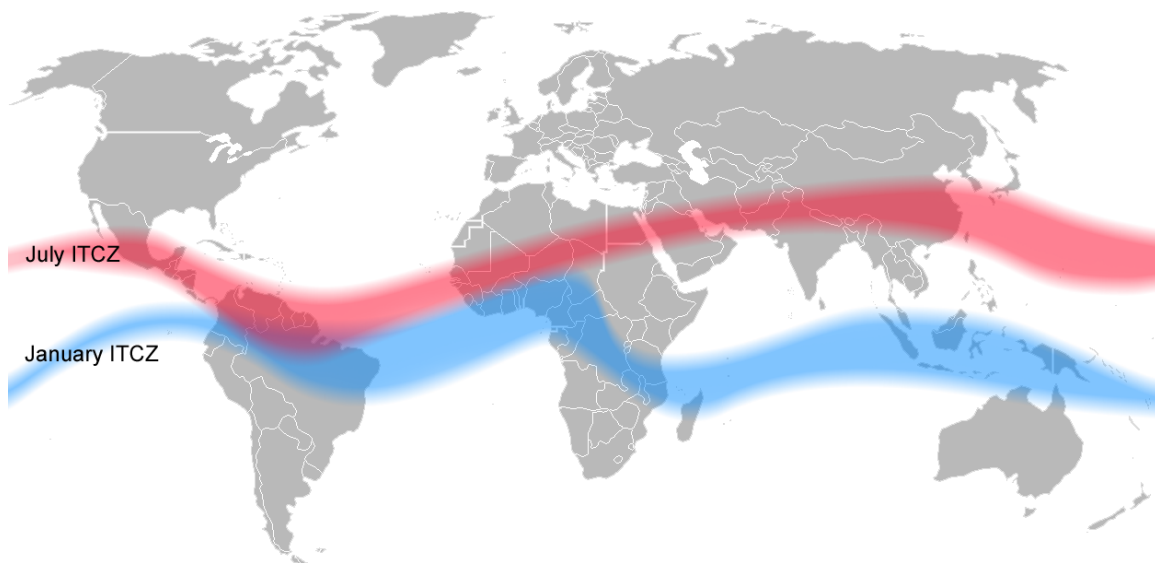


Figure 1 - Mean location of the ITCZ in January (blue) and July (red) (Source: Wikipedia, after Mats Halldin)

2.1.1. Set of geographical conditions

Article	Geographic zone	Latitude/Longitude	Local Time
[DR5]	Africa South America Western Pacific (Land/Ocean)	20°N-20°S, 0-40°E 10°N-30°S, 40°-70°W 20°N-20°S, 100°-180°E	13h30
[DR6]	Ocean	30°N-30°S	-
[DR7]	Tropical ocean and land - ITCZ	30°N-30°S, 90°W-90°E	10h
[DR8]	Tropical Zone	-	-
[DR9]	Tropical ocean and land - ITCZ	30°N-30°S	10h
GSICS		20°N-20°S/according to SPP	12h +/- 2h

Table 2-1 - Literature review of the set of geographical conditions and acquisition time.

DCCs are common in the Inter-Tropical Convergence Zone (ITCZ) – over land and ocean, mainly over the tropical western pacific and equatorial Africa (Figure 1). However, the localisation of the convergence zone varies with the seasons through the year. Over land, ITCZ moves from one side to the other of the equator and back, following the sun’s zenith point. Over sea, the convection is constrained by the distribution of ocean temperature. Consequently, different sets of microphysical properties are used over land and sea pixel as can be seen on Figure 5.

In order to perform calibration over DCC targets all-year round, the temporal window for SEVIRI slot acquisition is centred on the local noon, with a 4-hour range - while the morning slots provide the most active DCC population – as pointed out in the study of [DR10]. Typical geographical conditions used in the reviewed literature are listed in Table 2-1. The areas in which potential DCC pixels are identified in this study over the Zero Degree Service (ZDS) and IODC are shown on Figure 2.

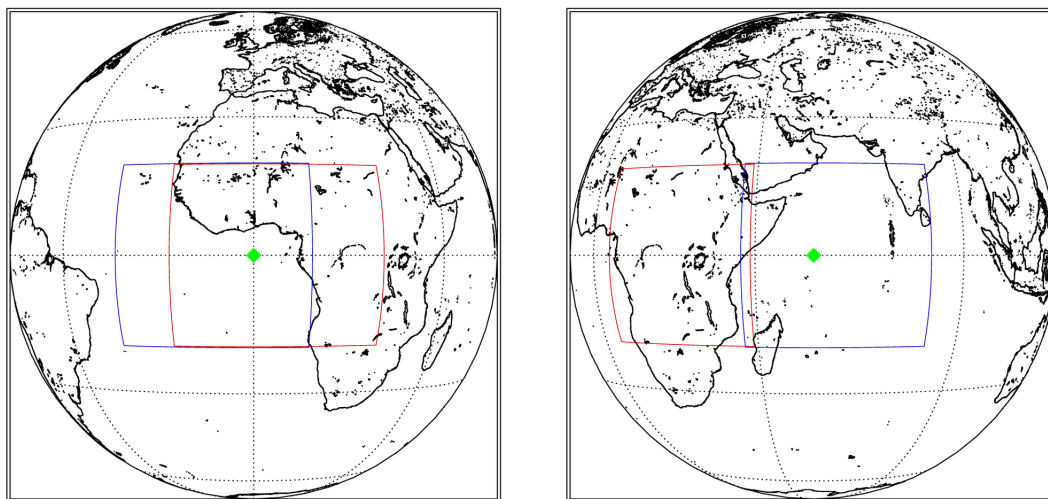


Figure 2 – Location of the sea (blue) and land (red) DCC pixel search areas over the ZDS (left) and IODC (Meteosat-7) areas. The green diamond indicates the location of the sup-satellite point.

It should be noted that the definition of geographical conditions also put constraints on the maximal viewing zenithal angle range (Section 2.1.3). A reduced geographical coverage will be used for the calibration of the data acquired for the Rapid Scan Service, from 30° to 15°, and therefore, will only acquire data during the northern summer.

2.1.2. Set of geophysical conditions

2.1.2.1. Brightness temperature threshold

The DCC tops are the coldest targets in the tropics, since they reach the tropopause level.

Article	Temperature Threshold (in K)
[DR5]	190 + CloudSat mask
[DR6]	205
[DR7]	190
[DR8]	205
[DR9]	205-195
GSICS	205 (1)
This study	205

Table 2-2 - Literature review of the brightness temperature threshold used.
(1) In GSICS this temperature is adjusted to account for some residual biases.

Since DCCs over ocean appear to be slightly warmer than land-borne DCCs, as shown on the Figure 3 extracted from the study [DR5], it seems logical to set the temperature threshold at a value slightly above 200K – this less restrictive threshold is therefore suitable for both land and sea pixels. However, this criterion alone cannot be sufficient to discriminate DCCs from other kinds of cloud, like cirrus and anvils. It should be stressed here that Figure 3 is representative of the month of January between 2007 and 2010.

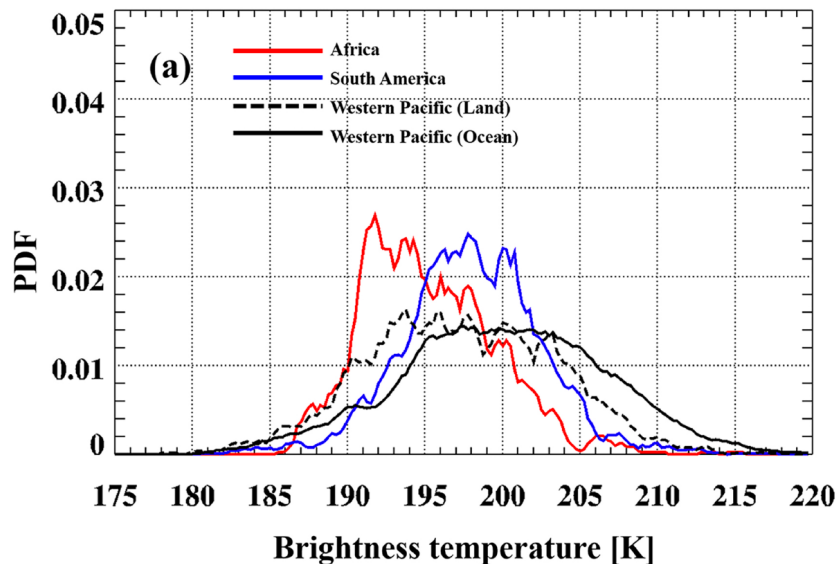


Figure 3 - Brightness temperature of MODIS products identified as DCC, from various geographic zones. Source: [DR5].

2.1.2.2. Spatial uniformity

The previous studies reviewed in this WP rely on different sensors, whose spatial resolution is different. Yet there is a consensus on the scale of the window used which is several kilometre-wide, centred on the targeted pixel. The criterion insuring the spatial uniformity is a threshold on the ratio of the standard deviation of the window over its averaged radiance value should be lower than a given percentage, ensuring that the pixel is not part of a thinner kind of cloud or present on the border of a DCC.

Article	Spatial extension	Reflectance	Temperature Standard Deviation
[DR5]	3*3 MODIS pixels	?	?
[DR6]		2%	1K
[DR7]	9*9 MODIS pixels	3%	1K
[DR8]			
[DR9]	3*3	3% in VIS	1K in IR
GSICS	3*3	3% in VIS	1K
This study	5*5	2% in every filtered band	0.5K

Table 2-3 - Literature review of the spatial uniformity criteria used

This uniformity is enforced in all spectral bands, including the infra-red, where the uniformity condition translated as a constraint on the standard deviation of the considered area, which should be lower than a given temperature threshold.

2.1.3. Set of geometrical conditions

Close to nadir, DCCs are almost Lambertian, i.e., near isotropic, targets. Restraining the angular ranges for the viewing and solar zeniths during the identification process of the calibration pixels ensures the limitation of uncertainties related to the assumption of a 1-D plane parallel atmosphere for the simulation of DCC reflectance. Outside that range, 3-D effects arising from the curvature of the Earth become too important to be negligible. This study relies thus on a maximum sun and viewing zenith angle of 30°. In most of the cases, enough DCC are observed within these limits, reducing thereby any issues related to 3D effects.

Article	Viewing Zenithal Angle (VZA)	Solar Zenithal Angle (SZA)	Azimuthal Angular Difference
[DR5]	0° - 40°	0° - 40°	-
[DR6]	0° - 40°	0° - 40°	10° - 170°
[DR7]	0° - 60°	30°	0° - 180°
[DR8]	-	30°	0° - 180°
[DR9]	0° - 40°	0° - 40°	-
GSICS	0° - 40°	0° - 40°	
This study	0° - 30°	0° - 30°	-

Table 2-4 - Literature review of the angular range restriction

In order to avoid any backscattering features that might be present in the ice crystal phase function, it should be emphasized that in this study, the phase angle, which is defined as the angle between of the viewing zenith to the backscattering direction, will be selected in order to be larger than 5°, the value of 0° being defined as the exact backscattering direction.

2.1.4. Duration of the accumulation period

Finally, the duration of the accumulation period defined to build the histogram of DCC pixels is important. The influence of various duration of the accumulation period has been examined, in particular on possible seasonal effects. An accumulation period of one month is recommended for the processing of SEVIRI data. However, there is also a limit on the minimum number of DCC pixels accumulated in the histogram. When this number not reached after a month, the duration of the accumulation period is expended until the required minimum of DCC pixels is reached.

Article	Accumulation period	Temporal shift
[DR5]	1 month	-
[DR6]	1 month	
[DR7]	1 month	-
[DR8]	-	-
[DR9]	-	-
GSICS	1 month	1 day/5 days
This study	1 month or more if not enough pixels have been acquired	5 days

Table 2-5 - Literature review of the temporal criteria used

2.2. SUMMARY OF THE IDENTIFICATION CRITERIA

Table 2-6 summarises the set of identification conditions used in this study for the processing of SEVIRI data.

Identification Criteria	Values set for this study
Geographic Zone	Tropical ocean and land - ITCZ
Latitude/Longitude	30°N-30°S/according to SPP
Local Time	12h +/- 2h
Viewing Zenithal Angle (VZA)	0° - 30°
Solar Zenithal Angle (SZA)	0° - 30°
Azimuthal Angular Difference	-
Spatial extension	5*5
Relative Reflectance Deviation	2%
Temperature Standard Deviation	0.5K
Accumulation period	1 month – more of not enough pixels have been acquired
Temporal shift	5 days

Table 2-6 Identification criteria and their values in this study

3. DEFINITION AND VALIDATION OF A STANDARD DCC REFERENCE MODEL

3.1. OVERVIEW OF THE APPROACH

The objective of WP 2 is the development a physically-based DCC Reference Model (RM) based on literature review. The vertical structure of the DCC RM principally relies on the model proposed in [DR5], **assuming invariant properties** along the year. In this paper, optical properties of DCCs are investigated through the use of CloudSat Cloud Profile Radar (CPR) and Cloud Aerosol Lidar Infrared Pathfinder Satellite Observation (CALIPSO) measurements.

Cloud top temperature alone cannot fully define a DCC - since no differentiation can be made from cirrus or anvils clouds. Sohn and al. proposed then to use CloudSat reflectivity for setting the details of the vertical profile, which is a single-layer cloud whose depth is higher than 15 km. The lower part of the cloud, is composed of water droplets with a constant effective radius, up to 7km, while above 7km the upper one is composed of ice particles with a vertical effective radius and optical thickness distribution shown on Figure 4. The water part is not fully characterized since the CloudSat-derived liquid water content and liquid effective radius were erroneous at the time of the study of Sohn et al., due to the miscalculation of the attenuation by the liquid clouds droplets. On the other hand, the ice water content and ice particle effective radius are reliable data and used here to explain the discrepancy between sea and land DCCs.

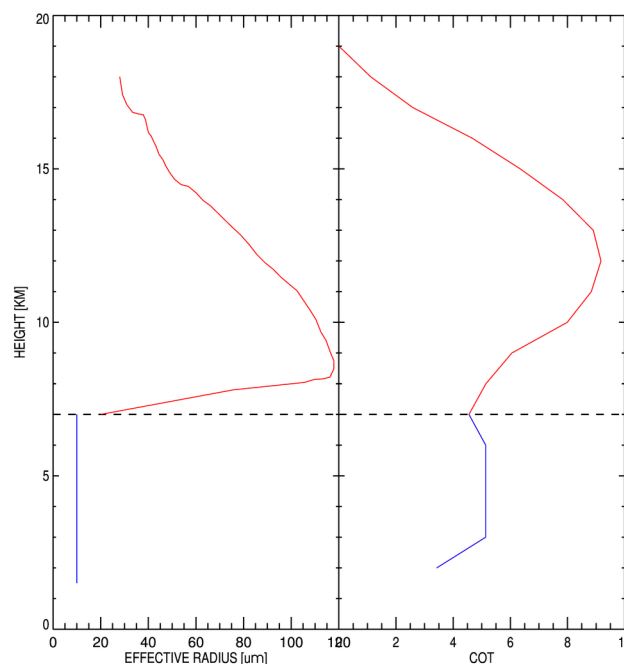


Figure 4 - DCC effective radius and optical thickness vertical profile after [DR5]. Ice crystals are shown in red and water droplet in blue.

The two most sensitive parameters of the proposed RM are thus the COT and the effective radius of the ice particle in the upper part of the cloud as can be seen from Figure 4. Ice particle single scattering properties, i.e., single scattering albedo and phase function will be taken from [DR1] as implemented in libRadtran. Based on the recommendations of Philip Watts during the Kick-off meeting, only the phase function of severely roughened aggregates is used, instead of using a general habit mixture of the former with, in addition, severely roughened solid columns and a general habit mixture of 9 habits (rosettes, columns, plates, droxtals...).

3.2. MOST RELEVANT PARAMETERS

3.2.1. Cloud Optical Thickness

The cloud optical thickness (COT) depends on the moisture density and vertical depth of the cloud. It is mostly due to the scattering of light by droplets or crystals, the nature of the cloud content (liquid or ice) and the size distribution of the water droplets or ice crystals.

The total DCC Cloud Optical Thickness (COT) typically varies between 70 and 200. As the COT increases, the contribution of the signal from the surface becomes negligible. In the algorithm used for this study, the COT vertical profile is taken from Figure 4 right panel which is rescaled according to the total optical thickness.

3.2.2. Ice crystal effective radius

The effective radius vertical profile is taken from the measurements of the CloudSat-derived products gathered in Sohn [DR5] (Figure 4, left panel). For the sensitivity analyses performed on the effective radius in Section 3.4.3, only the value in the upper layer is perturbed. It should be noted that any further use of the phrase “effective radius” in the rest of this study makes reference to this upper layer effective radius.

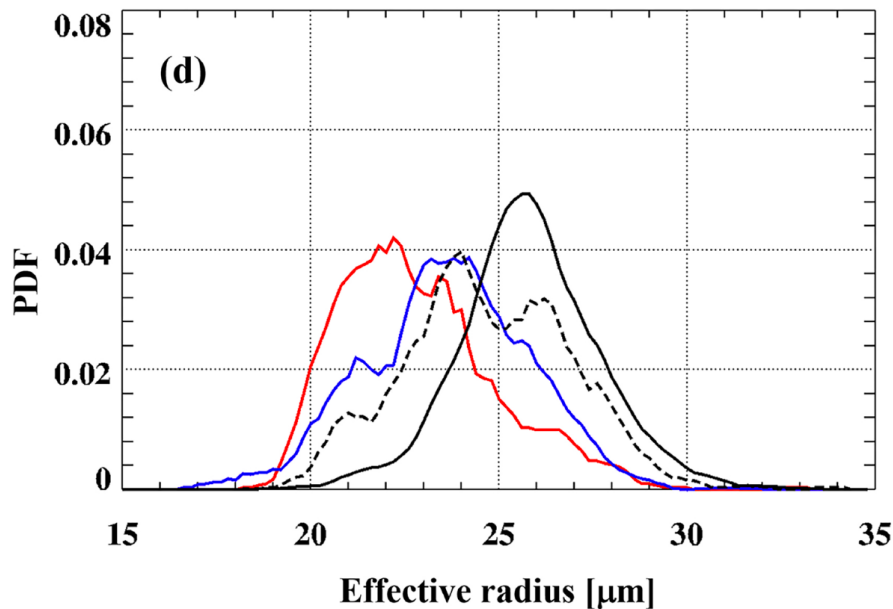


Figure 5 - Effective radius of the same MODIS products from Africa (in red), South America (in blue), Western Pacific over land (in dotted black) and Western Pacific over ocean (in solid black) - Source: [DR5]

3.3. PROPOSED MICROPHYSICAL AND OPTICAL PARAMETER VALUES

Article	Temperature Threshold	COT Range	COT Mode	Particle Radius Range	Particle Radius Mode
[DR6]	205K	<50		-	
[DR7]	190K	100 - 400	200	15μm - 25μm	20μm
[DR8]	205K	40 - 100		15μm - 40μm	15μm
[DR9]	205K - 195K			-	
GSICS	205.4K				

This study	205K		100		23µm (land) 25µm (sea)
------------	------	--	-----	--	---------------------------

Table 3-1 Literature review of the microphysical parameters used in various DCC reference models

Sensitivity analyses with respect to the DCC RM parameters have been performed in Meteosat Second and Third generation solar channels, in Section 5. The DCC RM is used for the generation of TOA spectral radiance in the 350nm – 2500nm spectral interval. The RTMOM RTM has been used to generate DCC TOA BRF with these parameters.

3.4. DCC RM SENSITIVITY ANALYSIS

3.4.1. Experimental Setup

In this section, a sensitivity analysis to the RM model parameter values is conducted on the Top Of Atmosphere Bidirectional Factor (TOA BRF) in the principal plane. The sun zenith angle is set to 25°, close to the range limit of this study, in order to maximise any effects. The maximal viewing angle considered for this sensitivity study is within the range defined in the Table 2-6, at 30°.

The TOA BRF, computed by the RTMOM RTM and based on the spectral responses of the calibrated instrument, are stored in LUTs whose different entries consist in the wavelengths, the angles and the various parameters whose variations are of interest in this study:

- the COT (Section 3.4.2);
- the effective radius (Section 3.4.3);
- the surface reflectance (Section 3.4.4);
- the total ozone amount in the atmospheric column (Section 3.4.5);
- the Rayleigh diffusion over the cloud top height (Section 3.4.6.1);
- the total content of water vapour in the atmospheric column (Section 3.4.6.3).

3.4.2. Sensitivity to COT

- Over land

The relative and absolute differences for the TOA BRF in the principal plane can be seen in Table 3-2, on land, with an effective radius of 23µm for a range of COT values of 100, with an uncertainty of ±20. The change of COT is performed rescaling the vertical profile shown in Figure 4. Beyond this range, the differences between the calibration coefficients derived over DCC and bright desert become significant.

COT range	Band	Minimal relative abs. diff. in TOA BRF (PP)	Maximal relative abs. diff. in TOA BRF (PP)	Minimal absolute diff. in TOA BRF (PP)	Maximal absolute diff. in TOA BRF (PP)
80-120	VIS 0.6	3.0%	3.2%	0.028	0.030
	VIS 0.8	2.8%	2.9%	0.027	0.029
	NIR 1.6	3.6%	3.9%	0.010	0.011
	HRVIS	2.9%	3.1%	0.027	0.030

Table 3-2 - Comparison of TOA BRF in the principal plane for different values of the COT, from 80 to 120.

The higher the COT values are considered, the lower the relative or absolute difference in the BRF is obtained in the principal plane. The choice of the COT has a limited impact on the TOA BRF value in the band VIS 0.6 (as can be seen on Figure 6), in the band VIS 0.8 (on Figure 7) or in the band HRVIS (on Figure 9) at high COT value: a 10% increase of the COT translates into an increase of about 1% of the TOA BRF. It should be noted that high sensitivity to COT in the NIR1.6 band (on Figure 8) results from the rescaling mechanism, affecting thereby the contribution of the lower layers which host ice particles different radii.

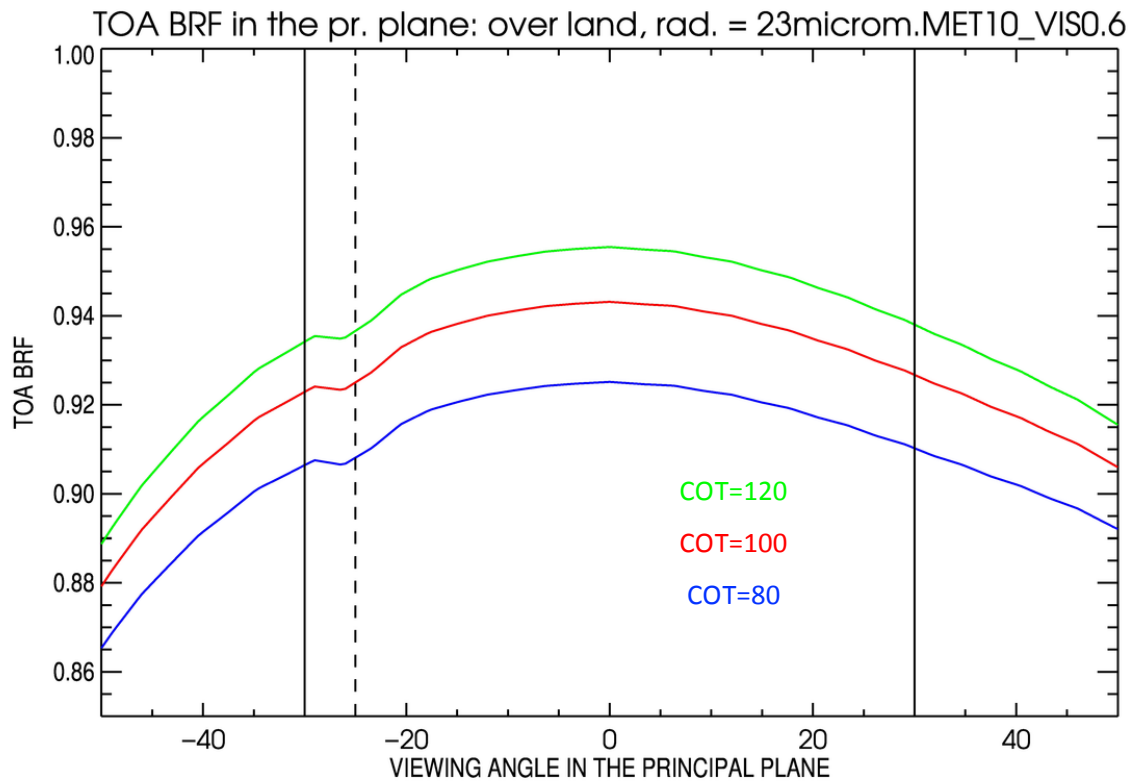


Figure 6 - Top Of Atmosphere Bi-Directional Factor in the Principal Plane for Meteosat 10 band, VIS0.6, with different COT on land, at a fixed effective radius of 23µm. The vertical dotted line is the zenithal sun angle at 25°, while the solid lines mark maximal viewing zenithal angle allowed.

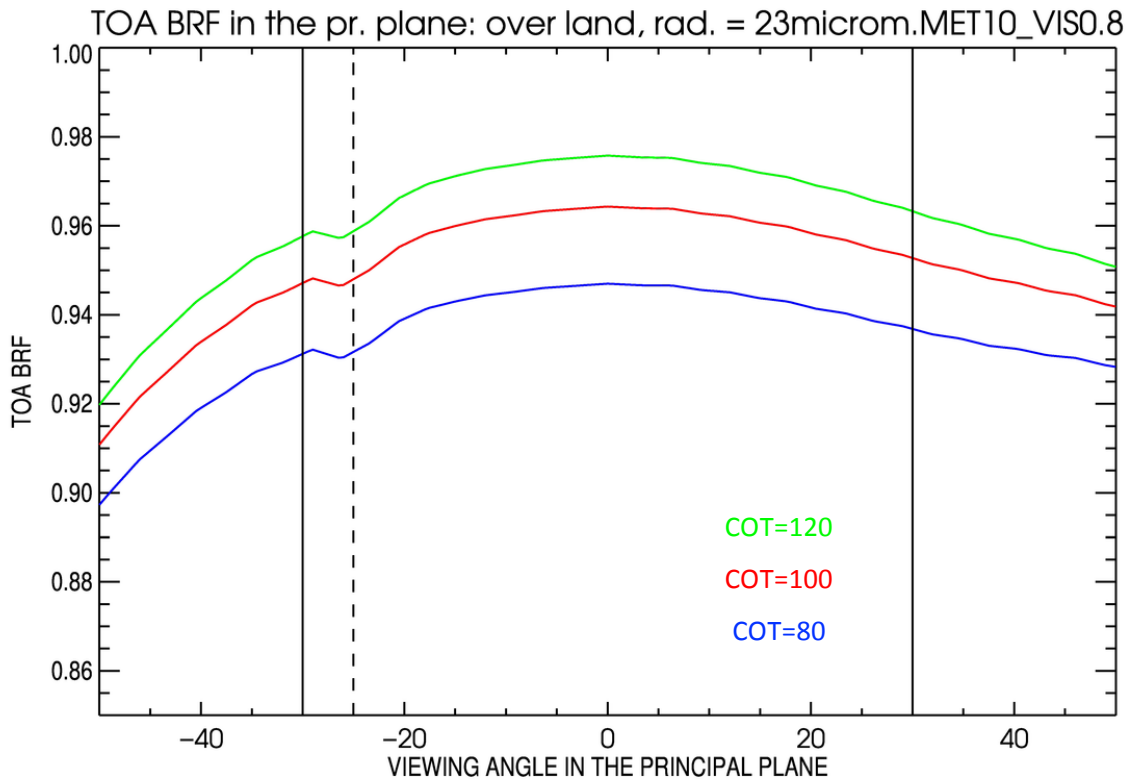


Figure 7 - Same as Figure 6, in the band VIS0.8.

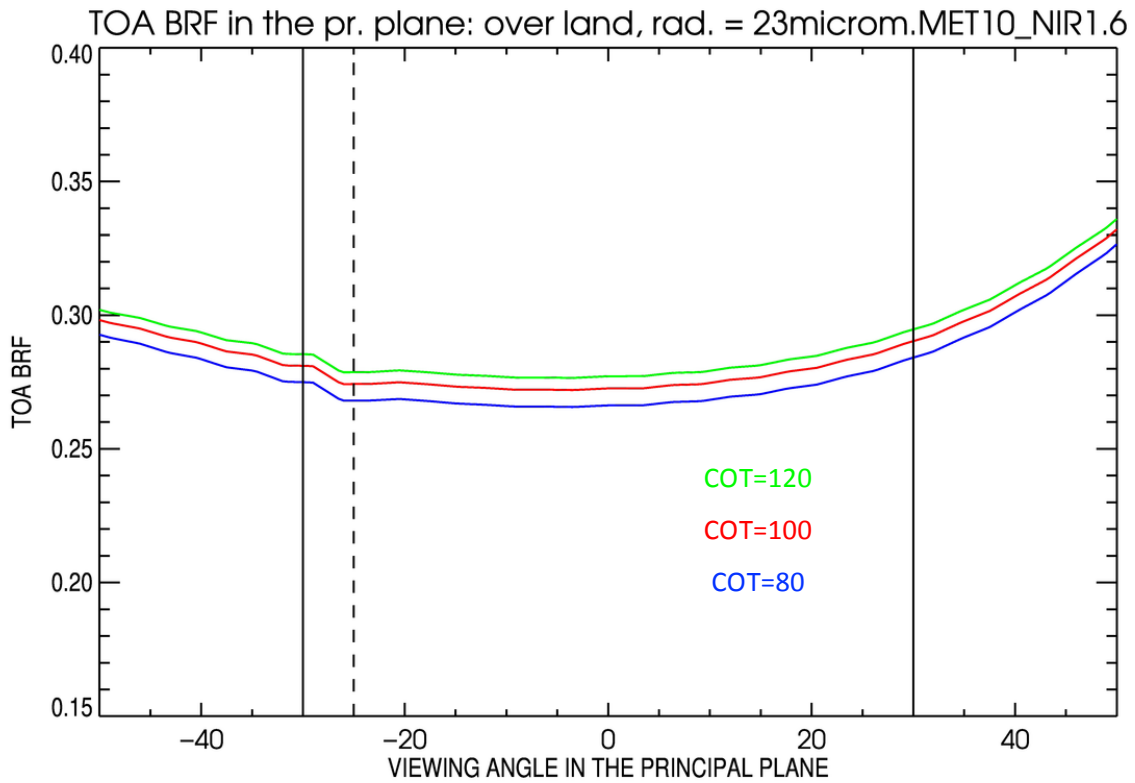


Figure 8 - Same as Figure 6, in the band NIR1.6.

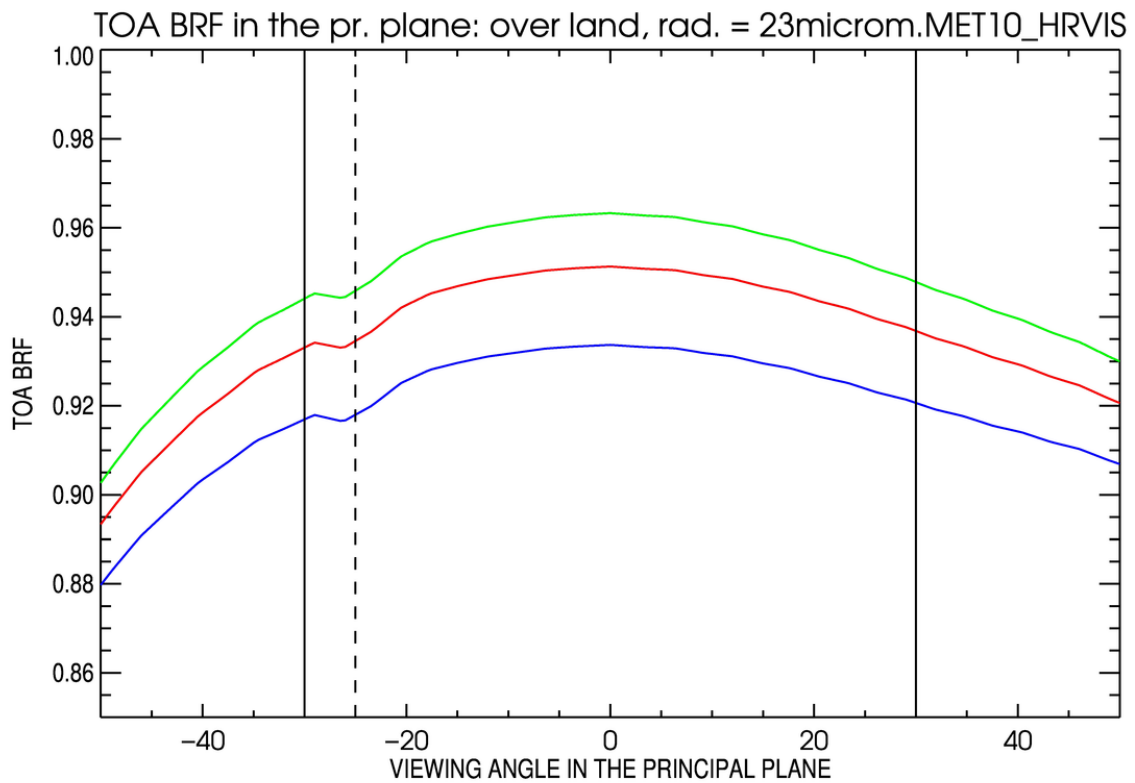


Figure 9 - Same as Figure 6, in the band HRVIS.

- Over sea

The relative and absolute difference for the TOA BRF in the principal plane can be seen in the Table 3-3, on sea, with effective radii of 25µm, for a range of COT values framing the nominal values of 100, within an uncertainty of ±20.

COT range	Band	Minimal relative abs. diff. in TOA BRF (PP)	Maximal relative abs. diff. in TOA BRF (PP)	Minimal absolute diff. in TOA BRF (PP)	Maximal absolute diff. in TOA BRF (PP)
80-120	VIS 0.6	2.9%	3.1%	0.028	0.030
	VIS 0.8	2.6%	2.8%	0.025	0.027
	NIR 1.6	3.3%	3.7%	0.009	0.010
	HRVIS	2.8%	3.0%	0.027	0.029

Table 3-3 - Comparison of TOA BRF in the principal plane for different values of the COT 80 to 120.

The same conclusion as for the study over land can be drawn: the band VIS 0.6 (depicted in Figure 10), the band VIS 0.8 (in the Figure 11) and band HRVIS (in the Figure 12) show the same range of variations with the COT values. The band NIR 1.6 is the least impacted in terms of absolute reflectance value (in the Figure 13) due to a lower reflectance value in that band.

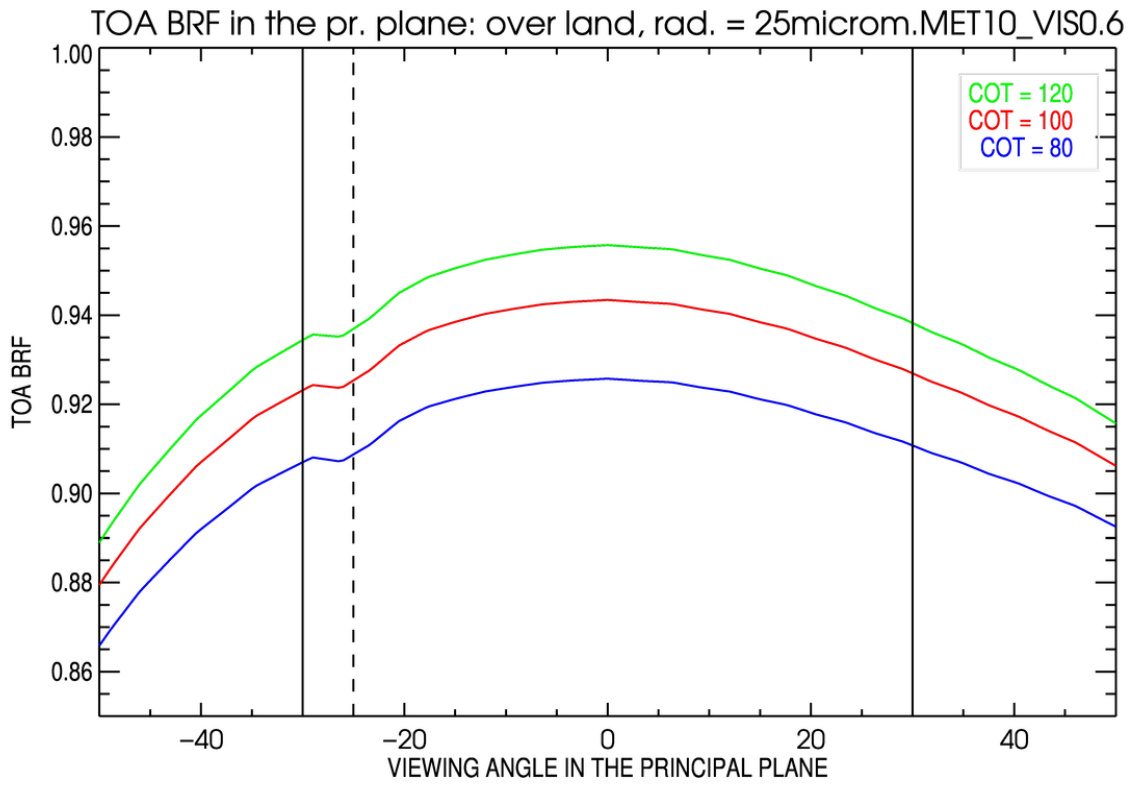


Figure 10 - Top Of Atmosphere Bi-Directional Factor in the Principal Plane for Meteosat 10 band, VIS0.6, with different COT on sea, at a fixed effective radius of 25µm. The vertical dotted line is the zenithal sun angle at 25°, while the solid lines mark maximal viewing zenithal angle allowed.

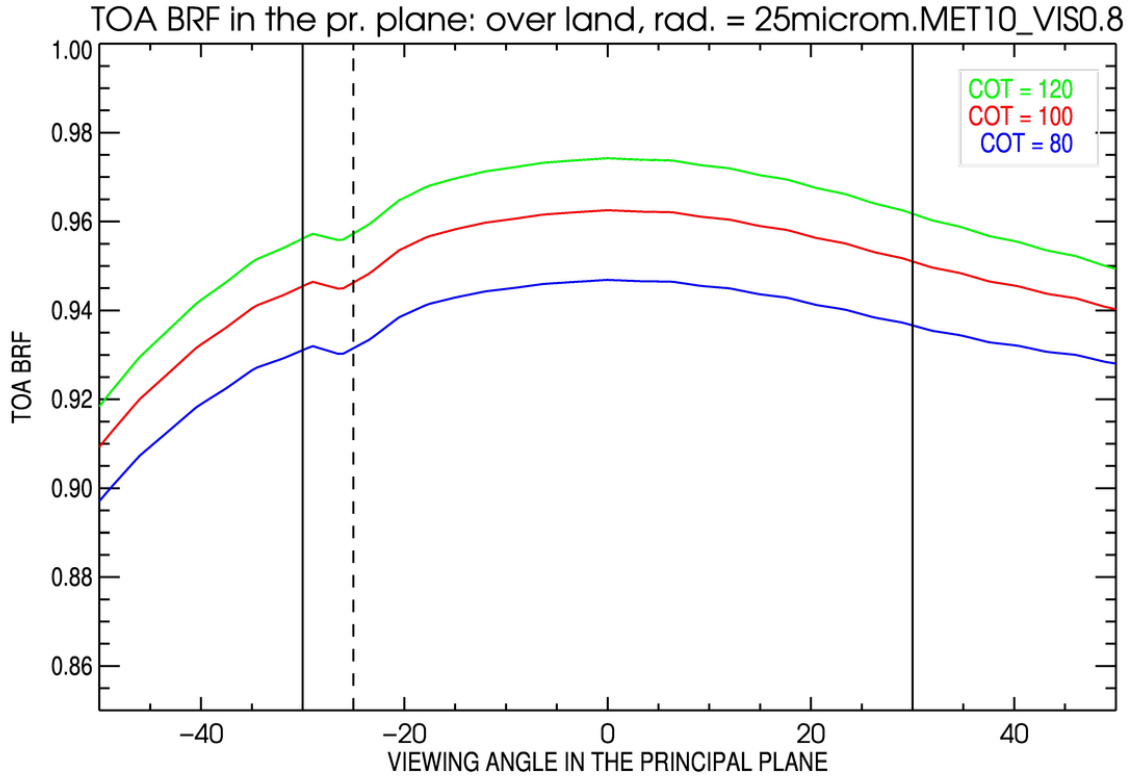


Figure 11 - Same as Figure 10, in the band VIS0.8.

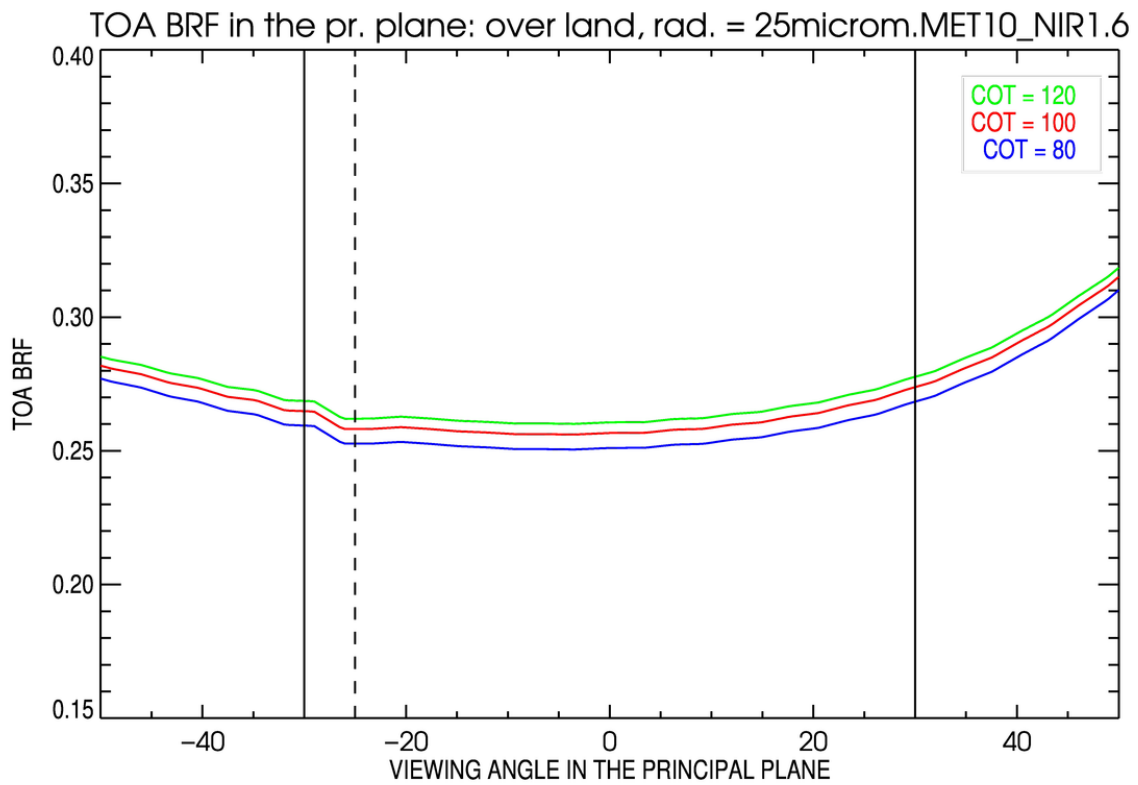


Figure 12 - Same as Figure 10, in the band NIR1.6.

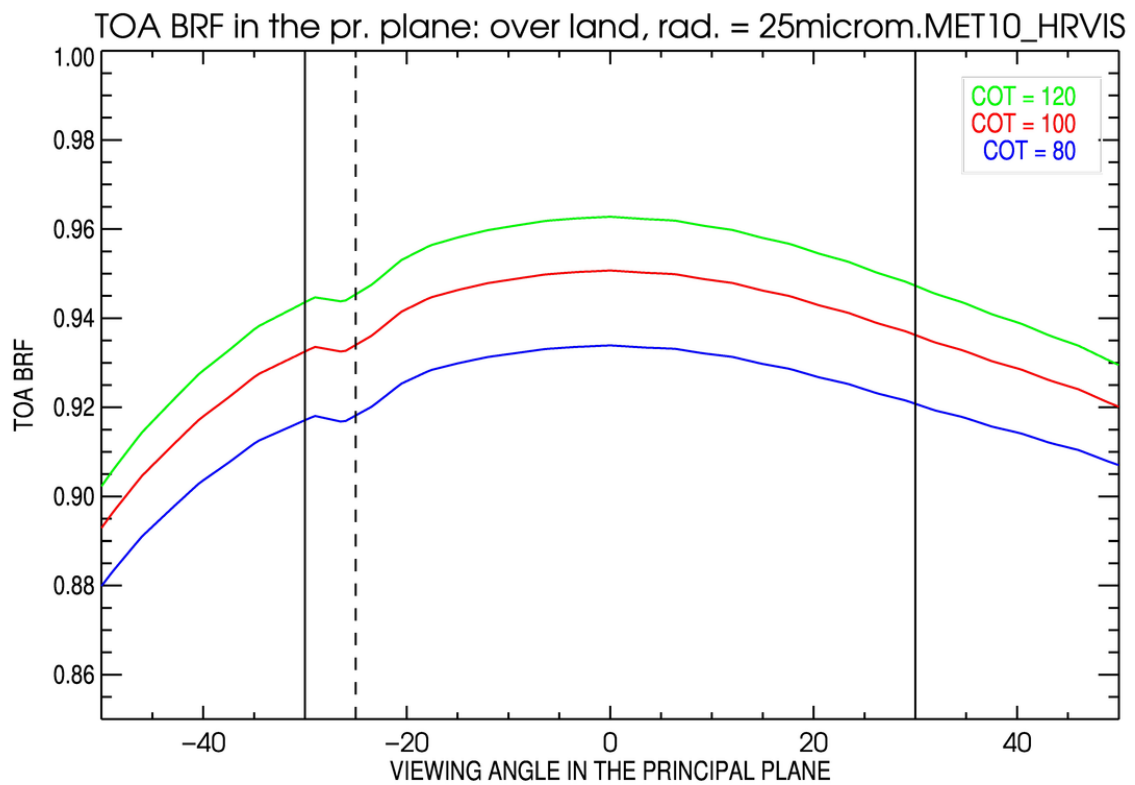


Figure 13 - Same as Figure 10, in the band HRVIS.

3.4.3. Sensitivity to effective radius

- Over land

The relative and absolute difference for the TOA BRF in the principal plane can be seen in Table 3-4, on land, with a fixed COT value of 100, for a range of effective radius centred around 23µm.

Effective radius range	Band	Minimal relative abs. diff. in TOA BRF (PP)	Maximal relative abs. diff. in TOA BRF (PP)	Minimal absolute diff. in TOA BRF (PP)	Maximal absolute diff. in TOA BRF (PP)
18-28	VIS 0.6	0.42%	0.49%	0.004	0.005
	VIS 0.8	0.00%	0.06%	0.000	0.001
	NIR 1.6	31.47%	32.94%	0.079	0.081
	HRVIS	0.18%	0.24%	0.002	0.002

Table 3-4 - Comparison of TOA BRF in the principal plane for different values of the effective radius at 18, 23 and 28µm.

The choice of an effective radius value mostly influences the TOA BRF in the NIR1.6 band (in Figure 14), for the land surface, while BRF in the other bands (Figure 15, Figure 16, and Figure 17) remain unaffected. An ice particles radius decreases of 5µm (21%) in the upper layer is responsible for an increase of the TOA BRF by about 0.048 (17%). The VIS0.8 band is not sensitive to a change of the upper layer radius by ±20%.

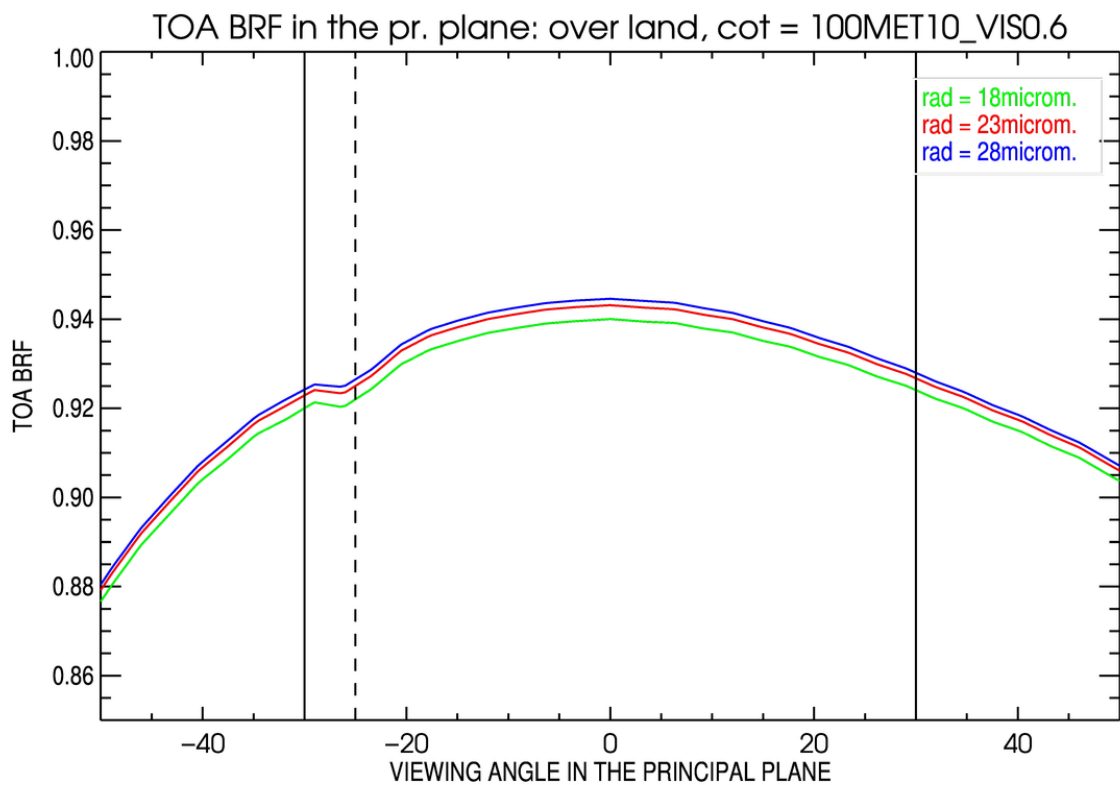


Figure 14 - Top Of Atmosphere Bi-Directional Factor in the Principal Plane for Meteosat 10 band, VIS0.6, with different effective radii on land, at a fixed COT of 100. The vertical dotted line is the zenithal sun angle at 25°, while the solid lines mark maximal viewing zenithal angle allowed.

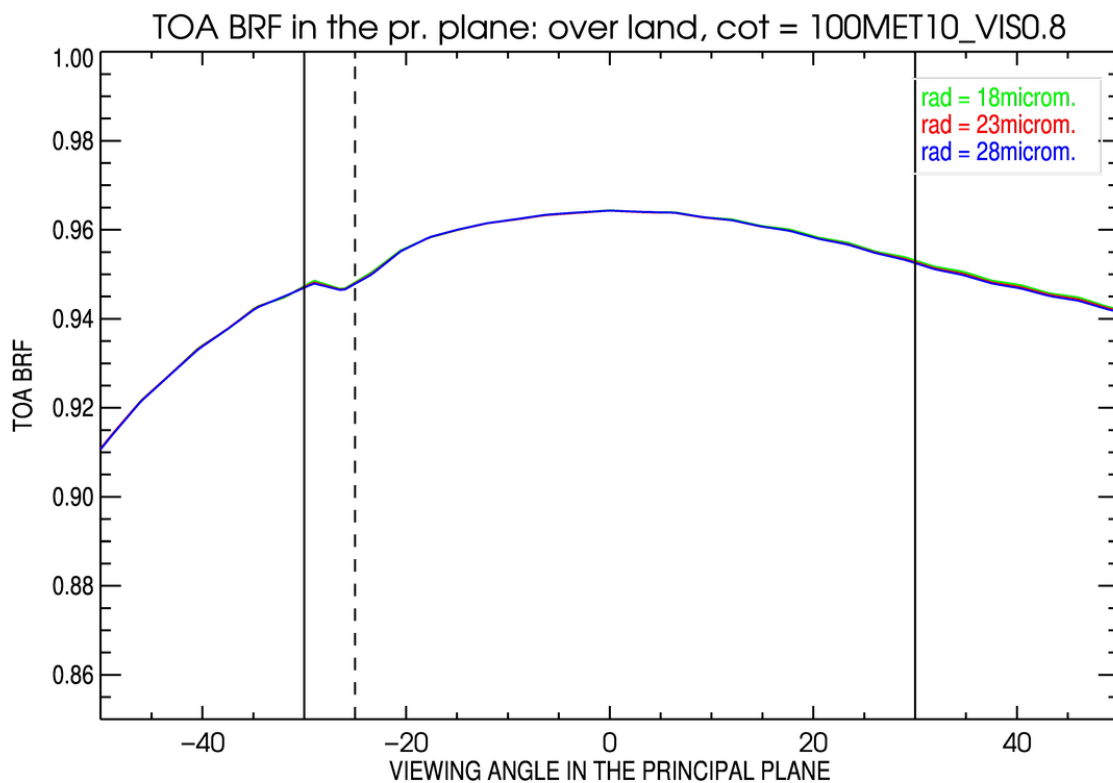


Figure 15 - Same as Figure 14, in the band VIS0.8.

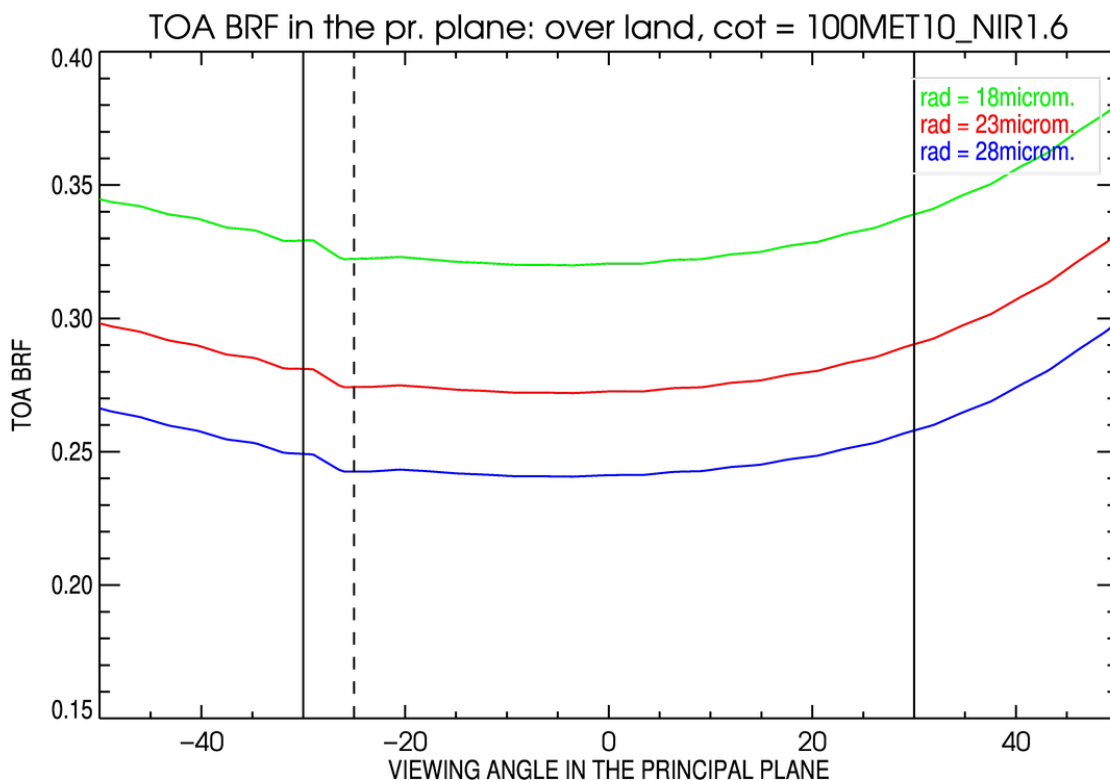


Figure 16 - Same as Figure 14, in the band NIR1.6.

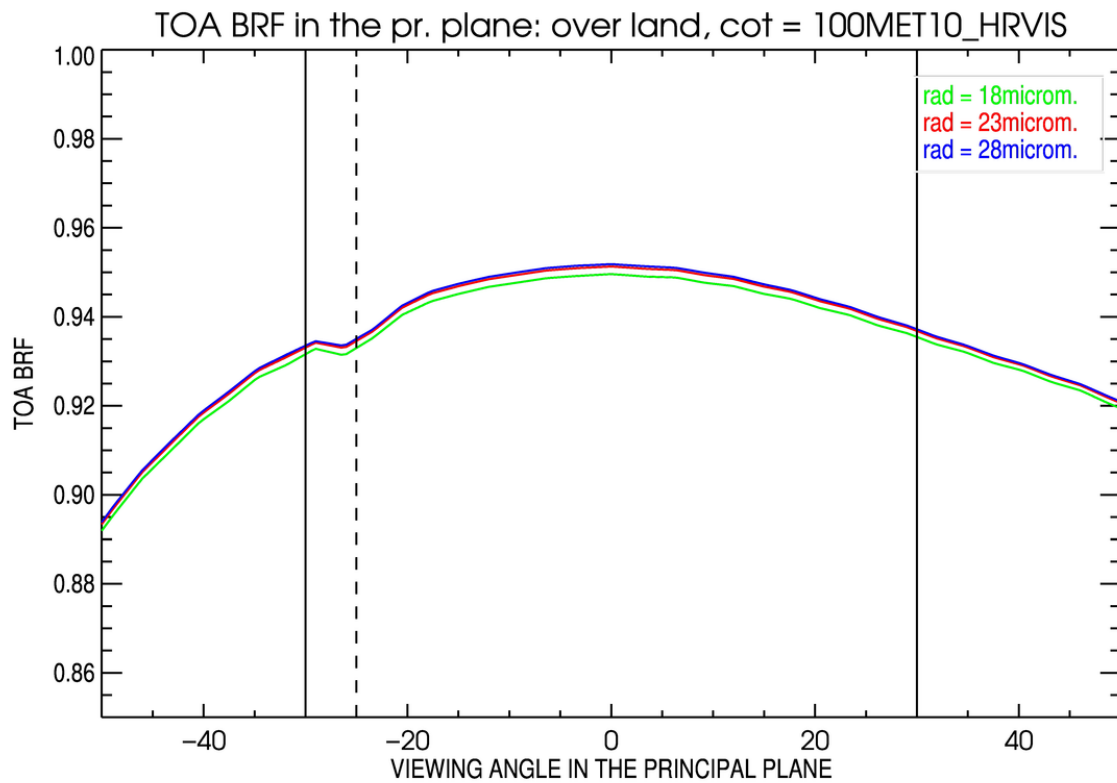


Figure 17 - Same as Figure 14, in the band HRVIS.

- Over sea

The relative and absolute difference for the TOA BRF in the principal plane can be seen in the Table 3-5, on sea, with a fixed COT value of 100, for a range of effective radius centred around 25µm.

Effective radius range	Band	Minimal relative abs. diff. in TOA BRF (PP)	Maximal relative abs. diff. in TOA BRF (PP)	Minimal absolute diff. in TOA BRF (PP)	Maximal absolute diff. in TOA BRF (PP)
20-30	VIS 0.6	0.32%	0.38%	0.003	0.003
	VIS 0.8	0.01%	0.07%	0.000	0.001
	NIR 1.6	29.63%	31.00%	0.071	0.072
	HRVIS	0.12%	0.16%	0.001	0.002

Table 3-5 – Comparison of TOA BRF in the principal plane for different values of the effective radius at 20, 25 and 30µm.

The TOA BRF of the band NIR 1.6 (in the Figure 20) is the most affected, while other visible bands remain weakly sensitive to the ice particle radius (in Figure 18, Figure 19 and Figure 21).

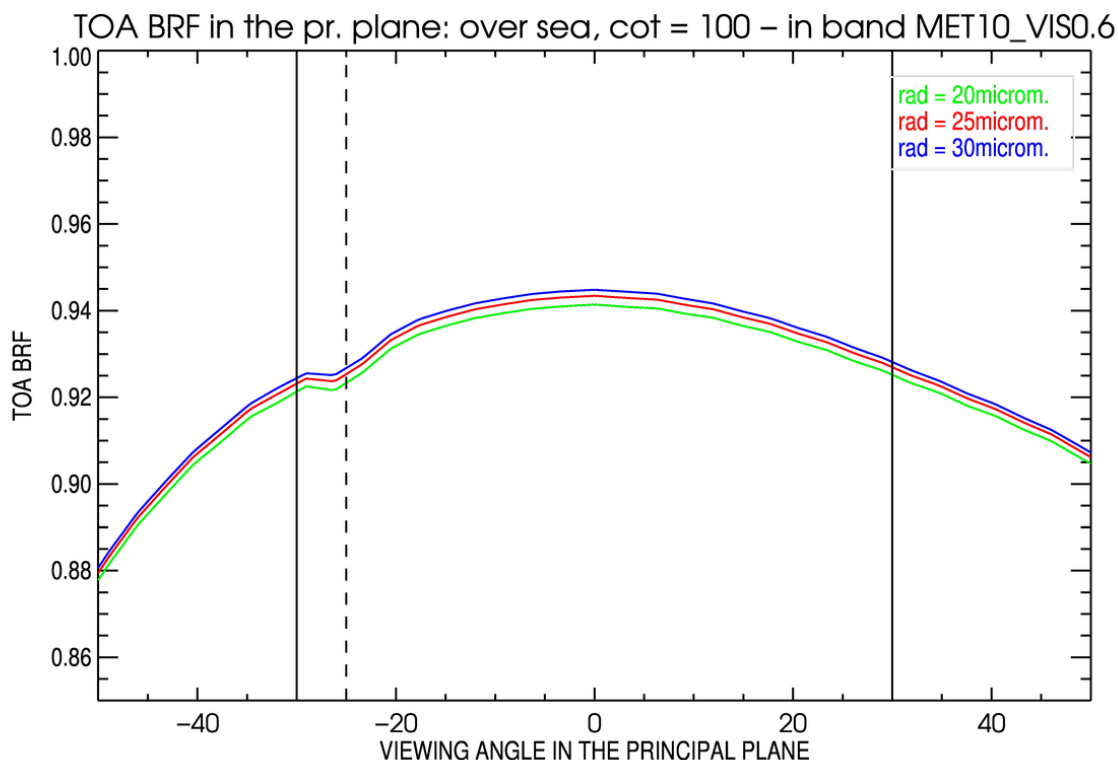


Figure 18 - Top Of Atmosphere Bi-Directional Factor in the Principal Plane for Meteosat 10 band, VISO.6, with different effective radii on sea, at a fixed COT of 100. The vertical dotted line is the zenithal sun angle at 25°, while the solid lines mark maximal viewing zenithal angle allowed.

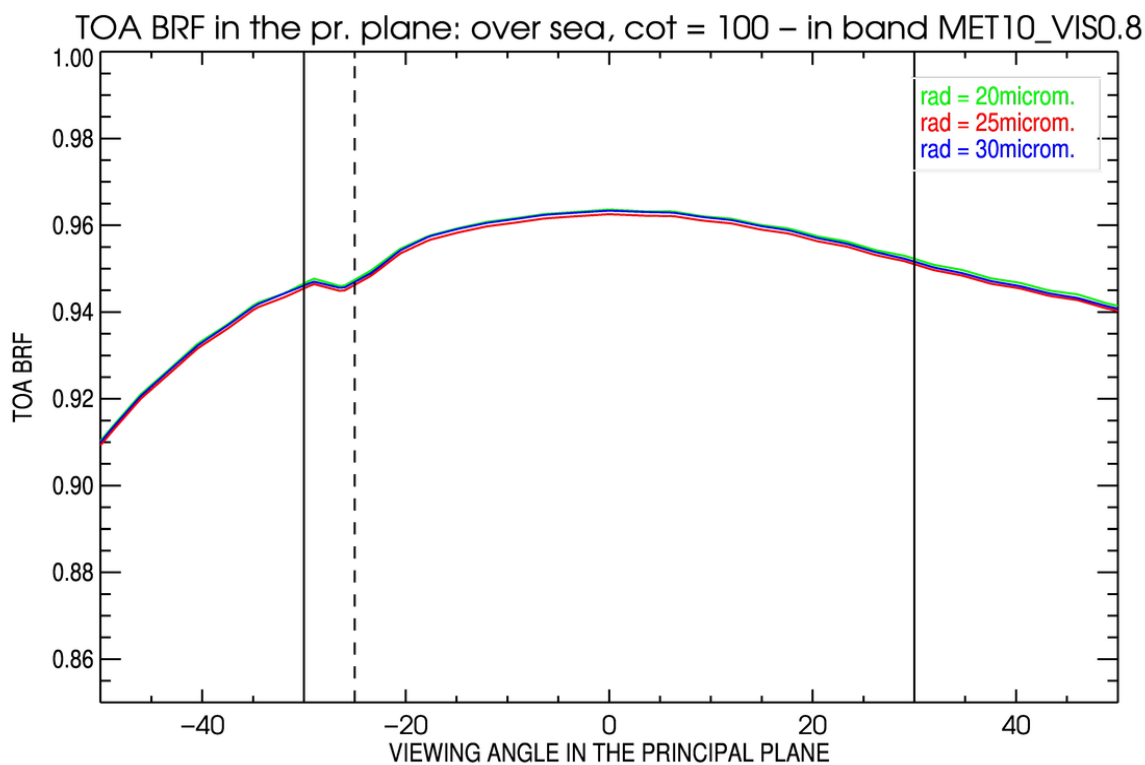


Figure 19 - Same as Figure 18, in the band VISO.8.

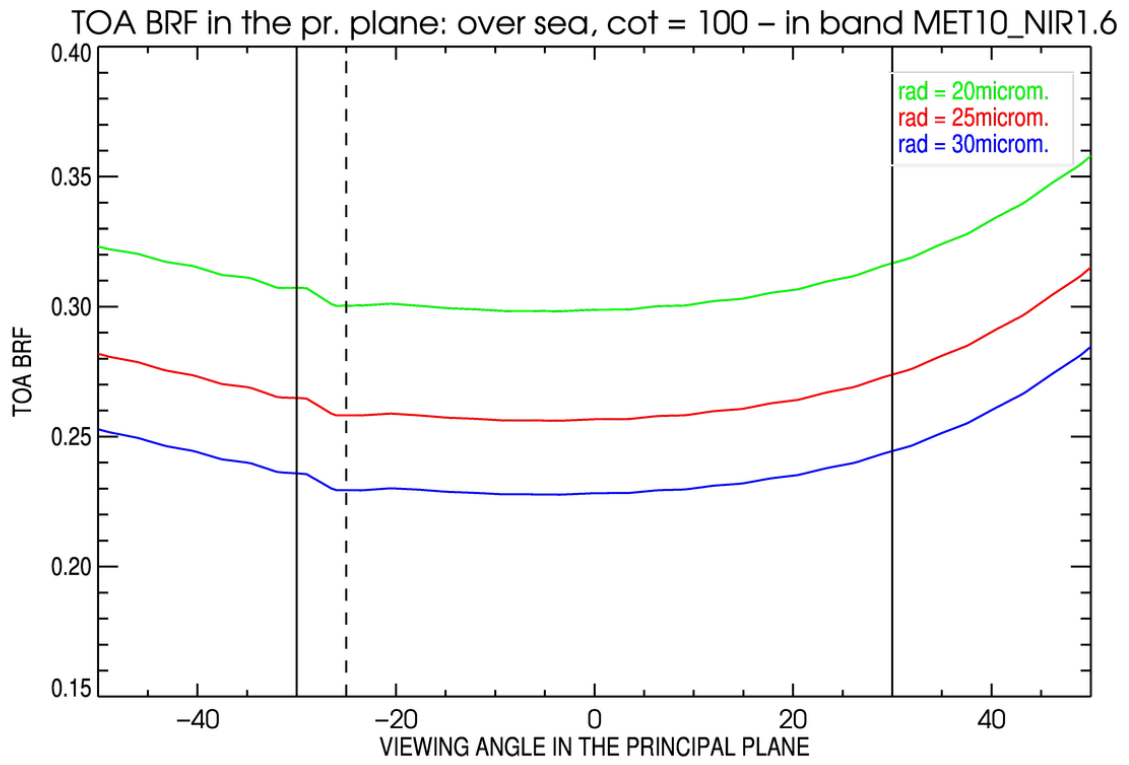


Figure 20 - Same as Figure 18, in the band NIR1.6.

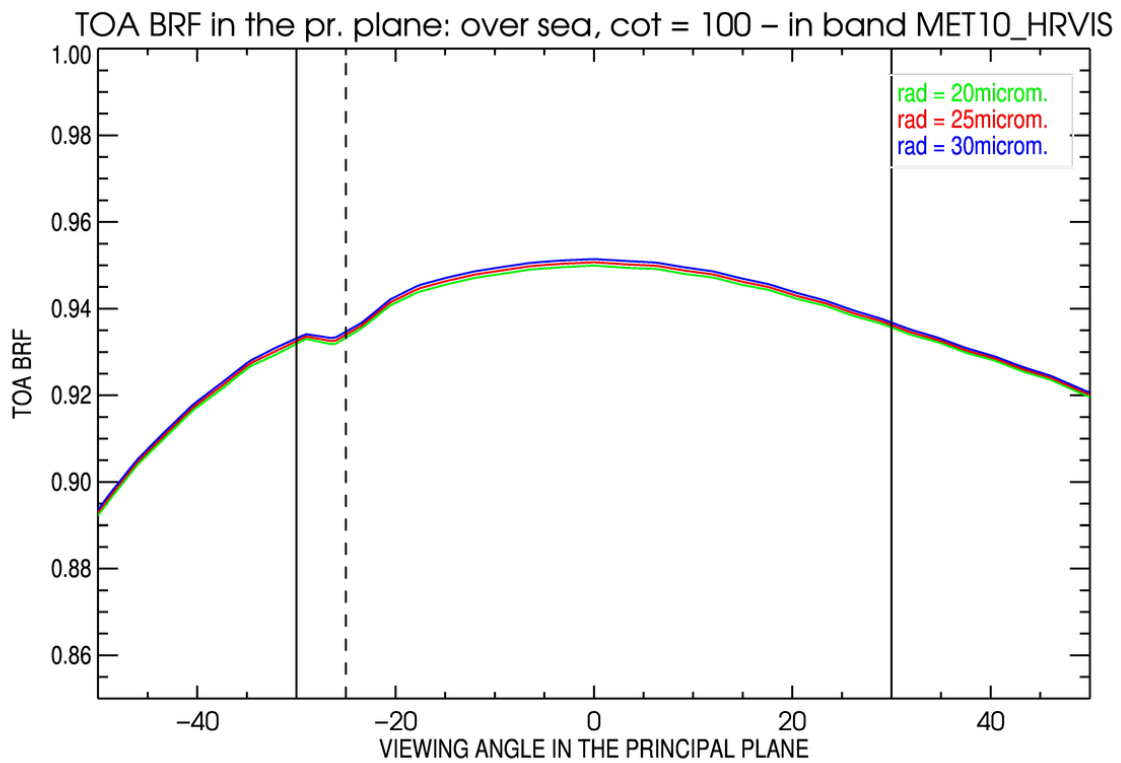


Figure 21 - Same as Figure 18, in the band HRVIS.

3.4.4. Sensitivity to surface reflectance

The relative and absolute differences for the TOA BRF in the principal plane over sea and land surfaces are displayed in Table 3-6. COT is set to value 100 and the effective radius to 25µm. Only surface reflectance varies between these two cases where a vegetated surface is assumed over land and open ocean reflectance over sea. In both cases, surfaces are assumed Lambertian. The results in every bands (as shown in Figure 22, Figure 23, Figure 24 and Figure 25) confirm the hypothesis that the signal coming from the surface can be neglected with such high value for the COT.

Surface	Band	Minimal relative abs. diff. in TOA BRF (PP)	Maximal relative abs. diff. in TOA BRF (PP)	Minimal absolute diff. in TOA BRF (PP)	Maximal absolute diff. in TOA BRF (PP)
Land vs Sea	VIS 0.6	0.02%	0.02%	0.000	0.000
	VIS 0.8	0.13%	0.14%	0.001	0.001
	NIR 1.6	0.00%	0.00%	0.000	0.000
	HRVIS	0.06%	0.07%	0.001	0.001

Table 3-6 - Comparison of TOA BRF in the principal plane for different surface types, with a COT at 100 and an effective radius of 25µm

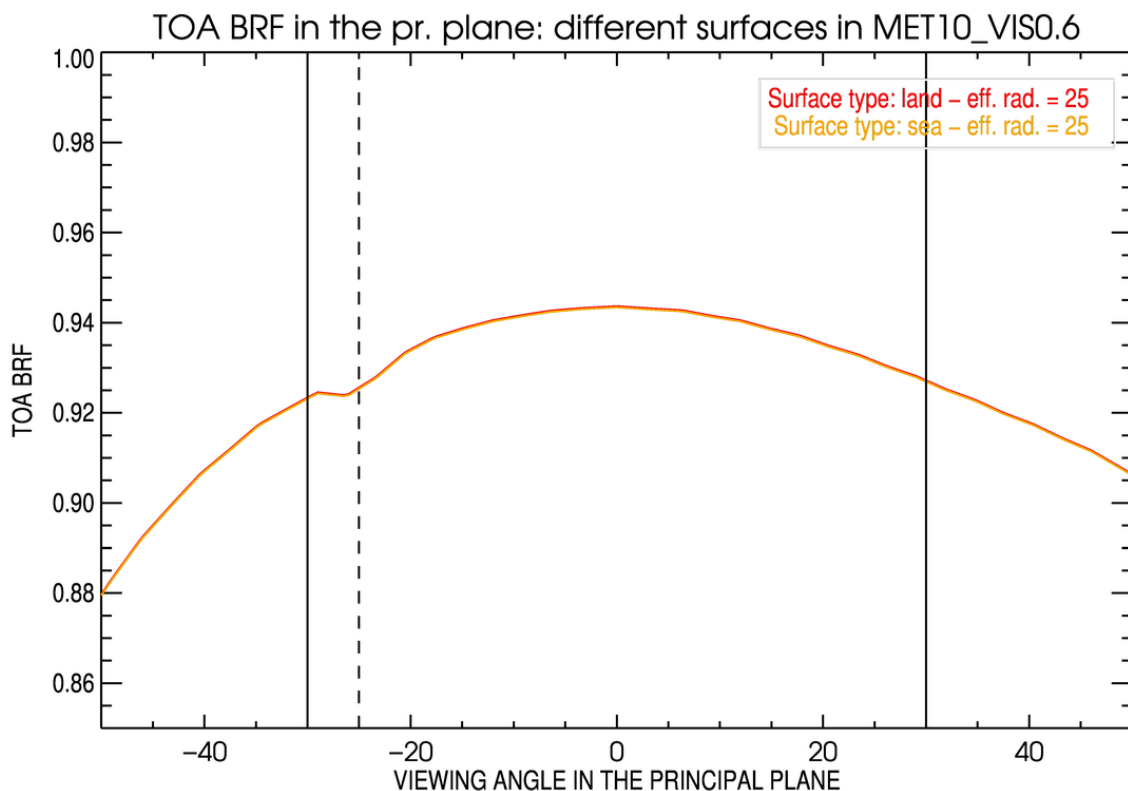


Figure 22 - Top Of Atmosphere Bi-Directional Factor in the Principal Plane for Meteosat 10 band, VIS 0.6, with two different kinds of surface: land (red) and sea (orange). The vertical dotted line is the zenithal sun angle at 25°, while the solid lines mark the maximal viewing zenithal angle allowed.

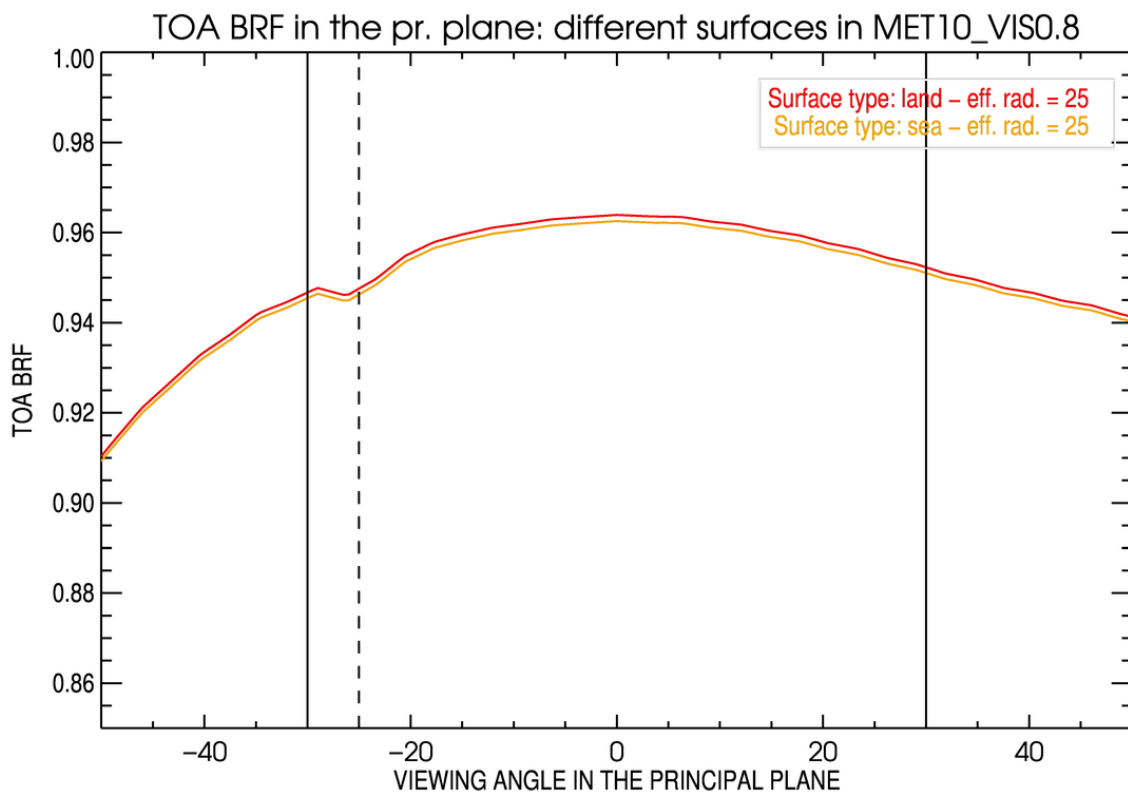


Figure 23 - Same as Figure 22, for the band VISO.8.

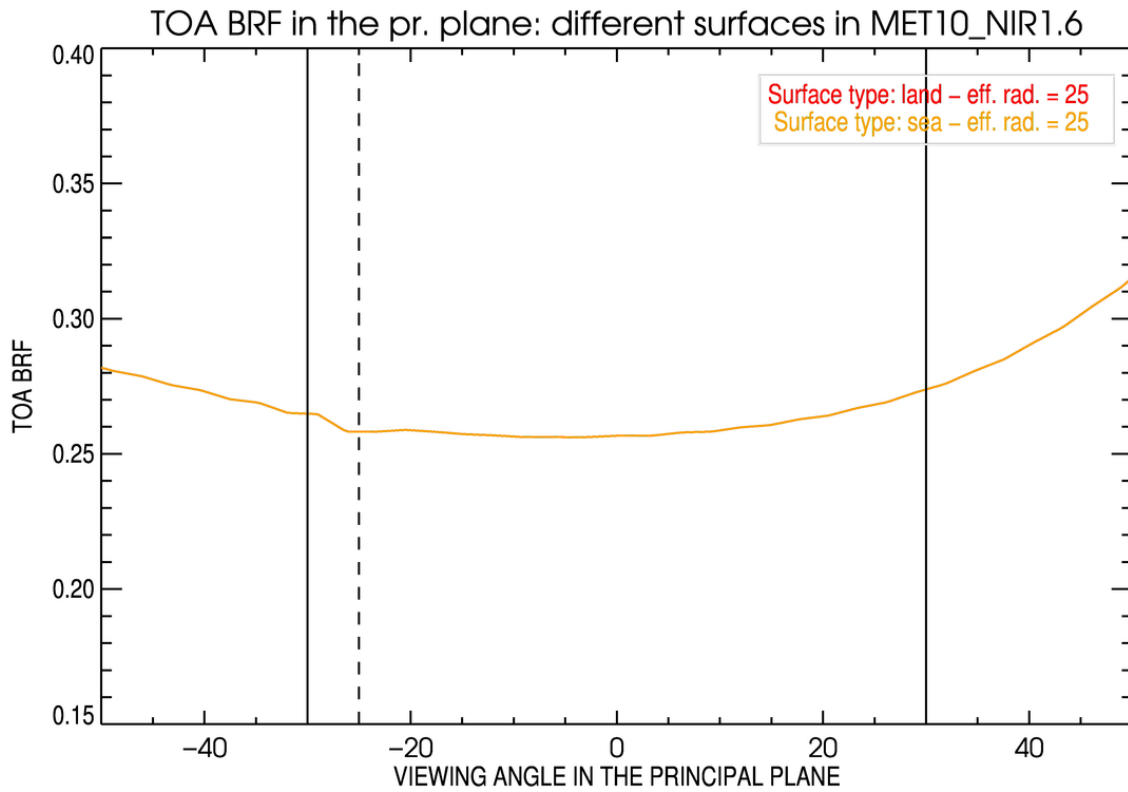


Figure 24 - Same as Figure 22, for the band NIR1.6.

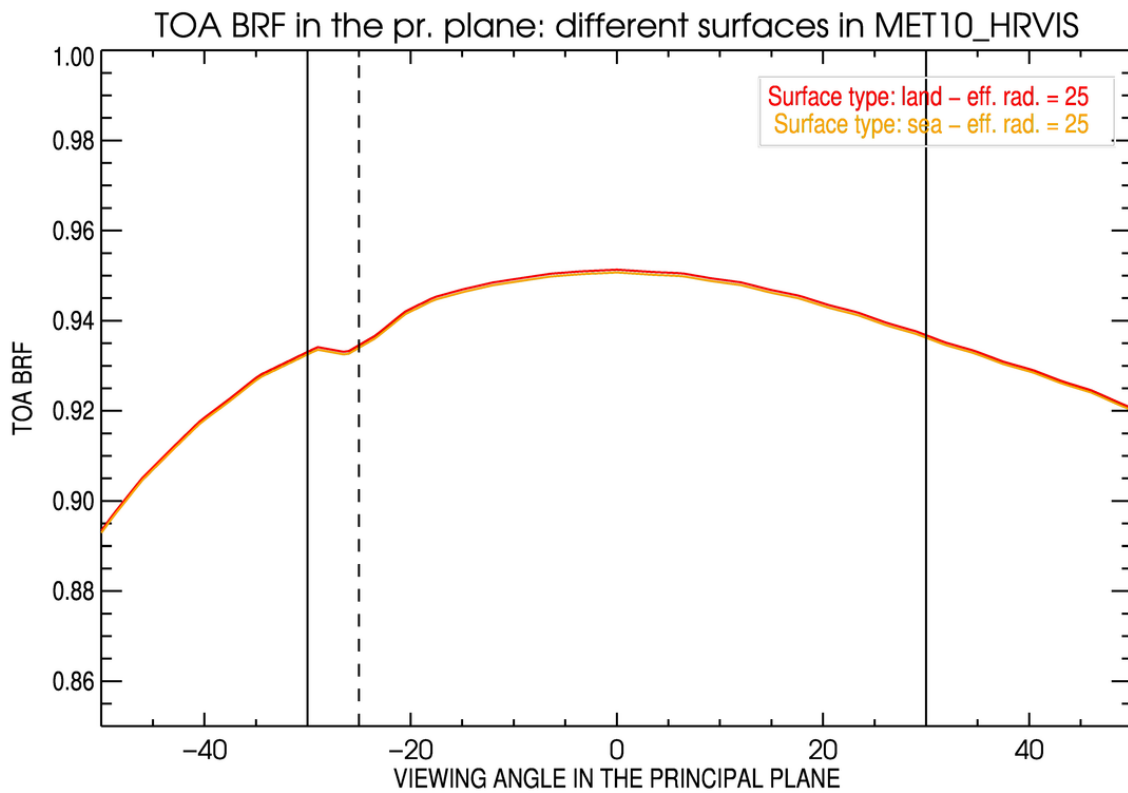


Figure 25 - Same as Figure 22, in the HRVIS band.

According to this sensitivity analysis, the effect of the surface reflectance, on land or on sea, does not exceed 0.14%. The surface type can therefore be neglected when simulating DCC TOA BRF LUTs.

3.4.5. Sensitivity to ozone

Sensitivity to total column ozone concentration has been tested in the VIS0.6 band using the standard configuration, i.e., an ice particle radius in the upper layer of 25µm for a COT of 100. Results are shown in Figure 26. Total ozone concentration was selected between 225DU and 300DU.

Ozone range (in Dobson Units)	Minimal relative abs. diff. in TOA BRF (PP)	Maximal relative abs. diff. in TOA BRF (PP)	Minimal absolute diff. in TOA BRF (PP)	Maximal absolute diff. in TOA BRF (PP)
225-250	0.43%	0.46%	0.004	0.004
250-283	0.57%	0.61%	0.005	0.006
283-300	0.29%	0.30%	0.003	0.003
225-300	1.29%	1.36%	0.012	0.013

Table 3-7 – Comparison of TOA BRF in the principal plane for different amounts of ozone in the atmosphere, with a COT at 100 and an effective radius of 23µm, over land.

As most of the ozone lies above the DCC, higher ozone concentration translates into larger absorption in the VIS0.6 band. A concentration increase of 25DU translates into a 0.4% decrease of the signal. Currently, sensitivity analyses in this report have been performed assuming a tropical standard atmosphere. Ozone concentration has not been considered as a DCC LUT dimension. However, accounting for the actual concentration might be necessary in order to reduce the uncertainty in the VIS0.6 band. It is however not considered as a high priority improvement, the impact of the actual COT value being much more important.

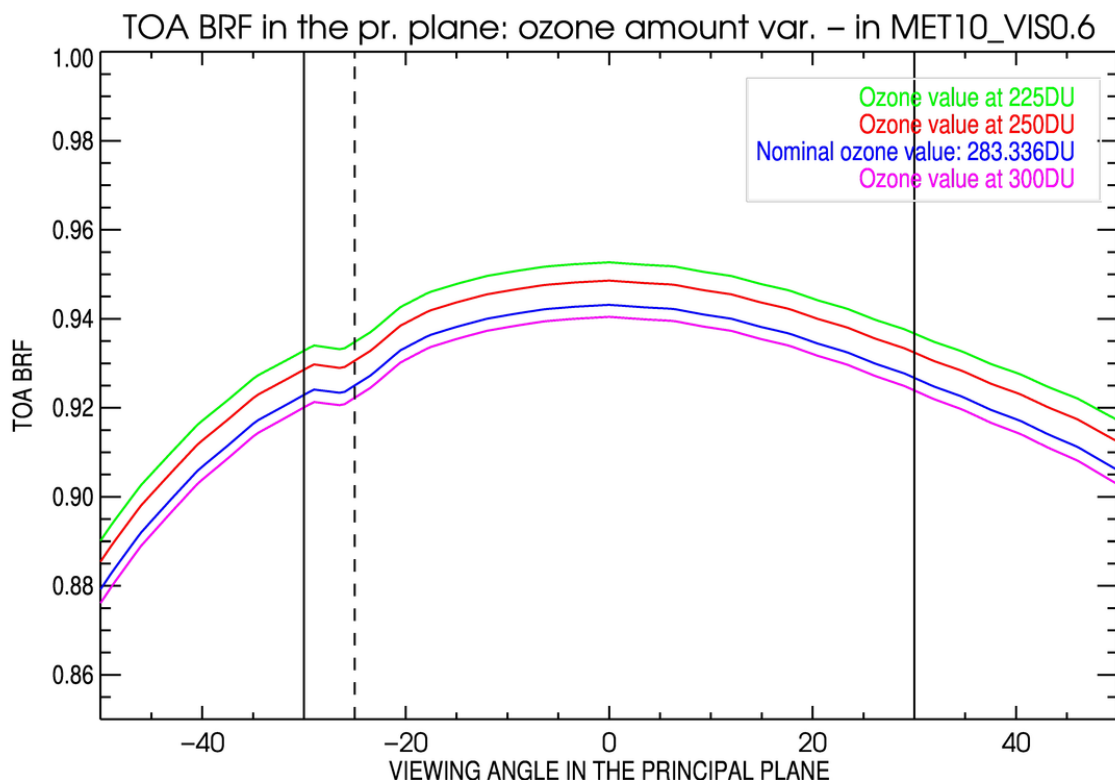


Figure 26 - Top Of Atmosphere Bi-Directional Factor in the Principal Plane for Meteosat 10 band, VIS0.6, with different values of the ozone total column concentration. The vertical dotted line is the zenithal sun angle at 25°, while the solid lines mark maximal viewing zenithal angle allowed.

3.4.6. FCI sensitivity analysis

3.4.6.1. Experimental setup

Specific sensitivity analyses have been performed to account for the additional spectral bands of MTG/FCI bands. Two additional parameters have been considered:

- The contribution of the Rayleigh scattering above the DCC top height;
- The contribution of the water vapour absorption above the DCC top height in the NIR1.3 band.

3.4.6.2. Sensitivity to Cloud Top Height

Changing the cloud top height influences the molecular concentration above the DCC inducing two effects: the influence of Rayleigh diffusion above the DCCs in the reference model is studied varying the height of the upper layer. According to the literature, e.g. [DR5], DCCs top heights can vary between 14km and 17km. The DCC cloud of the Reference Model is simulated with a height of 17km. In order to simulate a cloud with a top height at 14km, the entire cloud as been shifted by 3km. No rescaling of the vertical structure is performed.

Since the Rayleigh diffusion is inversely proportional to the wavelength, only MTG/FCI bands VIS0.4, VIS0.5 and VIS0.6 (Figure 28) and VIS0.6 (Figure 29) have been analysed. Results are shown in Table 3-8. It also increases molecular absorptions in case absorbing lines are present in the FCI spectral bands.

It is however difficult to discriminate these two effects. The effect is expected to be preponderant in the band VIS 0.4 (in the Figure 27), by comparison with the other bands, which is not the case. However, this simple reasoning does not take into account the impact of the absorption by molecules - such as the ozone, whose absorption alters significantly the TOA BRF in the VIS 0.6 band in particular.

Cloud Top Height range (in km)	Band	Minimal relative abs. diff. in TOA BRF (PP)	Maximal relative abs. diff. in TOA BRF (PP)	Minimal absolute diff. in TOA BRF (PP)	Maximal absolute diff. in TOA BRF (PP)
17-14	VIS 0.4	0.80%	0.96%	0.008	0.009
	VIS0.5	0.89%	1.00%	0.008	0.010
	VIS0.6	1.18%	1.30%	0.011	0.012
	VIS0.9	3.89%	4.24%	0.036	0.039
	NIR1.3	23.99%	24.80%	0.141	0.144
	NIR1.6	0.36%	0.38%	0.001	0.001
	NIR2.2	0.76%	0.79%	0.003	0.003

Table 3-8 – Comparison of TOA BRF in the principal plane for two cloud top heights, with a COT at 100 and an effective radius of 23µm, over land

DCC top height is therefore a critical parameter in spectral bands that includes molecular absorption above the cloud.

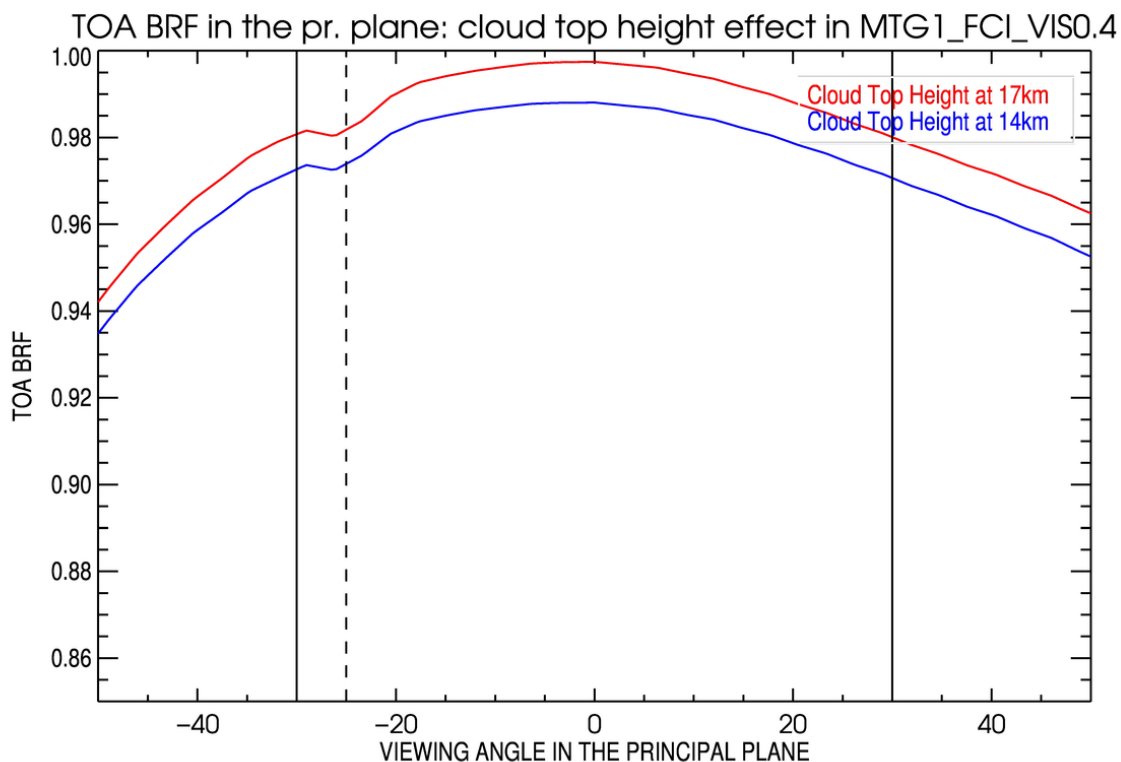


Figure 27 - Top Of Atmosphere Bi-Directional Factor in the Principal Plane for MTG1 band, VIS0.4, with different values for the cloud top height. The vertical dotted line is the zenithal sun angle at 25°, while the solid lines mark maximal viewing zenithal angle allowed.

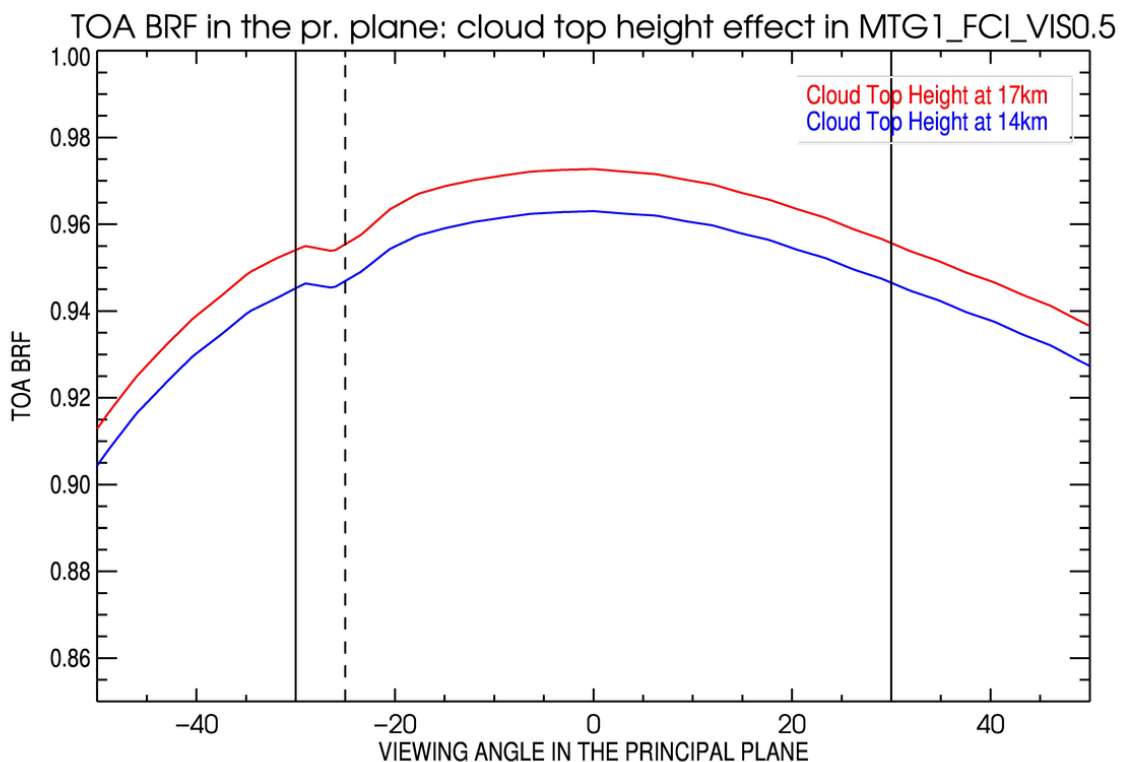


Figure 28 - Same as Figure 27, for MTG1 band, VIS0.5.

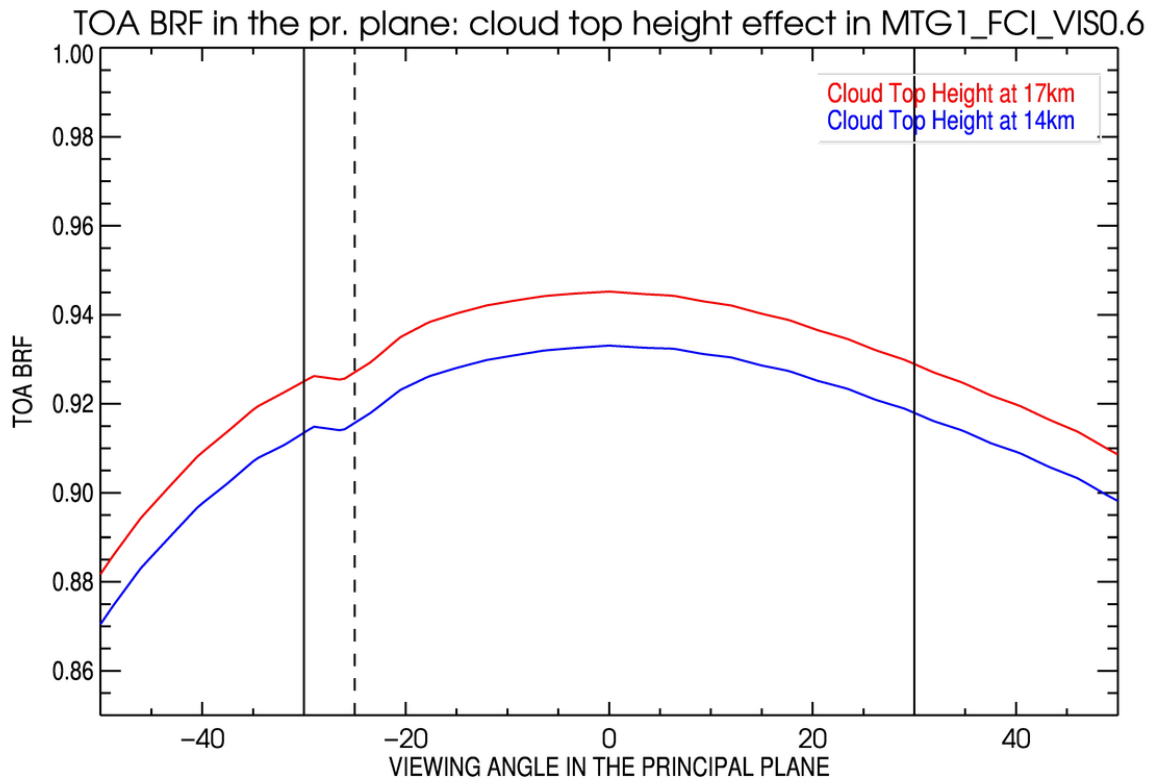


Figure 29 – Same as Figure 27, for MTG1 band, VIS0.6.

3.4.6.3. Water vapour content

Water vapour mostly absorbs light in the NIR1.3 band (depicted on Figure 30). The total amount of water vapour in the atmospheric column typically varies between 20 to 60 kg/m² in the ITCZ.

As for the variability of the total amount of ozone in the atmospheric column, the impact of the variability of the total water vapour amount on the TOA BRF remains small, as seen in Table 3-9. The amount of water vapour may be fixed in the RTM LUTs at the mean value given the standard atmospheric profile in the tropics, and its variability be eventually translated as a radiometric noise in the computation of the uncertainty associated to the calibration coefficient determination. The FCI VIS0.9 band does not show any significant sensitivity to change in the total column water vapour.

Water vapour range (in kg/m ²)	Minimal relative abs. diff. in TOA BRF (PP)	Maximal relative abs. diff. in TOA BRF (PP)	Minimal absolute diff. in TOA BRF (PP)	Maximal absolute diff. in TOA BRF (PP)
50-60	0.08%	0.10%	0.000	0.001
40-50	0.08%	0.10%	0.000	0.001
30-40	0.08%	0.10%	0.000	0.001
20-30	0.07%	0.10%	0.000	0.001
20-60	0.30%	0.40%	0.002	0.002

Table 3-9 - Comparison of TOA BRF in the principal plane for different amounts of water vapour in the atmosphere, with a COT at 100 and an effective radius of 23µm, over land

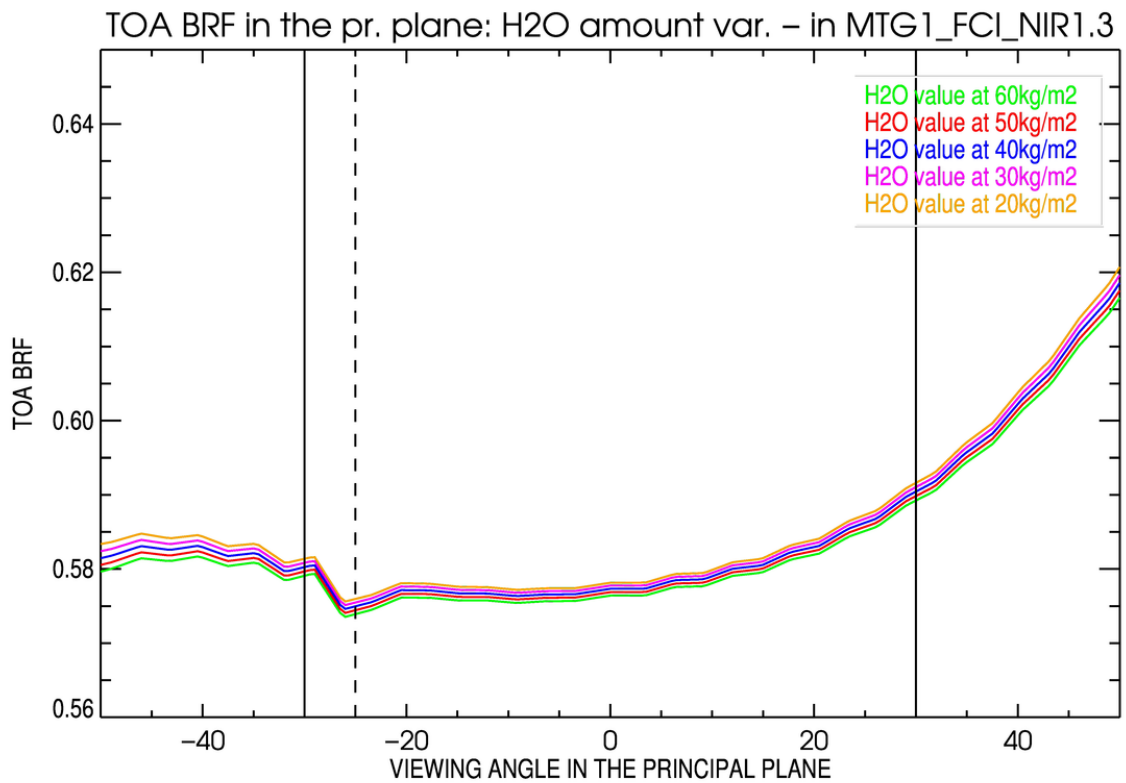
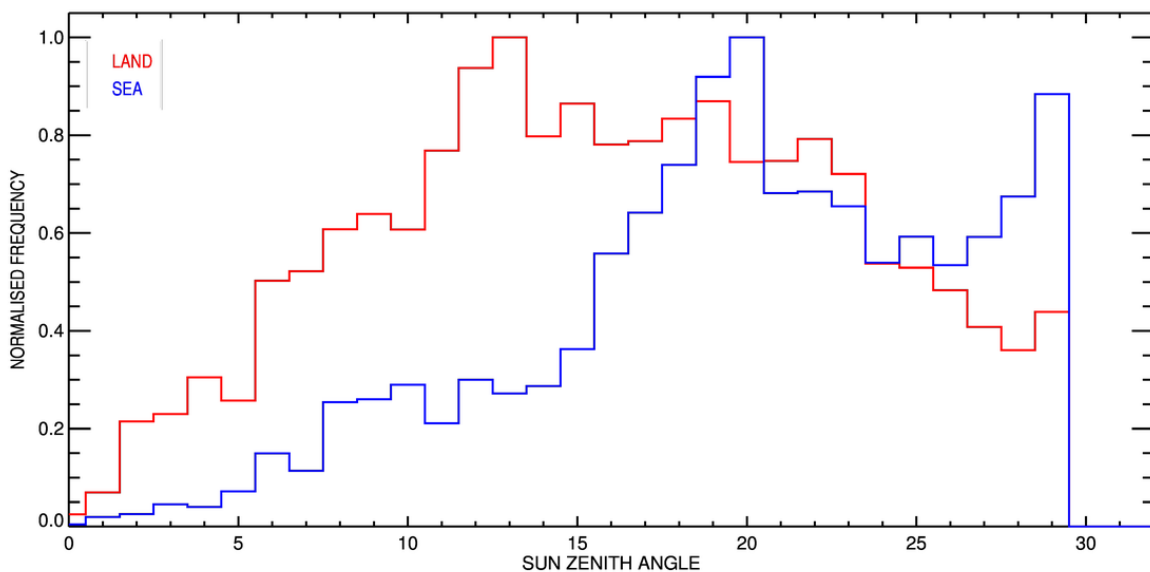


Figure 30 - Top Of Atmosphere Bi-Directional Factor in the Principal Plane for Meteosat MTG1 band, NIR1.3, with different values for the total amount of water vapour in the atmospheric column. The vertical dotted line is the zenithal sun angle at 25°, while the solid lines mark maximal viewing zenithal angle allowed.

3.4.7. Analysis of the actual observation conditions

The sensitivity analysis has been performed in the principal plane for a SZA set at 25°. These conditions tend to exacerbate the influence of the analysed parameters. The effects of these conditions with respect to the actual ones are now analysed. MSG3 data have been processed with the proposed algorithm and the distribution of SZA and VZA values of the identified DCC pixels analysed.



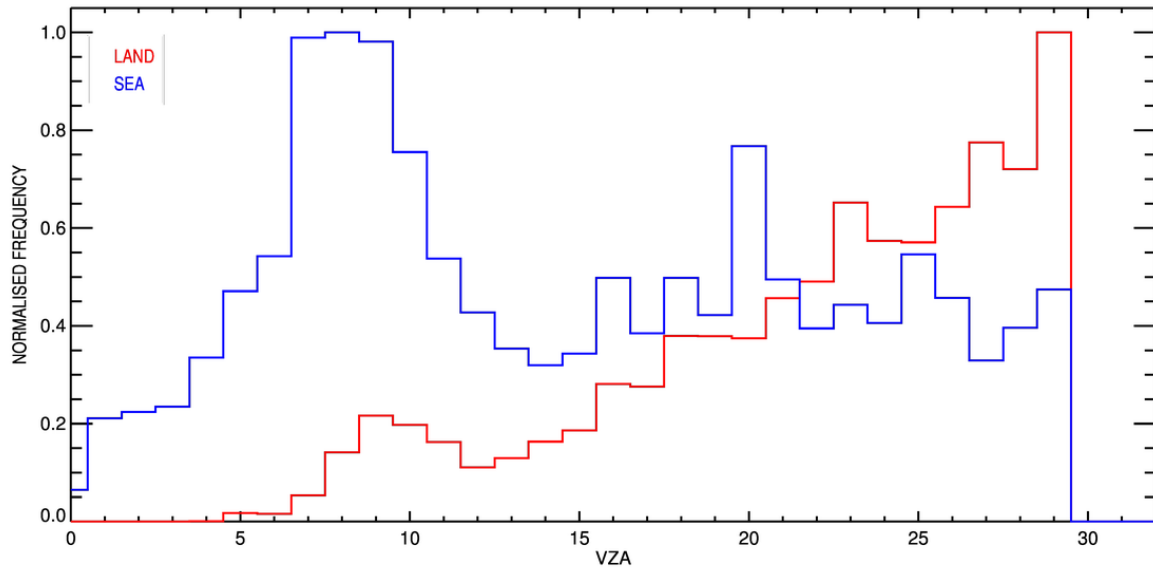


Figure 31: Distribution of the SZA and VZA values for the DCC pixels contributing to the calibration of MSG3 between 2013 and 2015. Red (blue) curve shows the DCC pixels identified over land (sea).

Results are shown on Figure 31 for land and sea pixels. Maximum distribution of SZA distribution exhibit different values over land and sea. Sea pixels tend to be identified with larger SZA values than land pixels. It indicates that DCC pixels are not identified at the same local time according to the type of surface. This type of surface has also an influence on the VZA distribution as a direct result of the localization of the African continent with respect to the sub-satellite point.

For each identified DCC during that period, the relative uncertainty on the simulated DCC TOA BRF has been estimated assuming an uncertainty of $\pm 5\mu\text{m}$ for the radius and ± 20 for the COT.

Table 3-10: Relative uncertainties due to an uncertainty of $\pm 5\mu\text{m}$ for the radius and ± 20 for the COT accounting for the actual observation geometry for DCC identification during the 2013-2015 period.

Band	Mean COT relative uncertainty	Mean radius relative uncertainty	Mean total relative uncertainty
VIS0.6	3.16%	0.48%	3.20%
VIS0.8	2.94%	0.01%	2.94%
NIR1.6	3.93%	28.94%	29.21%

Results are shown on Table 3-10 and are in very good agreement with those obtained in Sections (3.4.2) and (3.4.3). The distribution of these uncertainties is shown in Figure 32. The width of the distribution is pretty narrow indicating a limited sensitivity to the 0-30° angular configuration.

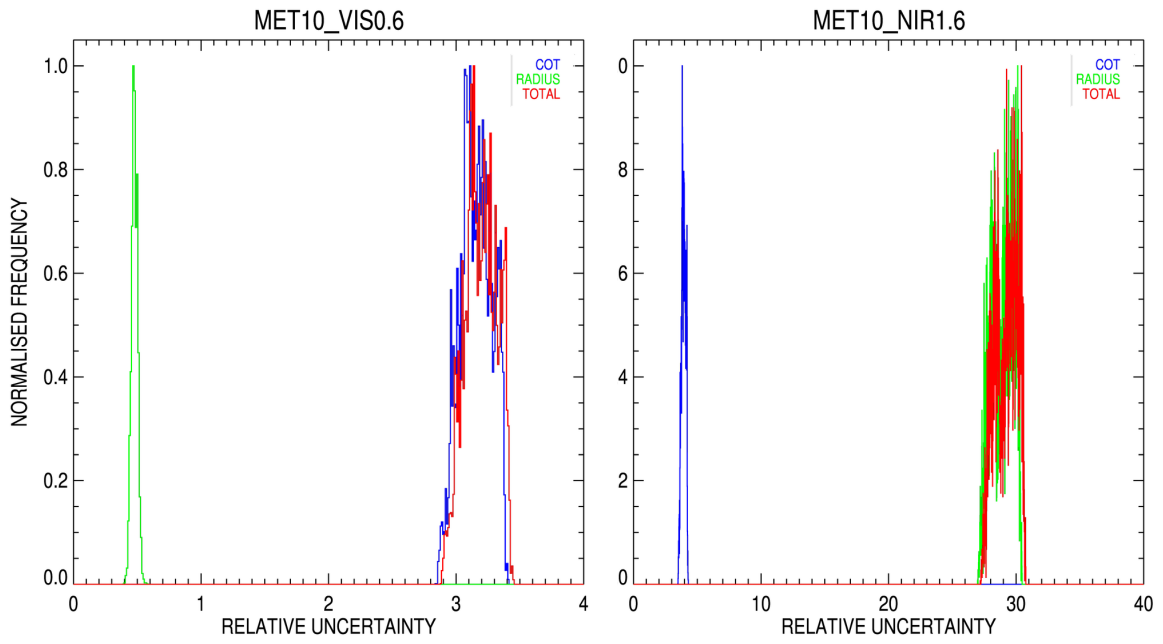


Figure 32: Distribution of the relative uncertainties due to an uncertainty of $\pm 5\mu\text{m}$ for the radius and ± 20 for the COT accounting for the actual observation geometry for DCC identification during the 2013-2015 period in the VIS0.6 band (left) and NIR1.6 (right).

4. ALGORITHM CONCEPT

The algorithm processes a number of periods of accumulation period of 30 days that are shifted by 5 days synchronized with the SSCC periods. The processing a new image during the accumulation period includes the following steps:

1. The multi-spectral identification of the potential DCC pixels (Section 4.1);
2. Generation of the multi-spectral calibration coefficient histograms with the selected pixels (Section 4.2);
3. The derivation of mean calibration coefficient and its uncertainty are produced for the considered shift period.

4.1. IDENTIFICATION PROCESS OF THE DCC PIXELS

Potential DCC pixels are searched in large areas defined over land and sea that differ for the ZDS and IODC regions (Figure 2). These regions are defined by two couples of coordinates, the minimal/maximal latitudes and the minimal/maximal longitudes. All the pixels within these regions of interest are processed one after the other, following each detailed step:

1. Removal of the pixels that do not correspond to the processed land/sea surface type.
2. Removal of the saturated pixels.
3. Removal of the pixels with a brightness temperature in band IR10.8 above 205K.
4. Application of uniformity test is performed in bands VIS0.6, VIS0.8, NIR1.6 and IR10.8. This test should be successful simultaneously in all bands in order to keep a pixel as a potential DCC. A pixel is rejected if the ratio of the standard deviation over the mean value is above the threshold value.
5. The 3x3 HRVIS pixels corresponding to the potential pixels that have successfully past the uniformity test are averaged.
6. If the solar and viewing zeniths are outside the range set to 0° to 30°, the pixel is rejected;
7. If the phase angle is below 5°, the pixel is disregarded;
8. The pixel data are saved, which comprise all angular information, the different counts, the geographical position as well as the coordinates.

4.2. CONSTRUCTION OF THE HISTOGRAMS

At the end of the 30-day accumulation period and when at least 3000 potential DCC pixels have been identified, the calibration process take place based on the calibration coefficient histograms. One histogram is built per spectral bands. The 3000 pixel threshold value ensures a proper statistical distribution.

Specifically, the generation of the histograms relies on the following processing steps:

1. The TOA radiance of each identified DCC pixels is extracted from the LUTs.
2. The calibration coefficient of each identified DCC pixel is computed in each band based on the observed count value and simulated TOA radiance;
3. The calibration coefficient histogram in each band is generated using bin value provided as setup parameter;
4. Extreme calibration coefficient values exceeding σ_{id} are rejected;
5. The mode of each distribution is determined;
6. The distribution is fitted with a Gaussian curve whose mean is set on the mode;

7. Only the pixels that are the closest to the mode are kept, within the range of the product of the standard deviation of the fitted Gaussian by the factor σ_{multi} – this condition has to be checked for every band simultaneously.
8. The mean calibration coefficient is taken equal to the mean of the fitted Gaussian, in each band;
9. The standard deviation of the fitted Gaussian is the uncertainty associated with the calibration coefficient for the shift period;
10. The pixels presents in all histograms and belonging to the 5-days period should be extracted for subsequent processing in SSCC.

An example of calibration coefficient histogram is shown on Figure 33 for Meteosat-10 over land pixels.

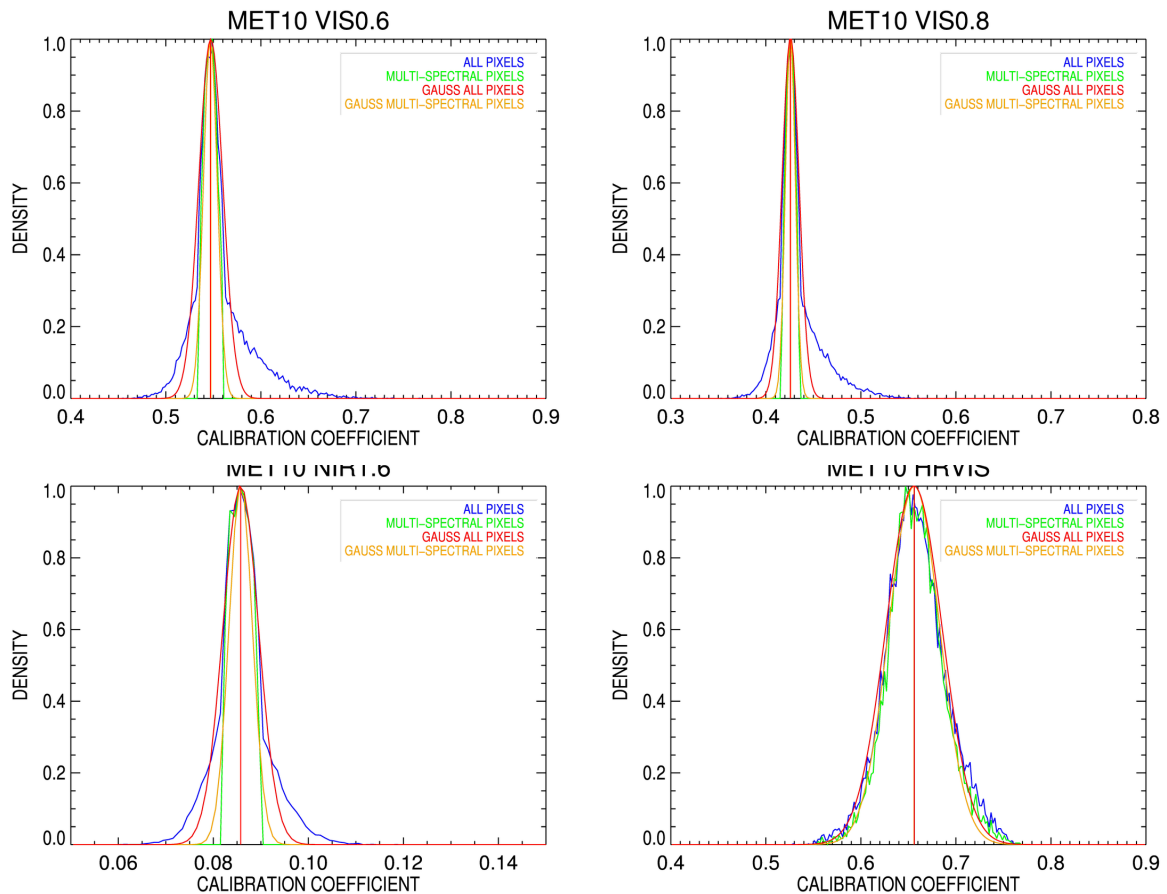


Figure 33 – Example of accumulated calibration coefficient histograms for Meteosat-10 over land for period 116 – 120 in 2013. The blue line indicates all the accumulated pixels, the red line the fitted Gaussian curve on this histogram, the green lines shows the pixels that fulfil the multi-spectral conditions and the orange curve the fitted Gaussian of the multi-spectral population.

4.3. (HR)VIS BAND CONSIDERATION

For Meteosat First Generation, only one solar spectral band is available. The multi-spectral filtering is therefore not relevant.

For SEVIRI, because of the specific scanning mode of the HRVIS band, it is difficult to use this band for DCC calibration over the Atlantic Ocean as most of the scanning window is located over the Africa during the selected daily interval, i.e., 10h – 14h (Figure 34). Consequently, the multi-spectral uniformity test is not performed in that band.

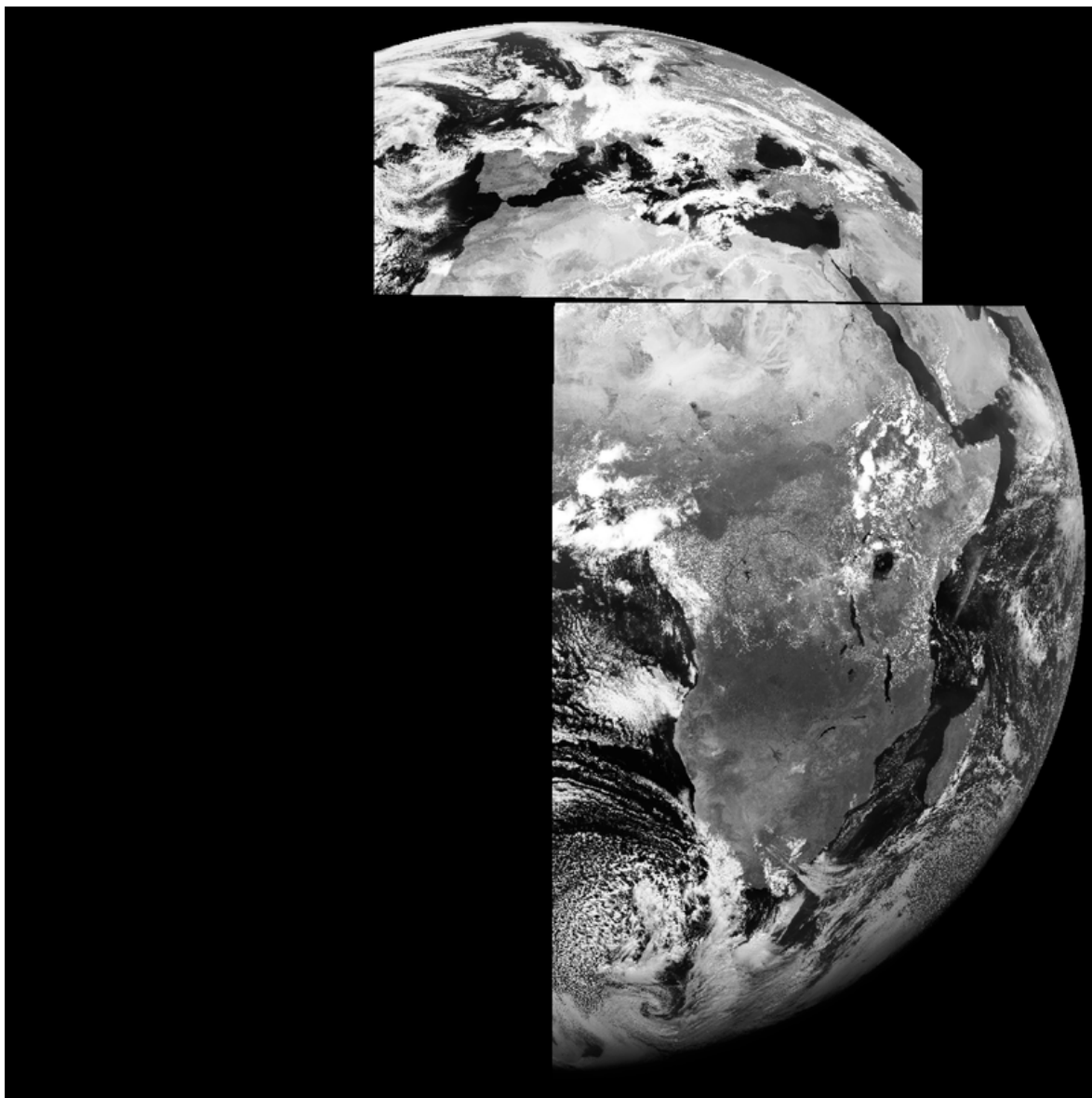


Figure 34 – Example of HRVIS acquisition mode for slot 48 (12h) acquired 01/06/2013 by Meteosat-10.

4.4. SETUP PARAMETERS

The following setup parameter values are used for the processing of SEVIRI data at ZDS.

Parameter	Symbol	Units	Value			
			VIS0.6	VIS0.8	NIR1.6	HRVIS
Accumulation period		Day	30			
Shift of the accumulation period		Day	5			
First image		Hour	10:00			
Last image			14:00			
Minimum number of pixels in the histogram			3000			
Calibration coefficient distribution outlier removal	σ_{id}	sigma	3			
Calibration coefficient multi-spectral analysis	σ_{multi}	sigma	1			
Calibration coefficient bin size		$\text{Wm}^{-2}\text{sr}^{-1}\mu\text{m}^{-1}/\text{DC}$	0.002	0.002	0.001	0.002

5. CONSISTENCY ANALYSIS AND EVALUATION

This Section covers partially WP3 and contains the sensitivity analysis performed on DCC pixel identification criteria for the defined RM. As already stated, pixel identification and RM characterization are strongly connected within the SSCC approach. Hence, the fine-tuning of the identification criteria is closely connected to the DCC RM parameter values and *vice versa*. The impact of the criteria set in the Sections (2) and (3) on the derived calibration coefficients is analysed. This sensitivity analysis should be used to help the definition of the parameters characterising the DCC RM.

5.1. EXPERIMENTAL SETUP

The sensitivity analysis to the identification criteria and RM parameter value is based on the processing of Meteosat-10 data for the first six months of 2013, over land and/or sea. Standard identification criteria are those of Table 2-6, except when expressly mentioned.

In the following plots, the calibration coefficients are represented by crosses, whose horizontal bar marks the value of the computed mean (as explained in section 4.2) of the fitted Gaussian while the vertical bar represents the uncertainty associated to the value, and is taken equal to the standard deviation of the same Gaussian. The black horizontal dashed line gives the value of the calibration coefficient as obtained Libya-4 CEOS PICS for comparison purposes as described in Govaerts et al (2013). The dotted lines represent the $\pm 3\%$ uncertainties.

In order to study the impact of identification and DCC RM parameters on the calibration coefficients, the algorithm has been run while varying the following parameters, one at a time:

- the brightness temperature threshold (Section 5.2.1.1);
- the latitude coverage (Section 5.2.1.2);
- the COT (Section 5.2.2.1);
- the effective radius (Section 5.2.2.2).

5.2. SENSITIVITY ANALYSIS TO THE IDENTIFICATION CRITERIA

5.2.1. DCC identification criteria

5.2.1.1. Brightness temperature threshold

As seen on Figure 3, taken from the study of Sohn [DR5], the DCC top brightness temperature can vary between 190 and 205K – it is one of the main identification parameters and its influence on the calibration coefficients is therefore analysed.

- Over land

The legend for the four following graphs, depicting the calibration coefficient time series, in band VIS0.6 (on Figure 35), VIS0.8 (on Figure 36), NIR1.6 (on Figure 37) and HRVIS (on Figure 38), is:

- In red: calibration coefficient for a temperature threshold at 205K;
- In coral: calibration coefficient for a temperature threshold at 200K;
- In orange: calibration coefficient for a temperature threshold at 195K;
- In yellow: calibration coefficient for a temperature threshold at 190K.

In the NIR1.6 band, the lower the temperature threshold, the larger the uncertainty associated with a given temporal sampling over 5 days. This effect, though present, is far less pronounced in the other bands.

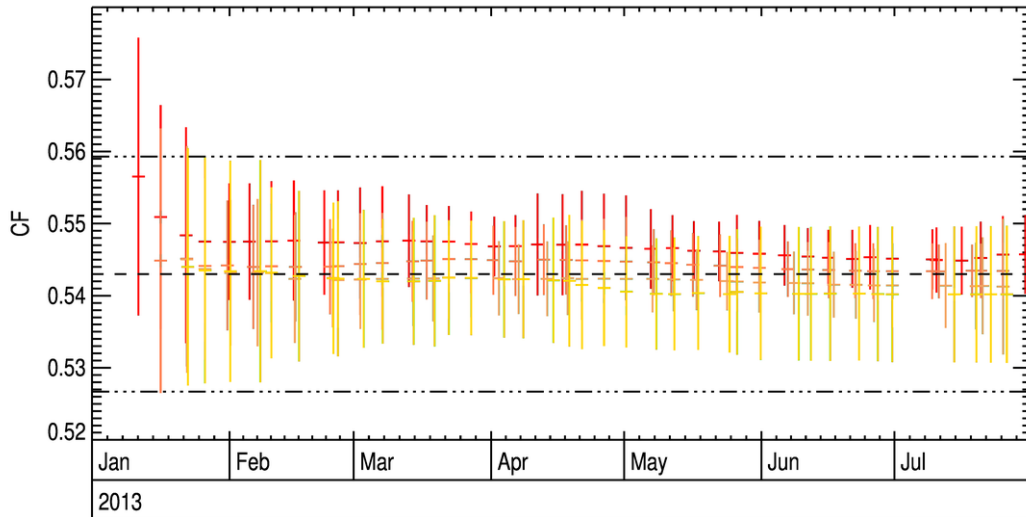


Figure 35 - Calibration coefficient computed with Meteosat 10 data of the first 6 months of 2013, over the ZDS region, on land, in the VIS 0.6 band. The following colour code is used: 205K (red), 200K (coral), 195K (orange), 190K (yellow). The black horizontal dashed line gives the value of the calibration coefficient as obtained Libya-4 CEOS PICS for comparison purposes. The dotted lines represent the uncertainties associated with this reference value, within a 3% margin.

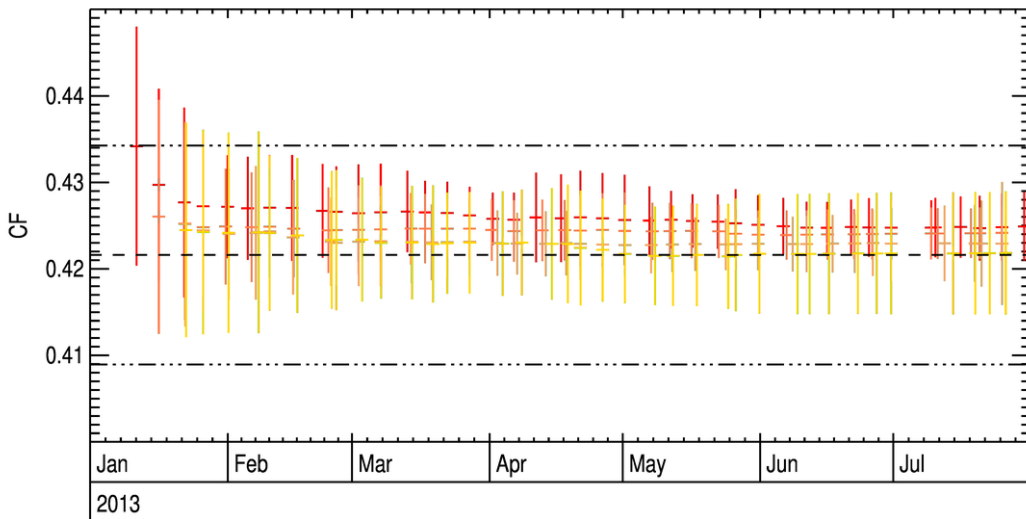


Figure 36 – Same as Figure 35, in the VIS 0.8 band.

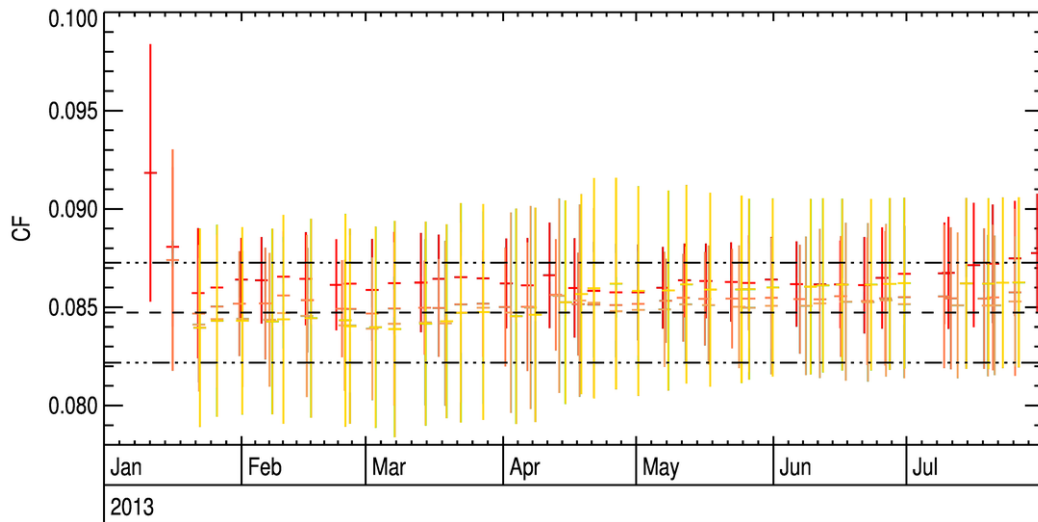


Figure 37 - Same as Figure 35, in the NIR 1.6 band.

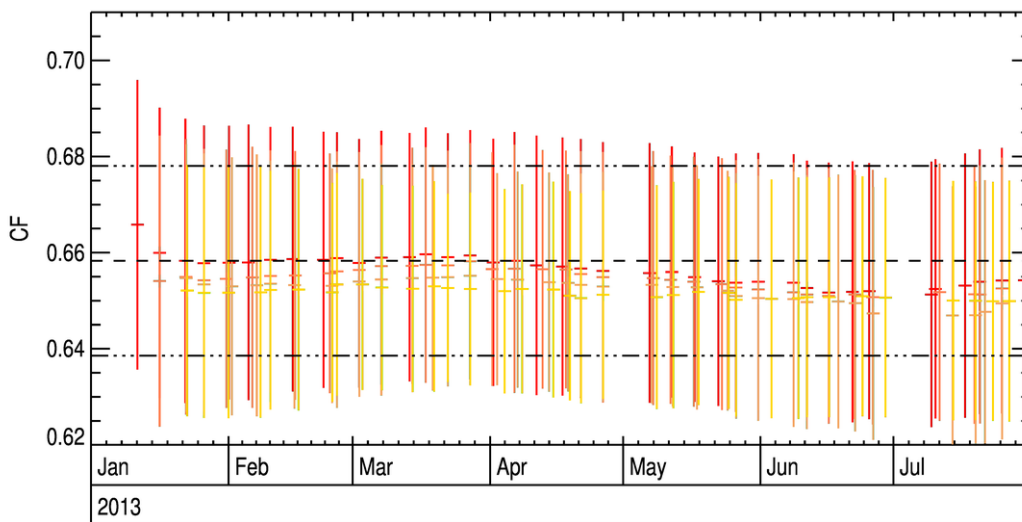


Figure 38 - Same as Figure 35, in the HRVIS band.

- Over sea

The legend for the four following graphs, depicting the calibration coefficient time series, in band VIS0.6 (on Figure 39), VIS0.8 (on Figure 40), NIR1.6 (on Figure 41) and HRVIS (on Figure 42), is:

- In ultramarine blue: calibration coefficient for a temperature threshold at 205K;
- In cerulean blue: calibration coefficient for a temperature threshold at 200K;
- In light blue: calibration coefficient for a temperature threshold at 195K;
- In baby blue: calibration coefficient for a temperature threshold at 190K.

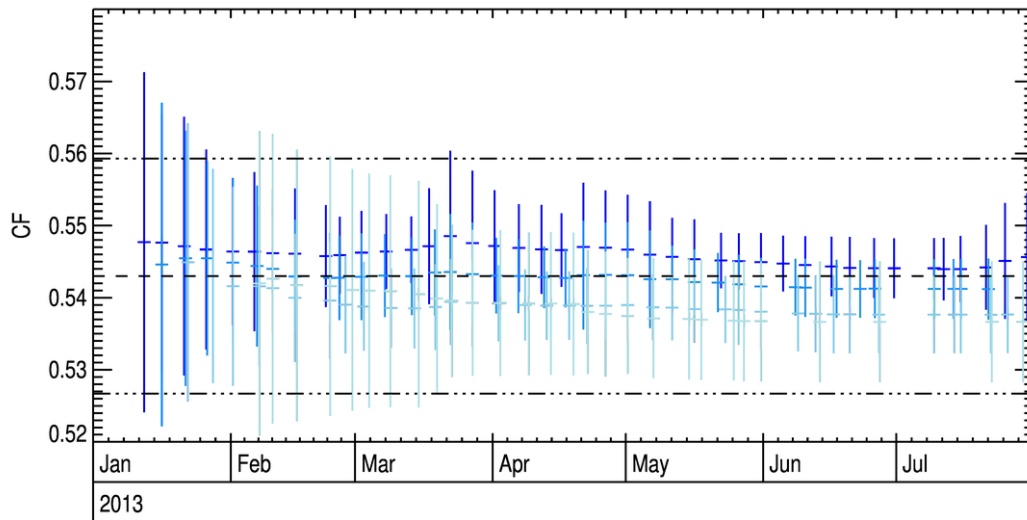


Figure 39 - Calibration coefficient computed with Meteosat 10 data of the first 6 months of 2013, over the ZDS region, on sea, in the VIS 0.6 band for threshold brightness temperature varying from 205K to 190K by step of 5K. The lighter the blue, the colder the threshold temperature. The black horizontal dashed line is mean calibration coefficient obtained over Libya-4 CEOS PICS. The dotted lines represent the $\pm 3\%$ uncertainties.

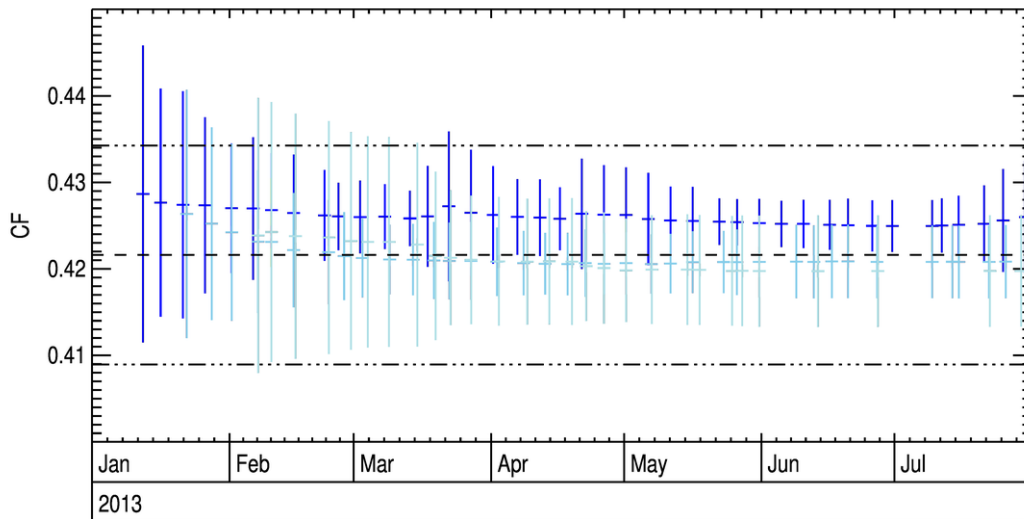


Figure 40 – Same as Figure 39, in the VIS 0.8 band.

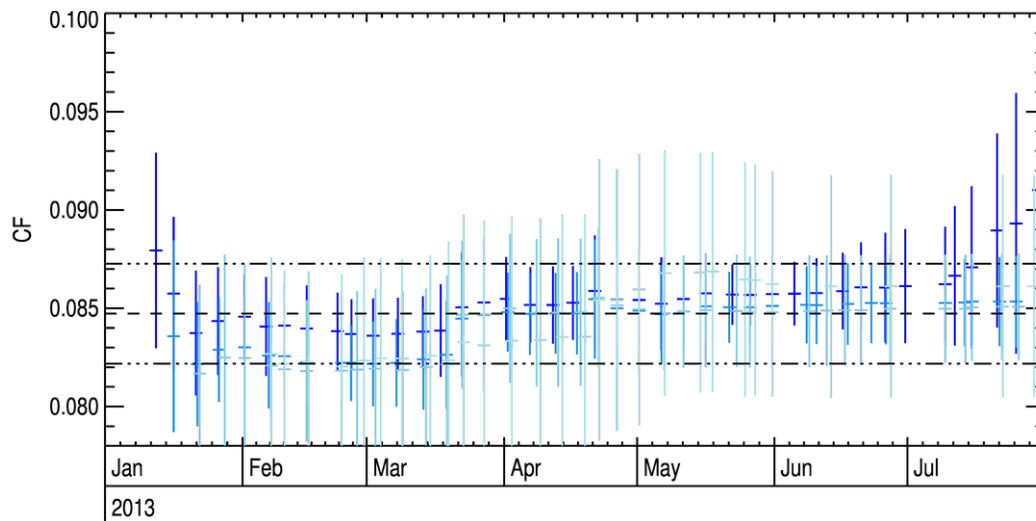


Figure 41 - Same as Figure 39, in the NIR1.6 band.

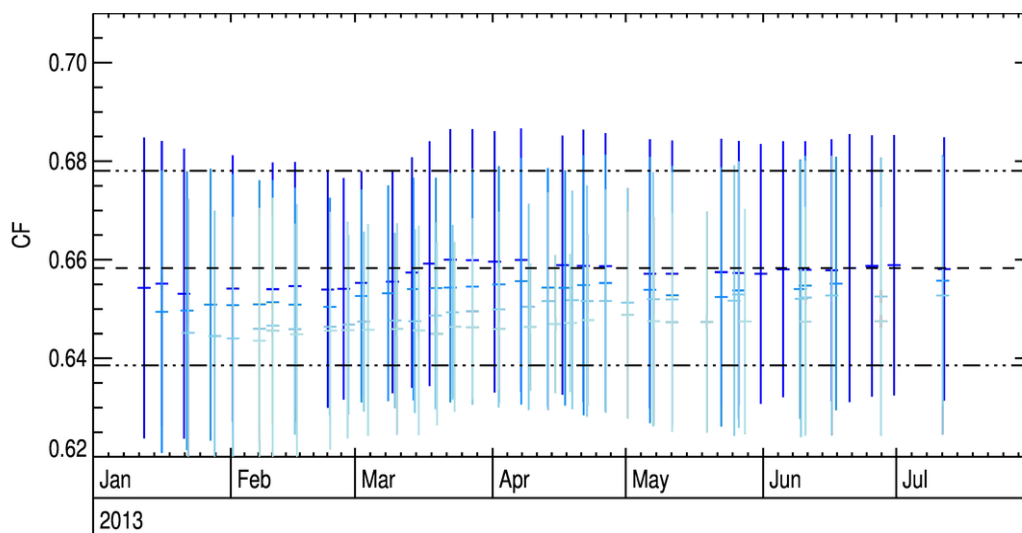


Figure 42 - Same as Figure 39, in the HRVIS band.

The same remark can also be applied for the DCCs calibration over sea. A warmer temperature threshold allows the algorithm to perform statistics on a larger population, thus making the sampling more accurate when selecting DCC pixels whose microphysical parameters well match the ones implemented in the RM.

5.2.1.2. Latitude Coverage: Rapid Scan Mode

The frequency of rapid scan is not expected to provide additional information. Rapid scan acquisition mode is thus simulated reducing the spatial coverage to 15°N without processing data at a higher temporal resolution.

Over land, reduced latitude coverage results in a depletion of the DCCs population – hence the absence of calibration coefficient computation during certain periods, and a larger uncertainty associated with the coefficients effectively computed, during the winter – when the ITCZ migrate north the Equator. It should be noted, however, that even with this restriction on the DCC population, the drift of the sensor is visible over 3 years, and correctly follows the results of Meteosat-10 calibration over the ZDS.

Over sea, there is no computation for the calibration coefficients, at any period of the year, due to the lack of sea-borne DCCs in those areas.

- Over land

The legend for the four following graphs, depicting the calibration coefficient time series, in band VIS0.6 (on Figure 43), VIS0.8 (on Figure 44), NIR1.6 (on Figure 45) and HRVIS (on Figure 46), is:

- In yellow: calibration coefficient at COT = 100 and an effective radius of 23 μ m, while using only the region covered by the Rapid Scan Mode;
- In red: calibration coefficient at COT = 100 and an effective radius of 23 μ m, while using the full ZDS region.

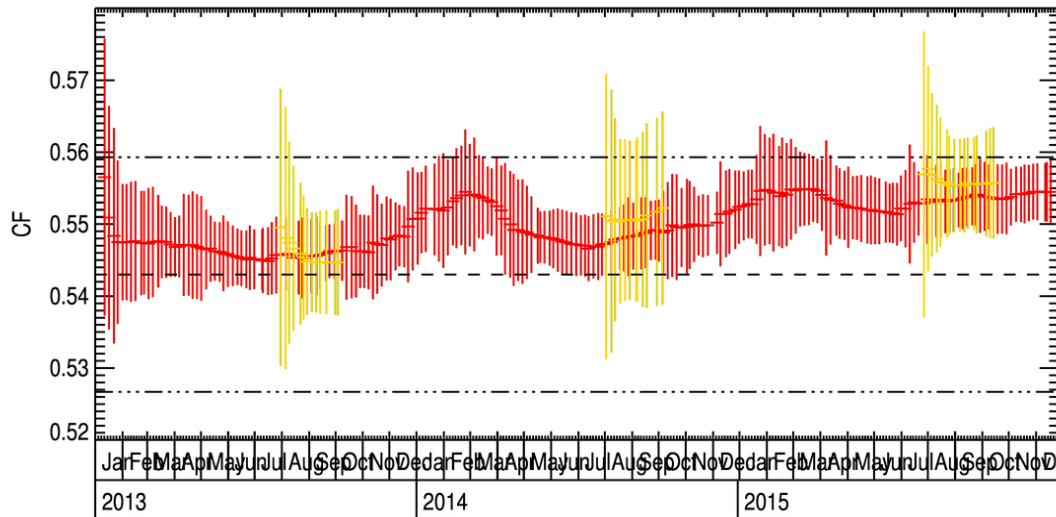


Figure 43 - Calibration coefficient computed with Meteosat 10 data of the years 2013, 2014, 2015, over the ZDS region and the Rapid Scan Mode area, on land, in the VIS0.6 band. Red curve: normal acquisition mode, yellow : rapid scan acquisition area. The black horizontal dashed line is mean calibration coefficient obtained over Libya-4 CEOS PICS. The dotted lines represent the $\pm 3\%$ uncertainties.

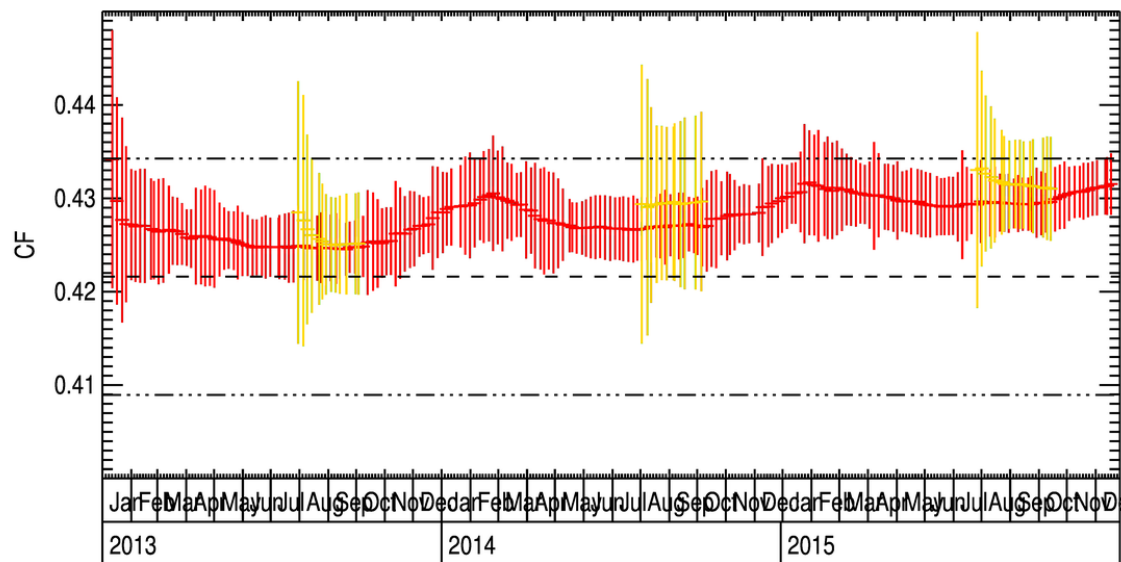


Figure 44 – Same on Figure 43, in the VIS0.8 band.

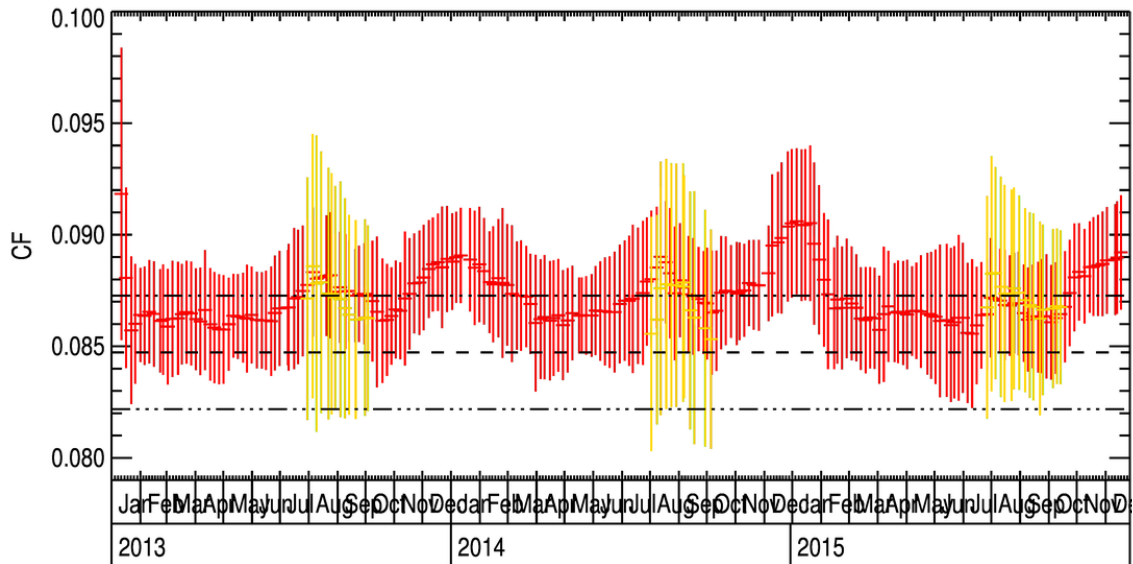


Figure 45 - Same on Figure 43, in the NIR1.6 band.

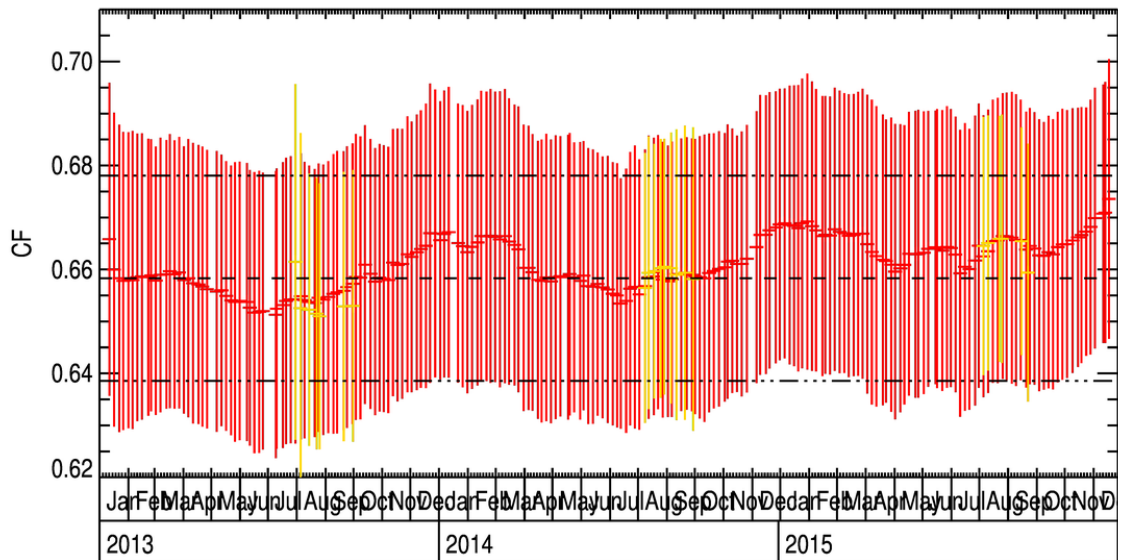


Figure 46 - Same on Figure 43, in the HRVIS band.

5.2.2. DCC RM parameters

We analyse now the sensitivity of the DCC calibration method to the RM parameter values.

5.2.2.1. Cloud Optical Thickness

- Over land

The legend for the four following graphs, depicting the calibration coefficient time series, in band VIS0.6 (on Figure 47), VIS0.8 (on Figure 48), NIR1.6 (on Figure 49) and HRVIS (on Figure 50), is:

- In light brown: calibration coefficient at COT = 80, for a fixed effective radius of 23µm;
- In red: calibration coefficient at COT = 100, for a fixed effective radius of 23µm;
- In dark brown: calibration coefficient at COT = 120, for a fixed effective radius of 23µm;

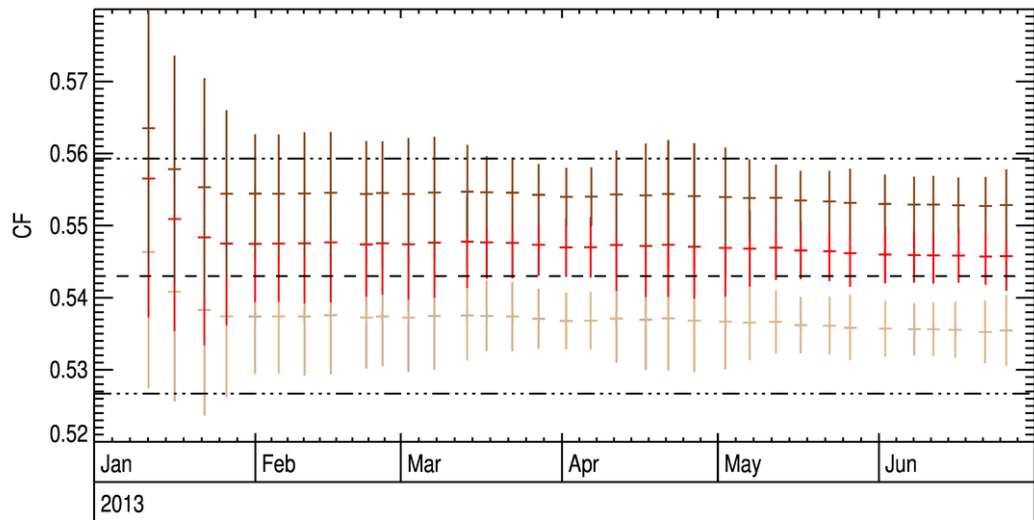


Figure 47 - Calibration coefficient computed with Meteosat 10 data of the first 6 months of 2013, over the ZDS region, on land, in the VIS0.6 band. The following colour code is used: COT = 80 (light brown), COT = 100 (red), COT = 120 (dark brown). The black horizontal dashed line is mean calibration coefficient obtained over Libya-4 CEOS PICS. The dotted lines represent the $\pm 3\%$ uncertainties.

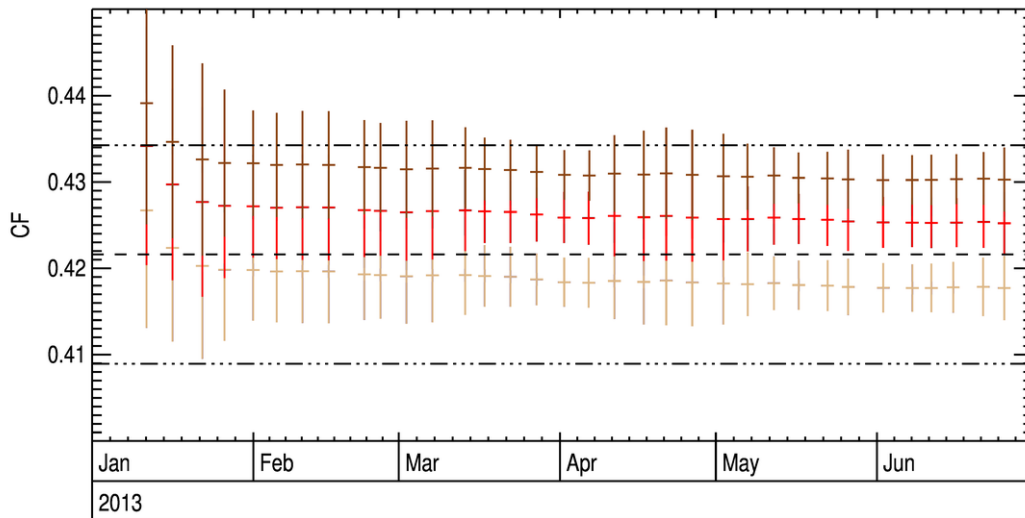


Figure 48 – Same as Figure 47, in the VIS0.8 band.

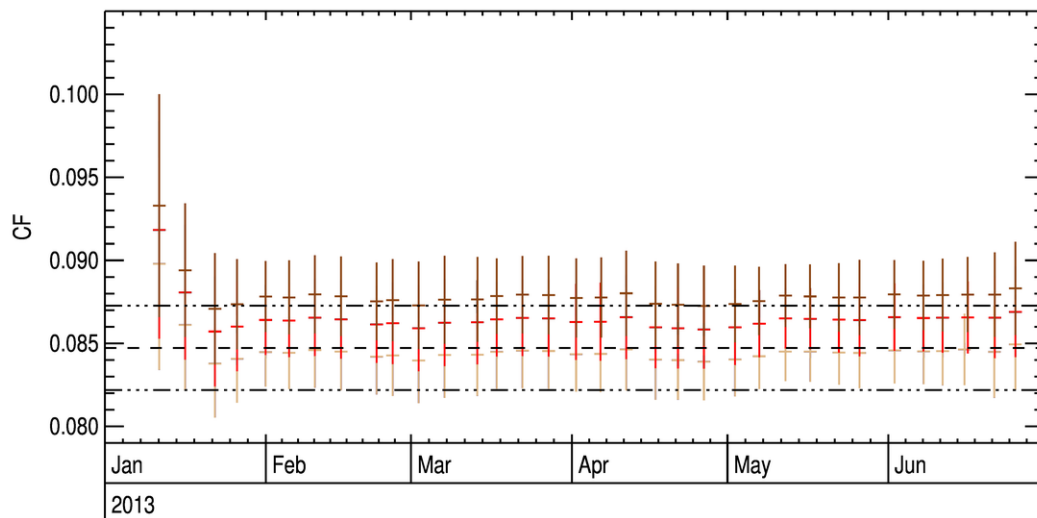


Figure 49 – Same as Figure 47, in the NIR1.6 band.

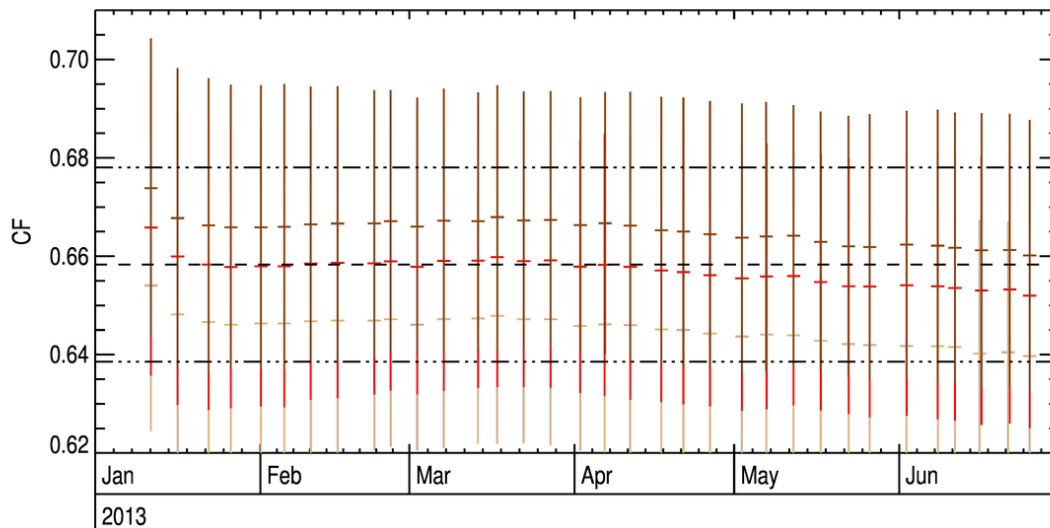


Figure 50 - Same as Figure 47, in the HRVIS band.

In the visible solar bands, a change of $\pm 20\%$ of the COT translates into change of about $\pm 1\text{-}2\%$ of the calibration coefficient. The observed sensitivity of the NIR1.6 band to COT results from the cloud vertical profile scaling as already explained in Section (3.4.2).

- Over sea

The legend for the four following graphs, depicting the calibration coefficient time series, in band VIS0.6 (on Figure 51), VIS0.8 (on Figure 52), NIR1.6 (on Figure 53) and HRVIS (on Figure 54), is:

- In cyan: calibration coefficient at COT = 80, for a fixed effective radius of $25\mu\text{m}$;
- In blue: calibration coefficient at COT = 100, for a fixed effective radius of $25\mu\text{m}$;
- In navy: calibration coefficient at COT = 120, for a fixed effective radius of $25\mu\text{m}$;

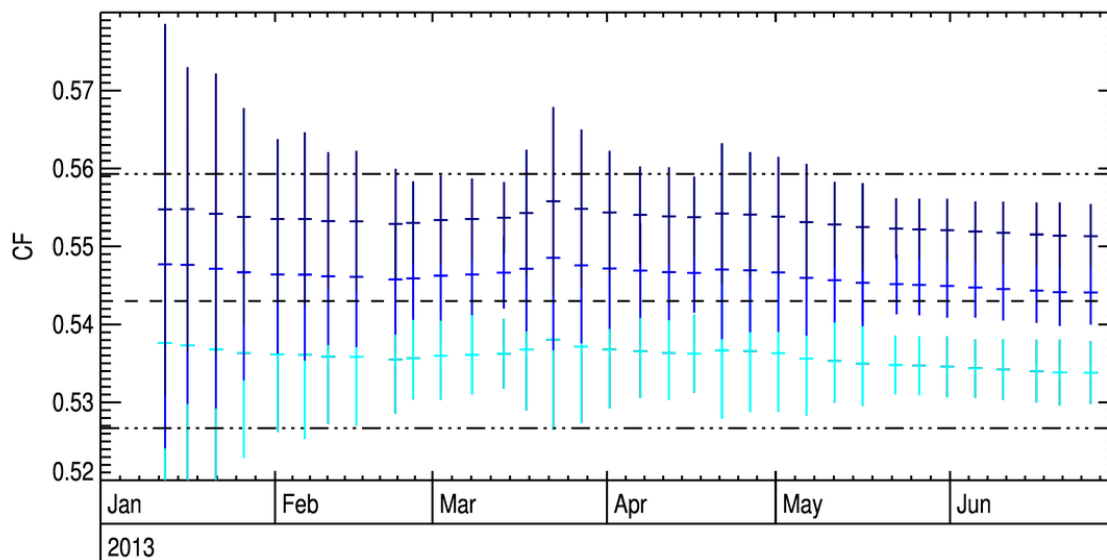


Figure 51 - Calibration coefficient computed with Meteosat 10 data of the first 6 months of 2013, over the ZDS region, on sea, in the VIS0.6 band. The following colour coding is used: COT = 80 (cyan), COT = 100 (blue) COT = 120 (navy blue). The black horizontal dashed line is mean calibration coefficient obtained over Libya-4 CEOS PICS. The dotted lines represent the $\pm 3\%$ uncertainties.

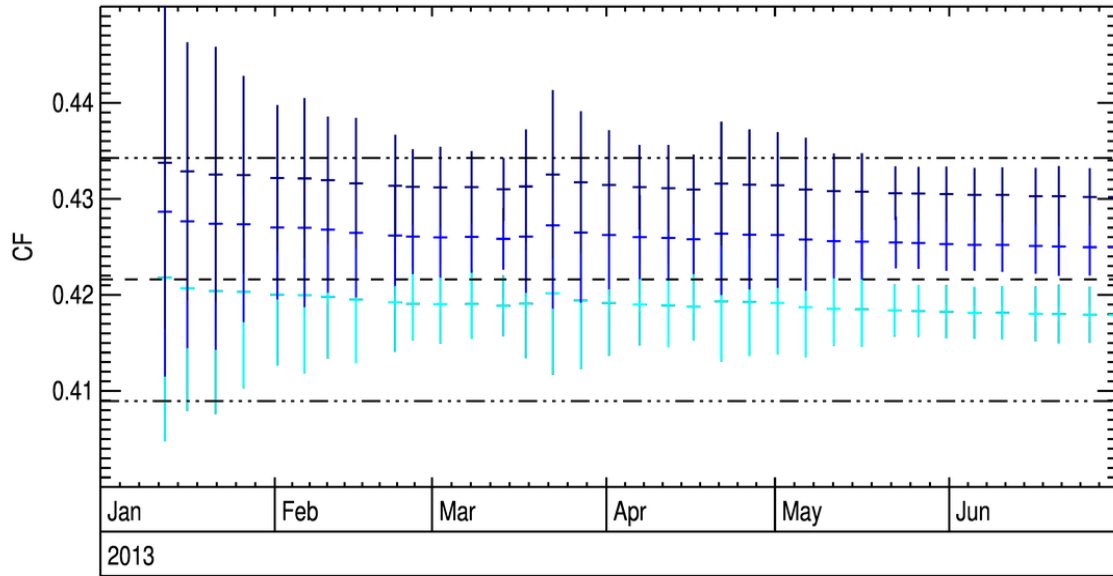


Figure 52 – Same as Figure 51, in the VIS0.8 band.

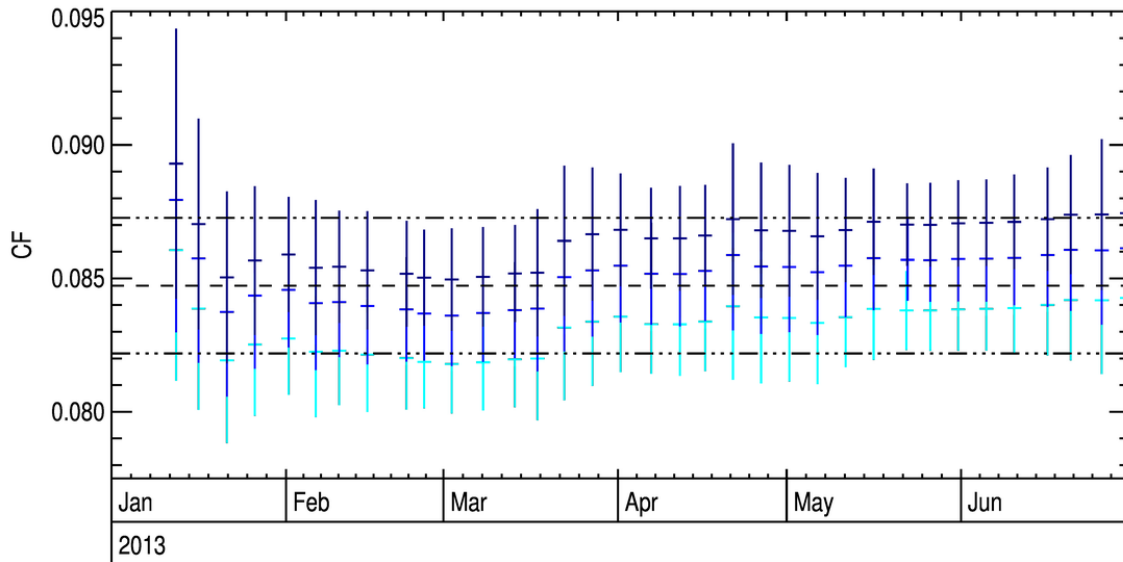


Figure 53 – Same as Figure 51, in the NIR1.6 band.

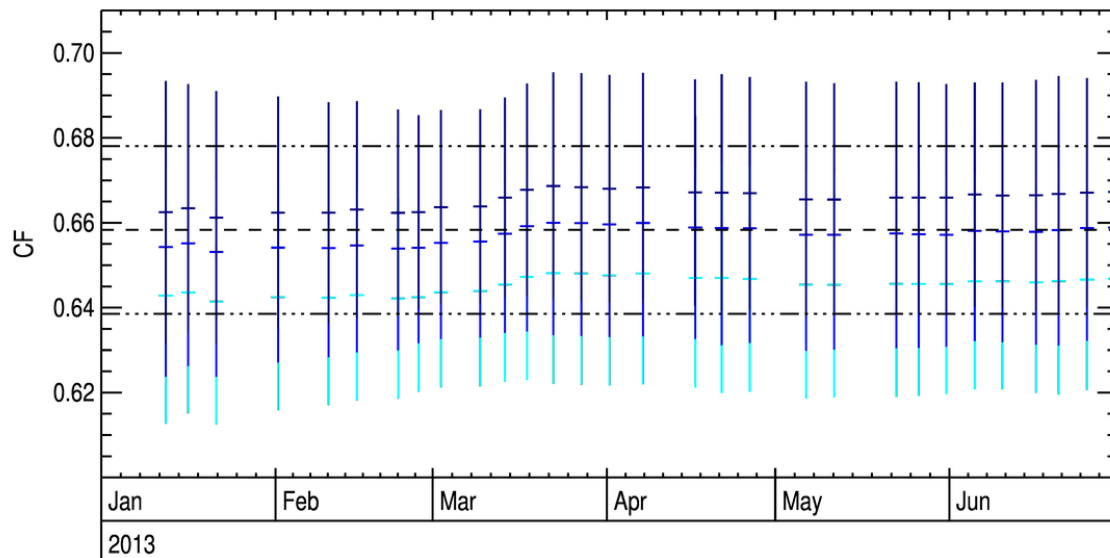


Figure 54 - Same as Figure 51, in the HRVIS band.

5.2.2.2. Effective Radius

According to Sohn et al. (cf. [DR5]) who analysed the MODIS cloud product, the effective radius exhibits a slight difference between sea and land as can be seen on Figure 5. From the statistics pulled from the MODIS products, the effective radius over sea is about 25µm. Over land, values range between 20 to 26µm. An average value of 23µm is therefore recommended. The following sensitivity analysis shows that the same conclusions can be drawn while using the RTMOM RTM.

- Over land

The legend for the four following graphs, depicting the calibration coefficient time series, in band VIS0.6 (on Figure 55), VIS0.8 (on Figure 56), NIR1.6 (on Figure 57) and HRVIS (on Figure 58), is:

- In dark brown: calibration coefficient at effective radius of 25µm, for a fixed COT = 100;
- In red: calibration coefficient at effective radius of 23µm, for a fixed COT = 100;
- In pink: calibration coefficient at effective radius of 20µm, for a fixed COT = 100;
- In light brown: calibration coefficient at effective radius of 15µm, for a fixed COT = 100.

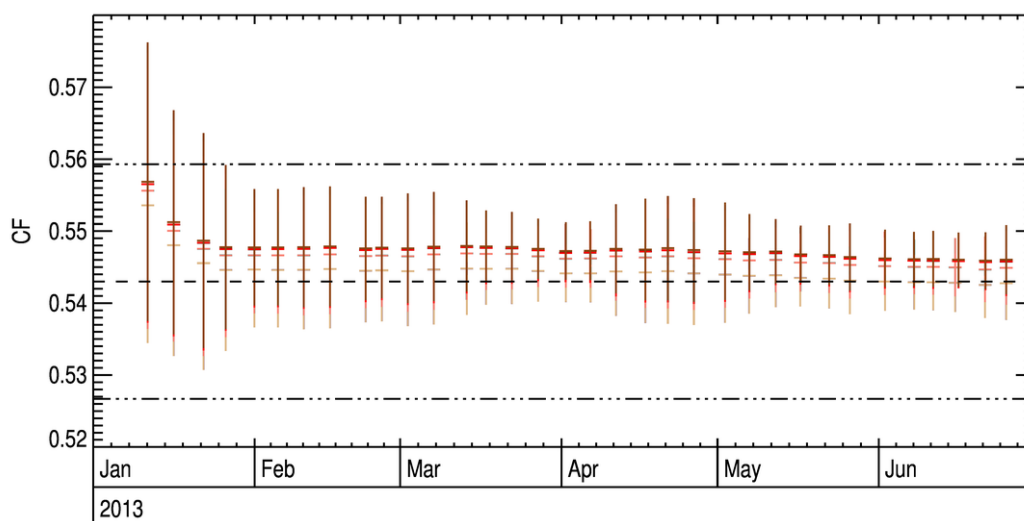


Figure 55 - Calibration coefficient computed with Meteosat 10 data of the first 6 months of 2013, over the ZDS region, on land, in the VIS0.6 band.

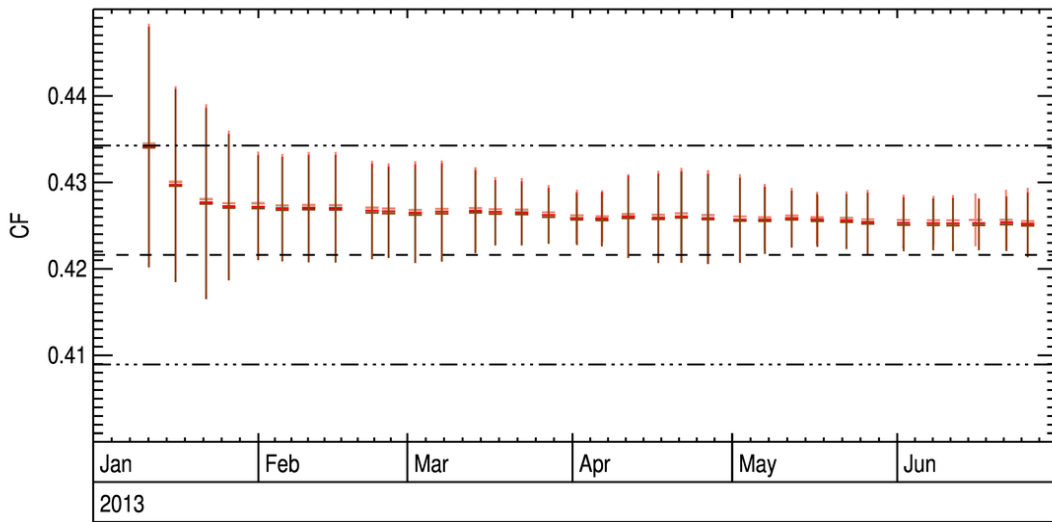


Figure 56 – Same as Figure 55, in the VIS0.8 band.

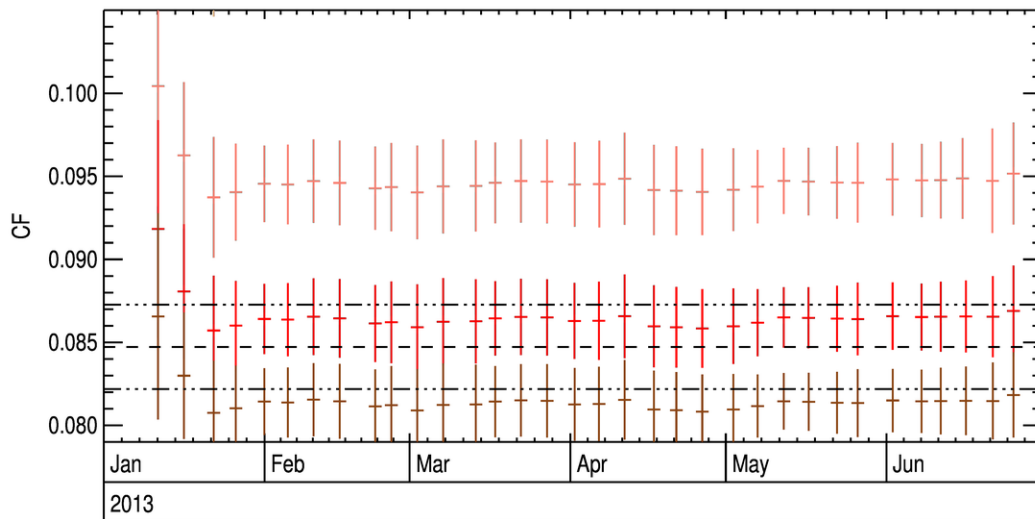


Figure 57 - Same as Figure 55, in the NIR1.6 band.

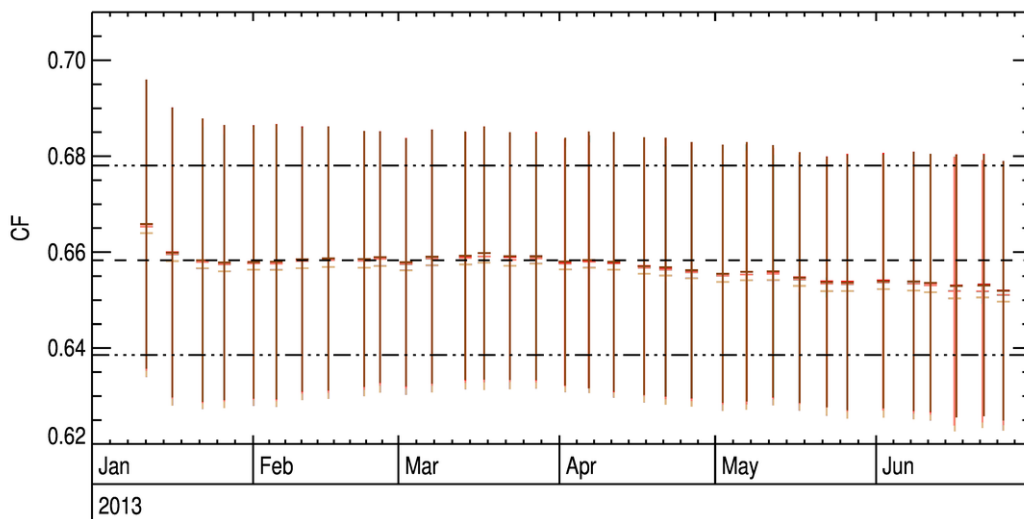


Figure 58 - Same as Figure 55, in the HRVIS band.

The solar visible bands exhibit almost no sensitivity to the effective radius value. On the contrary, the NIR1.6 band is extremely sensitive to this parameter. From the Figure 57, it can be deduced that the only acceptable value for the land-borne DCCs is an effective radius of 23 μm – value matching the study of Sohn [DR5]. The effects of the multi-spectral histogram analysis is also clearly visible in the VIS0.6 and 0.8 band where the derived calibration coefficients converge toward the one derived over Libya-4 after several periods.

- Over sea

The legend for the four following graphs, depicting the calibration coefficient time series, in band VIS0.6 (on Figure 59), VIS0.8 (on Figure 60), NIR1.6 (on Figure 61) and HRVIS (on Figure 62), is:

- In cyan: calibration coefficient for an effective radius of 20 μm , for a fixed COT = 100;
- In blue: calibration coefficient for an effective radius of 25 μm , for a fixed COT = 100;
- In navy: calibration coefficient for an effective radius of 30 μm , for a fixed COT = 100;

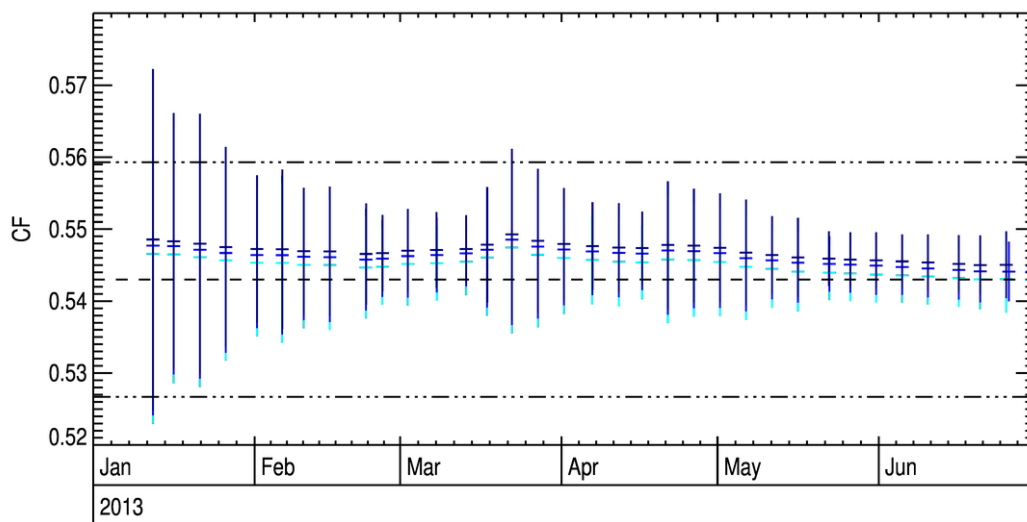


Figure 59 - Calibration coefficient computed with Meteosat 10 data of the first 6 months of 2013, over the ZDS region, on sea, in the VIS0.6 band.

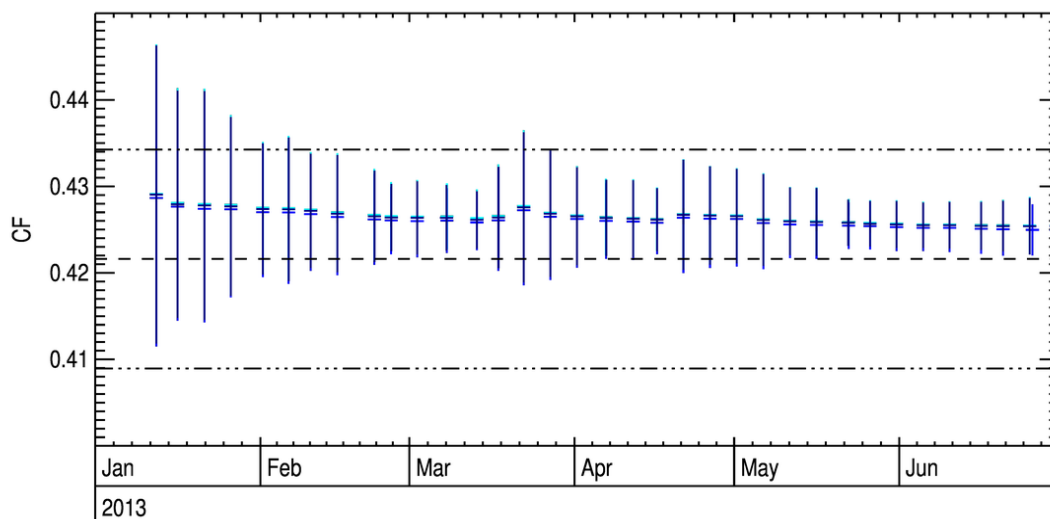


Figure 60 – Same as Figure 59, in the VIS0.8 band.

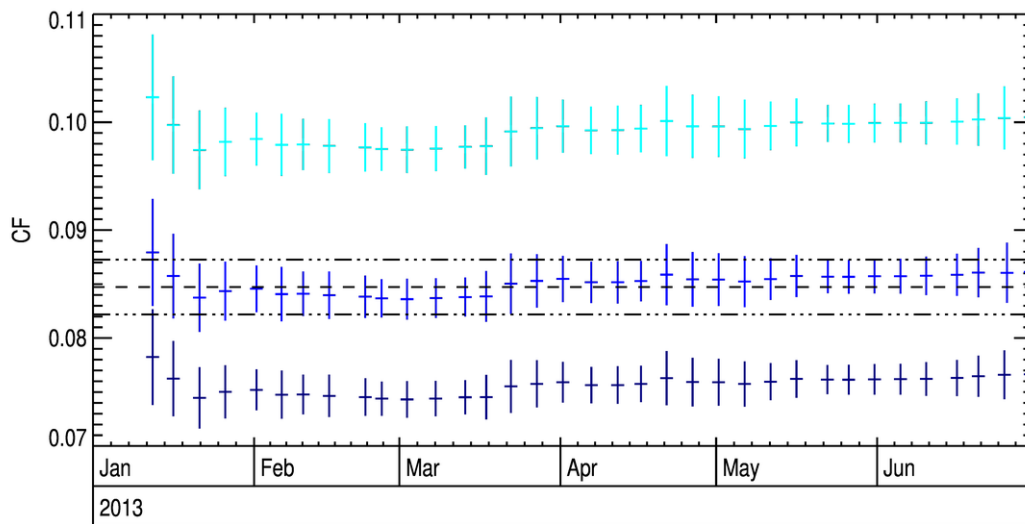


Figure 61 - Same as Figure 59, in the NIR1.6 band.

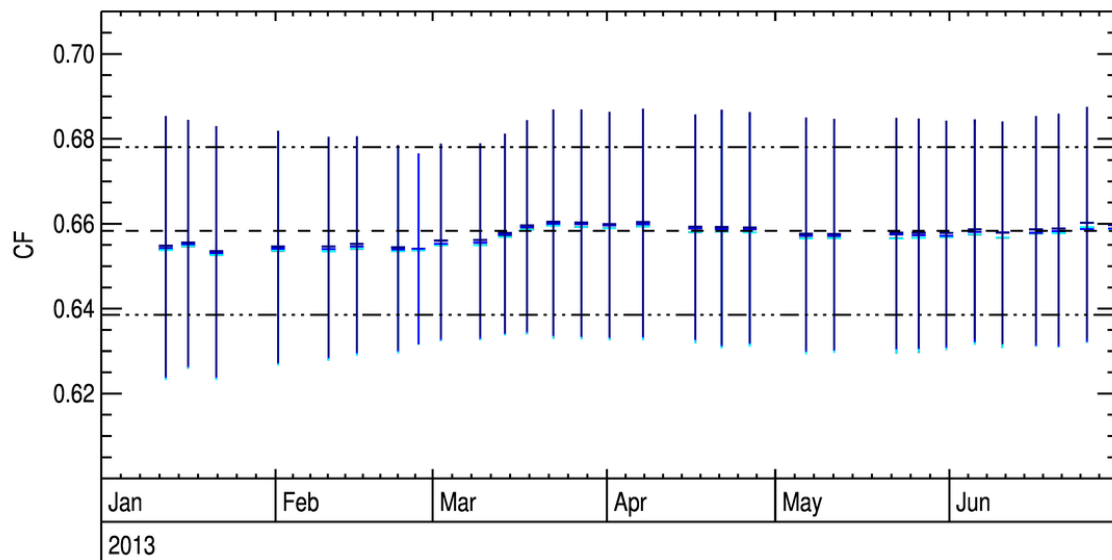


Figure 62 - Same as Figure 59, in the HRVIS band

The conclusion of the sensitivity analysis on the effective radius, for land-borne DCCs, applies for the sea-borne DCCs. The NIR1.6 band points to a correct effective radius value of 25 μ m, in perfect agreement with the study of Sohn, as can be seen on the Figure 5. It should be noted that smaller effective radius for the cloud top height means brighter TOA BRF and therefore higher calibration coefficients.

6. SYSTEMATIC ALGORITHM EVALUATION

The proposed algorithm has been evaluated on a series of Meteosat First and Second Generation observations acquired over the ZDS and IODC areas (Table 6-1). The corresponding observed radiances are generated using the TOA spectral radiance simulated by following the recommendations drawn from the sensitivity analysis performed in the section 3.4 and convoluted in the respective Sensor Spectral Response (SSR) of the processed radiometric bands.

Mission	Coverage	Satellite	IR band	Calib. band	Period
MFG	ZDS	Met-7	IR	VIS	2005
MFG	IODC	Met-7	IR	VIS	2007
MSG	ZDS	Met-8	IR10.8	VIS0.6, VIS0.8, NIR1.6 and HRVIS	2005
MSG	IODC	Met-8	IR10.8	VIS0.6, VIS0.8, NIR1.6 and HRVIS	2016 -2017
MSG	ZDS	Met-10	IR10.8	VIS0.6, VIS0.8, NIR1.6 and HRVIS	2013 - 2015

Table 6-1 - List of data on which the DCC identification will be applied in the framework of this study.

6.1. EFFECT OF HRVIS SCANNING MODE

The effect of the HRVIS band acquisition mode is analysed first. As stated in Section (4.2), it is expected that this specific acquisition mode affects the possibility of detecting DCC over the Atlantic Ocean. For that purpose, Meteosat-10 data have been processed for year 2013 over land and sea looking at the effects of including the HRVIS band in the multi-spectral identification tests. These tests are:

- The multi-spectral uniformity criteria;
- The presence of a pixel in all spectral histograms.

The data have been processed first applying the multi-spectral tests including the HRVIS. The data have been next processed excluding the HRVIS data from this test. In that case, pixels that successfully pass the uniformity test in the VIS0.6, VIS0.8, NIR1.6 and IR10.8 are used to select HRVIS pixels when the corresponding area is scanned. The results of these two configurations have been compared.

The result over land for band VIS0.6 is given in Figure 63), band VIS0.8 in Figure 64), band NIR1.6 in Figure 65) and band HRVIS in Figure 66).

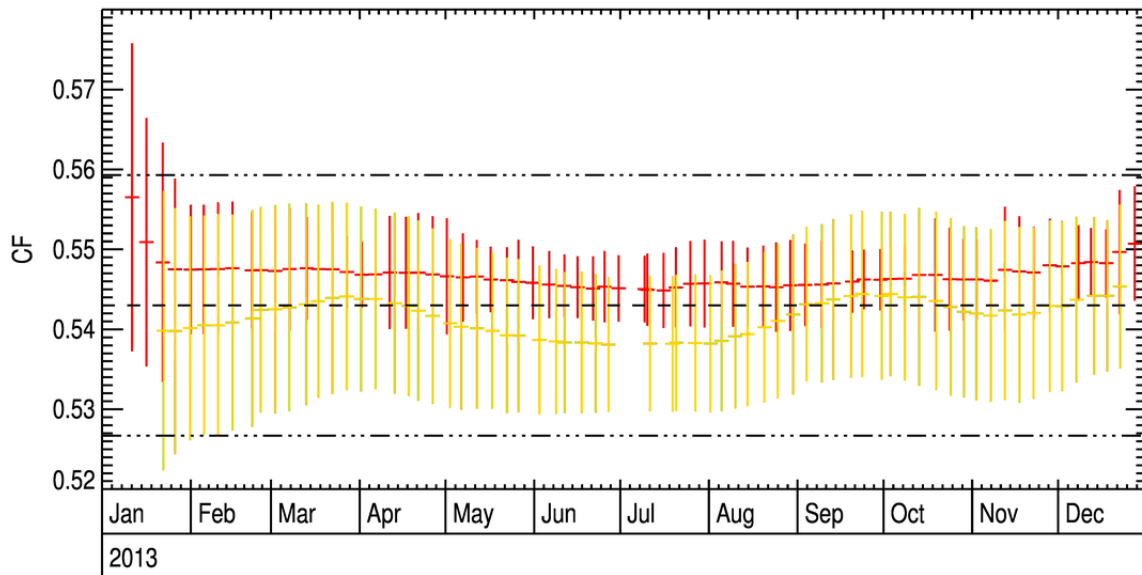


Figure 63 - Times series for the calibration coefficient of Meteosat 10, using land-borne DCCs, in the band VIS0.6, during the year 2013. The red points are the calibration coefficients computed with the mutli-spectral test activated in the VIS0.6, VIS0.8 and NIR1.6, while the yellow points are computed with a spectral filtering activated in all 4 bands (VIS0.6, VIS0.8, NIR1.6 and HRVIS). The black horizontal dashed line is mean calibration coefficient obtained over Libya-4 CEOS PICS. The dotted lines represent the $\pm 3\%$ uncertainties.

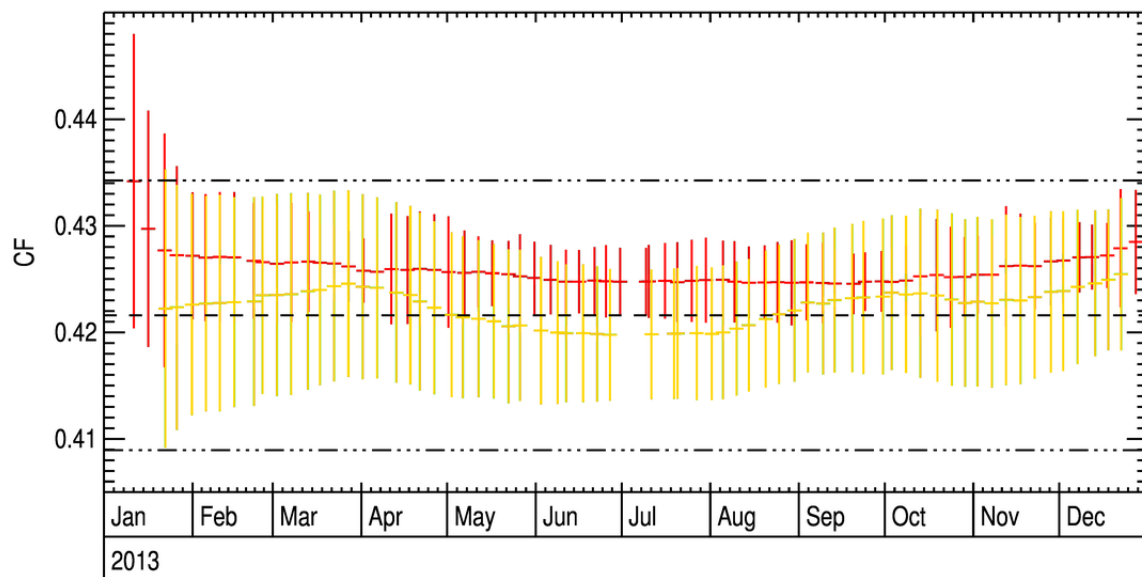


Figure 64 - Same as Figure 63, in the band VIS0.8.

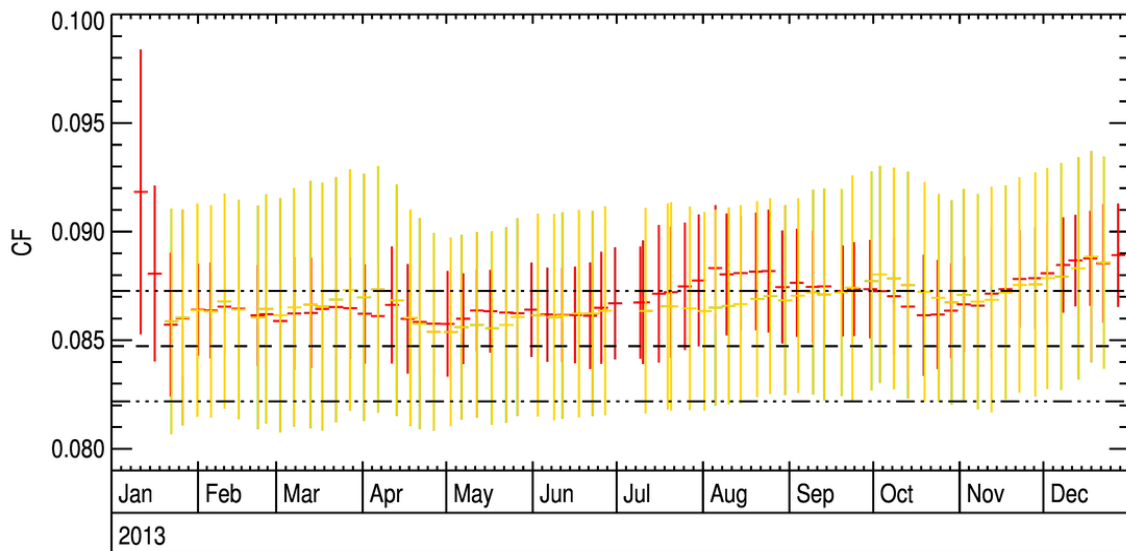


Figure 65 - Same as Figure 63, in the band NIR1.6.

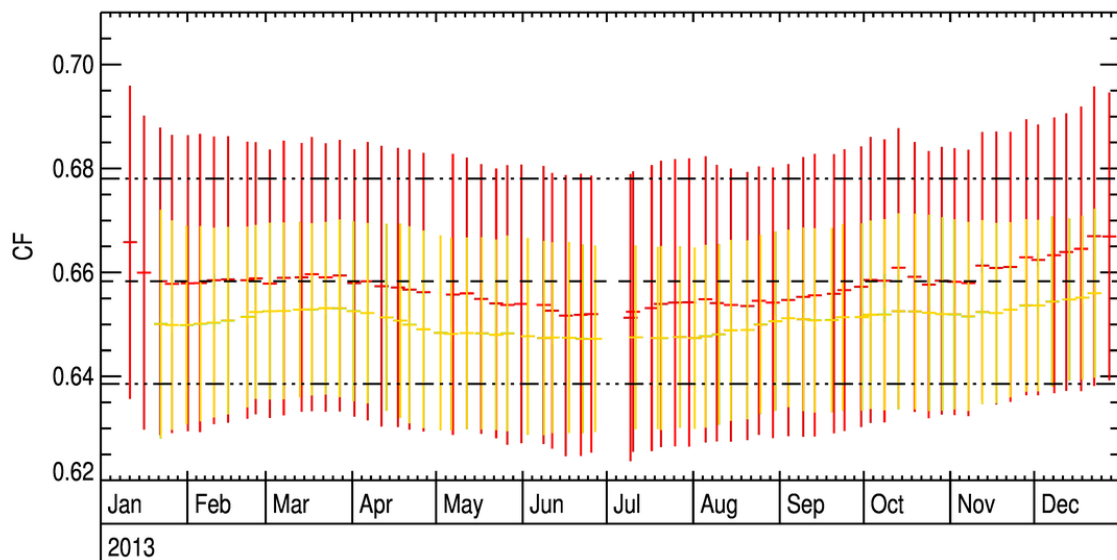


Figure 66 - Same as Figure 63, in the band HRVIS.

The relative difference between the use or not of the HRVIS band in the multi-spectral analysis is summarised in **Error! Reference source not found.**. Over land, this difference is about 1.5% to the exception of the NIR1.6 band. In the VIS0.6 and VIS0.8 bands, the results obtained with the use of the HRVIS band are closer to the calibration results obtained over Libya-4. In any case, these differences are within the uncertainty of the results obtained over Libya-4 and are therefore not significant.

Surface	VIS0.6	VIS0.8	NIR1.6	HRVIS
Land	1.56%	1.32%	0.54%	1.60%
Ocean	1.99%	1.74%	3.73%	1.85%

Table 6-2: Mean relative difference between the calibration coefficient derived with and without the use of the HRVIS band in the multi-spectral filtering.

- On sea

Results over sea are given in Figure 67 for band VIS0.6, Figure 68 for band VIS0.8, Figure 69 for band NIR1.6 and Figure 70 for band HRVIS. On the average, the difference between the two types of filtering is more pronounced over sea than over land (**Error! Reference source not found.**). Such behaviour is due to the limited scanning possibility of the HRVIS band over the Atlantic Ocean in the selected daily time frame. It should also be noted that the use of the HRVIS band in the multi-spectral filtering does not allow the generation of a calibration coefficient all year long. In summer time, when the ITCZ is located in North Atlantic, no pixels are scanned as can be seen in Figure 34. The HRVIS band only scan the Southern part of the Atlantic Ocean that is close to the African continent. A longer time frame, i.e., after 14:00 UTC would be needed to increase the possibility to identify more pixels in the HRVIS band over the Atlantic Ocean.

In the band NIR1.6 (Figure 69), which is sensitive to the effective radius of particles present in the upper layer of the DCC, a sharp increase in the calibration coefficient is detected during summer and autumn. This behaviour is noticeable only when the multi-spectral filtering is also activated in the HRVIS band. Yet this anomaly can be tied to the peculiar retrieving of the HRVIS pixels, that are selected in summer in a more restrained area than the other bands, as seen on Figure 71 and Figure 72. From the coordinates of those selected pixels, it appears that land-borne DCCs can be contaminating the selection process over sea. Their smaller effective radii lead to a brighter TOA BRF, resulting in a higher calibration coefficients.

DCC pixels whose microphysical properties are not perfectly matching the DCC RM are still accumulated, leading to a biased calibration coefficient mean. This is why, when the multi-spectral filtering in the HRVIS band is turned off, not enough good DCC pixels are retained in this band to compute a calibration coefficient, leaving gap in the time series.

Due to the accumulation period mechanism, this effect is propagated over the autumn, after a clear decrease of the calibration coefficient is hit during summer.

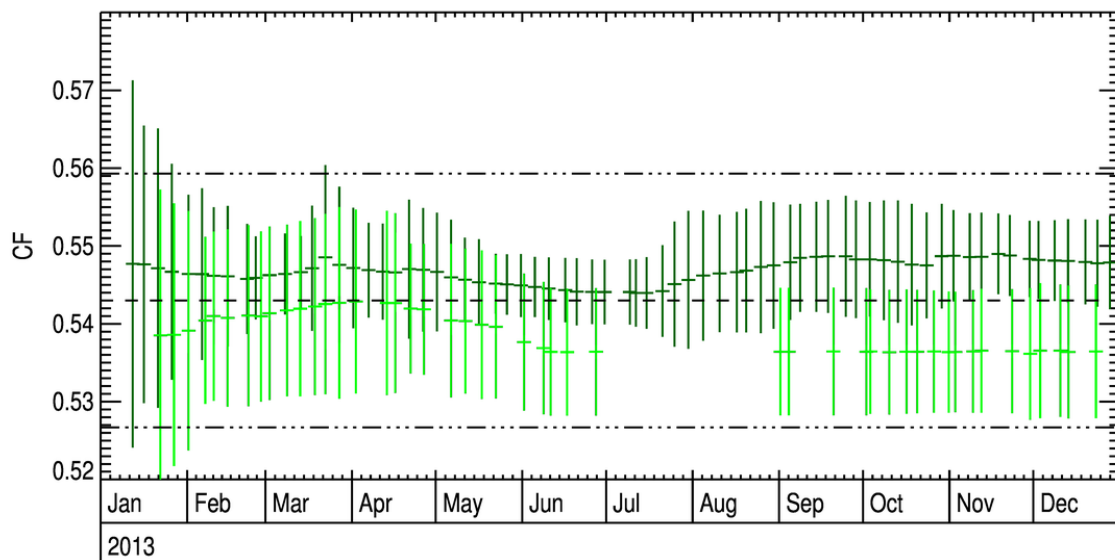


Figure 67 - Times series for the calibration coefficient of Meteosat 10, using sea-borne DCCs, in the band VIS0.6, during the year 2013. The dark green points are the calibration coefficients computed with the multi-spectral test activated in the VIS0.6, VIS0.8 and NIR1.6, while the light green points are computed with a spectral filtering activated in all 4 bands (VIS0.6, VIS0.8, NIR1.6 and HRVIS). The black horizontal dashed line is mean calibration coefficient obtained over Libya-4 CEOS PICS. The dotted lines represent the $\pm 3\%$ uncertainties.

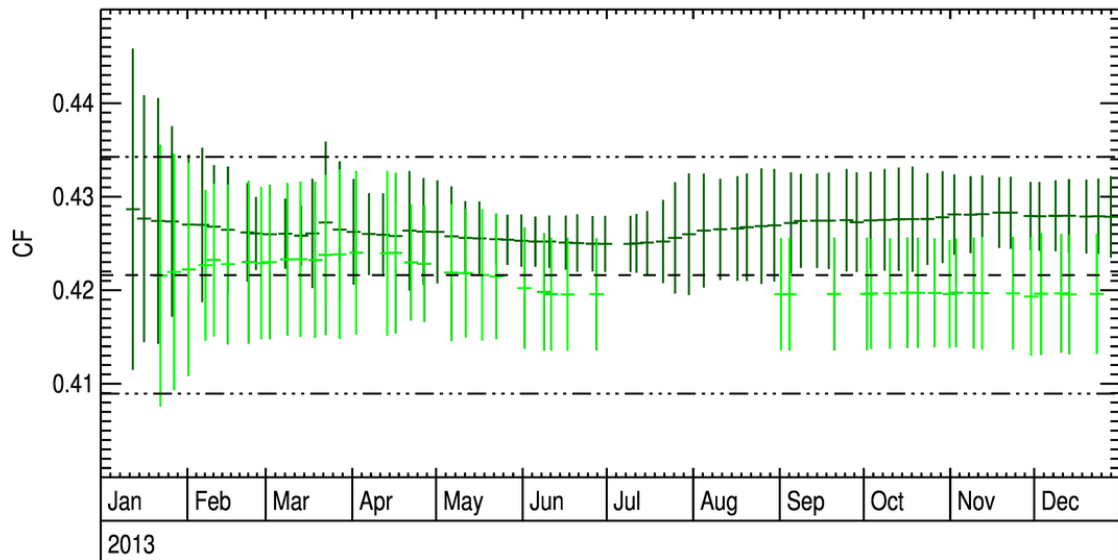


Figure 68 - Same as Figure 67, in the band VIS0.8.

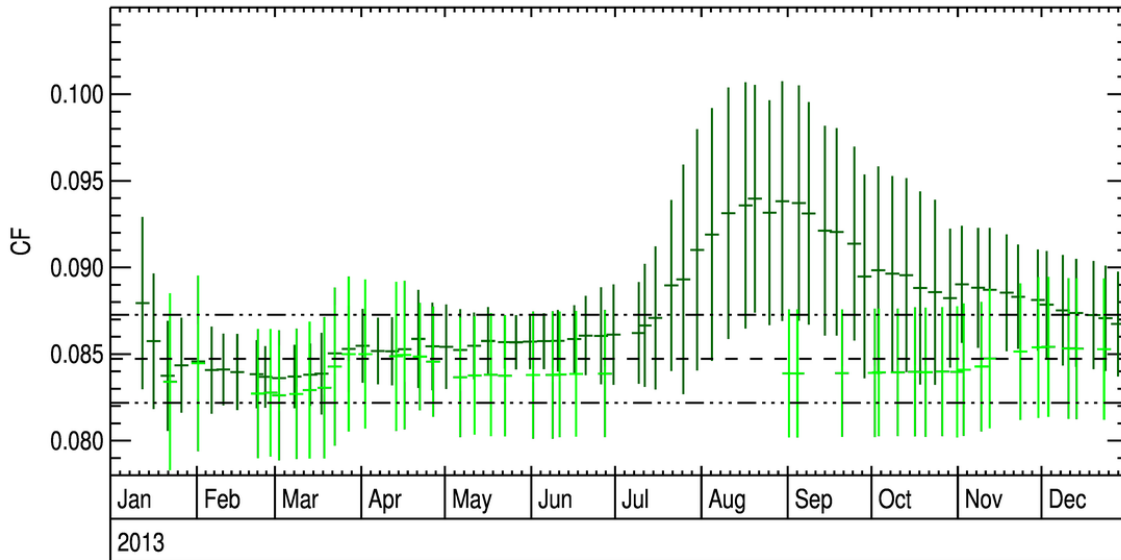


Figure 69 - Same as Figure 67, in the band NIR1.6.

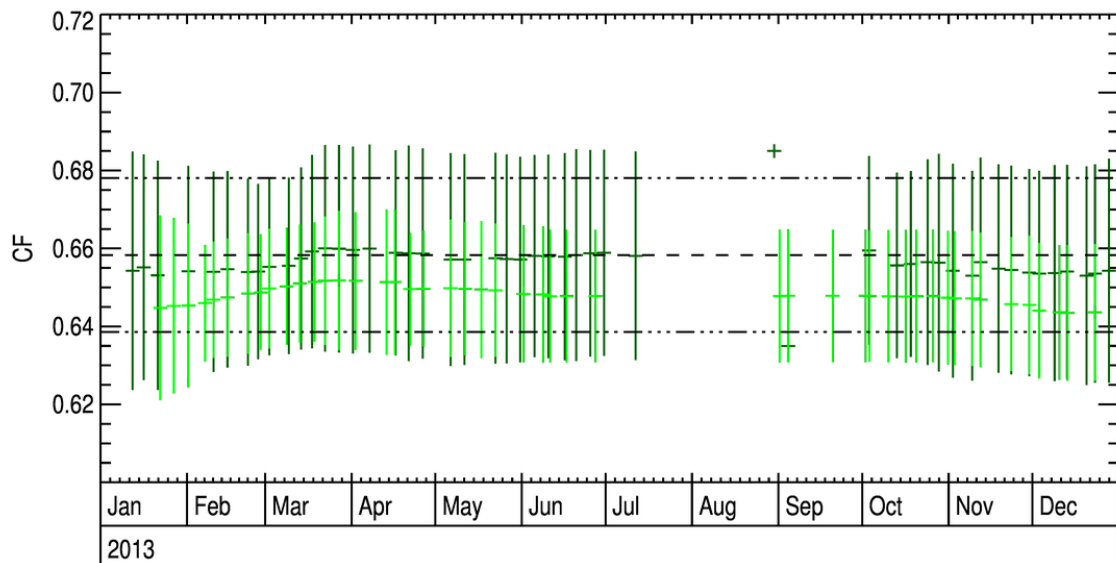


Figure 70 - Same as Figure 67, in the band HRVIS.

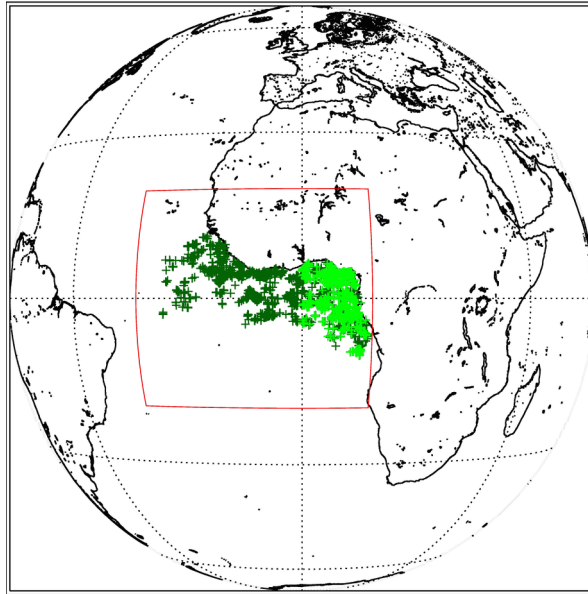


Figure 71 - Positions of the selected pixels during winter. Dark green pixels are acquired without filtering in the HRVIS band, while light green pixels are selected with the 4-bands filtering.

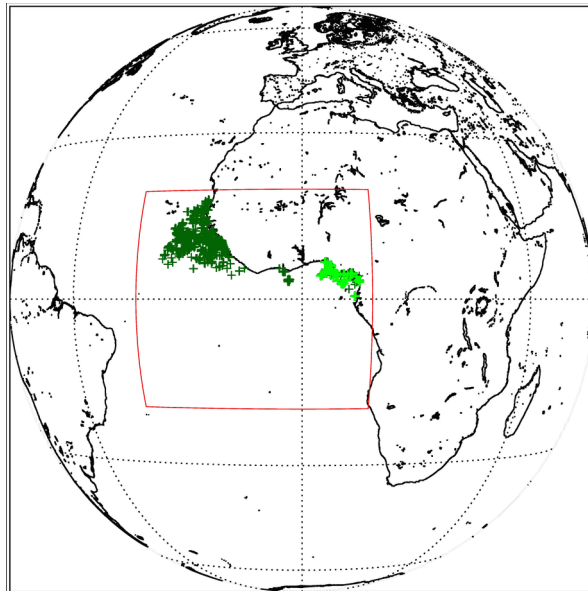


Figure 72 - Positions of the selected pixels during summer. Dark green pixels are acquired without filtering in the HRVIS band, while light green pixels are selected with the 4-bands filtering.

6.2. TIME SERIES

6.2.1. Meteosat-7 data (IODC/ZDS)

6.2.1.1. ZDS (2005)

The proposed method has been applied on Meteosat-7 data using the original pre-launch sensor spectral response. No correction has been applied for the spectral aging of the sensor spectral response. Results are given in Figure 73. There is no difference in the calibration coefficient obtained over land and sea. The results show also no significant seasonal effects in the results. These results have not been compared by those obtained over Libya-4 due to the uncertainty on the actual value of the sensor spectral response.

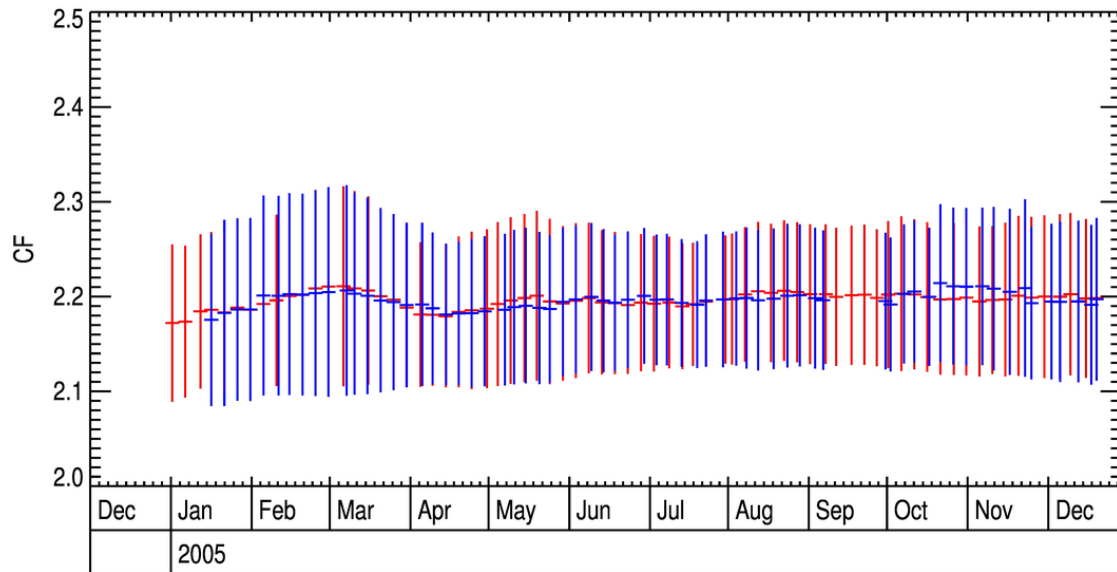


Figure 73: Calibration coefficient in $Wm^{-2}sr^{-1}\mu m^{-1}/DC$ for Meteosat-7 VIS band derived in 2005 over land (red) and ocean (blue).

6.2.1.2. IODC (2007)

Results for 2007 when Meteosat-7 was over the Indian Ocean are shown in Figure 74. There is a small difference in the calibration coefficient derived over land and sea in the second half of the year, i.e., after June. The reason of this difference, which does not exceed 1%, is not clear. The estimated uncertainty derived over sea is larger than over land and this difference is therefore not significant. The analysis of the location of the identified DCC during the first and second half of the year do not reveal particular feature (Figure 75). It should be noted that most of the DCC pixels are identified in the South-East part of the search area.

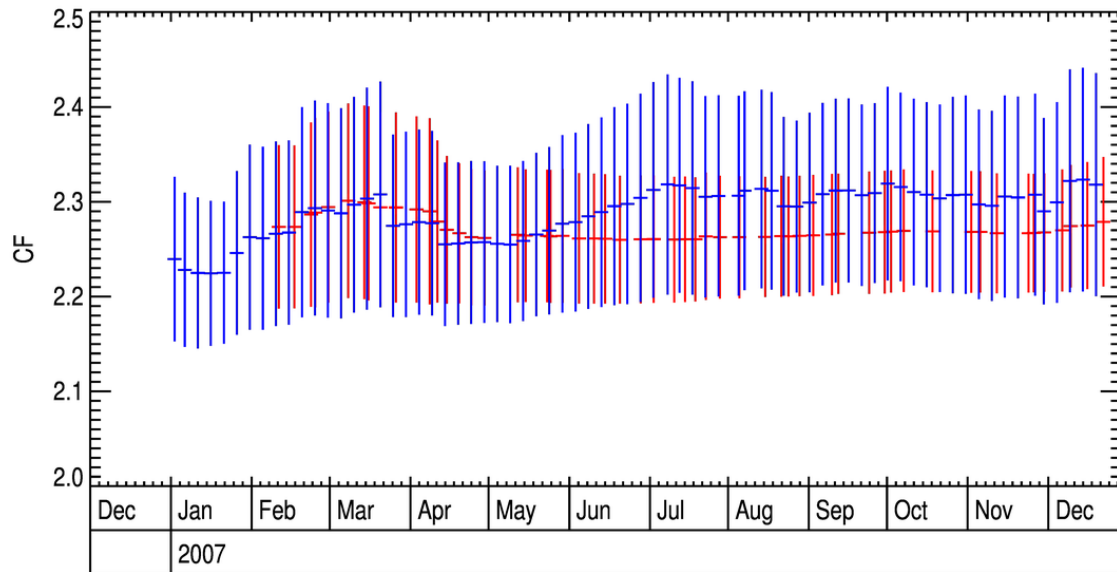


Figure 74: Same as Figure 73 but for year 2007.

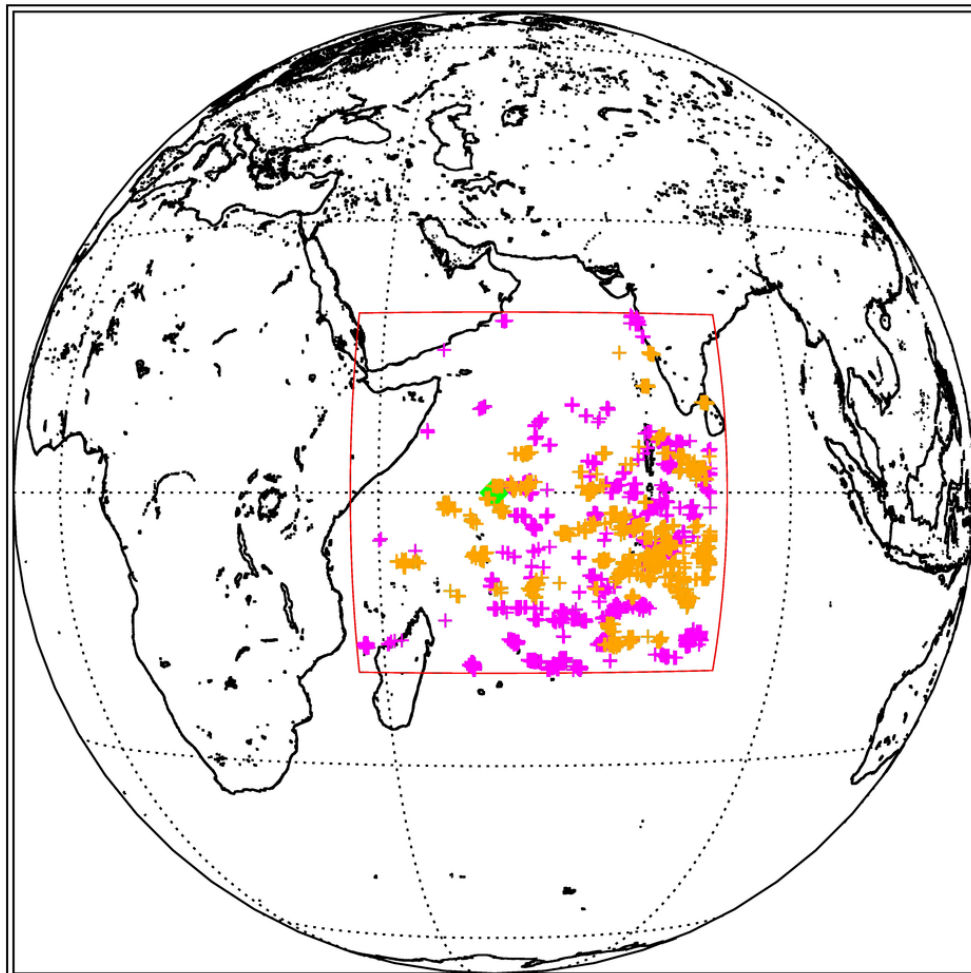


Figure 75: Localization of the identified DCC pixels in January – June 2007 (magenta) and July – December 2007 (orange). The search area is indicated in red and the sub-satellite point in green.

6.2.2. Meteosat-8 data (IODC/ZDS)

6.2.2.1. ZDS (2005)

Meteosat-8 data acquired in 2005 have been processed in order to compare any possible differences in the seasonality of the results with respect to those obtained for Meteosat-7. Results over land and sea are shown in Figure 76 to Figure 79. These results have been obtained using the standard RM parameter and identification criteria, i.e., the HRVIS band is not used for the multi-spectral DCC pixel filtering. As can be seen in Figure 76, it takes about 6 months before reaching a convergence between the calibration coefficient obtained over land and sea. There are no clear seasonal patterns in the results to the exception of the NIR1.6 band. Results obtained in the HRVIS band (Figure 79) are very consistent with those obtained in the Meteosat-7 VIS band (Figure 73). In the solar channels, calibration coefficients derived over DCC slightly underestimate those derived over Libya-4, though this difference is not significant.

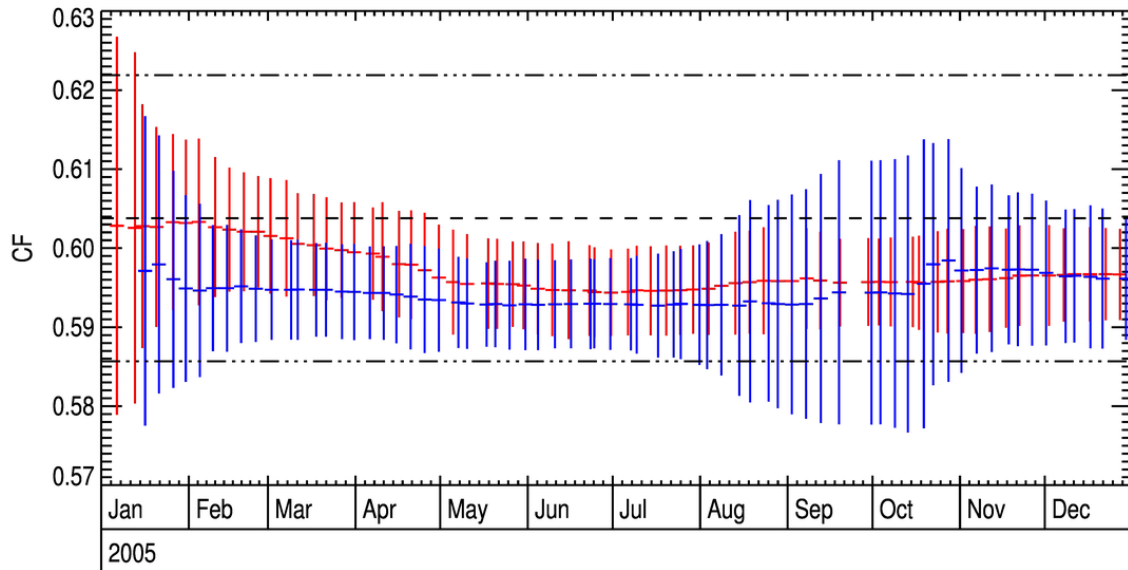


Figure 76: Calibration coefficient in $Wm^{-2}sr^{-1}\mu m^{-1}/DC$ for Meteosat-8 VIS0.6 band derived in 2005 over land (red) and ocean (blue). The black horizontal dashed line is mean calibration coefficient obtained over Libya-4 CEOS PICS. The dotted lines represent the $\pm 3\%$ uncertainties.

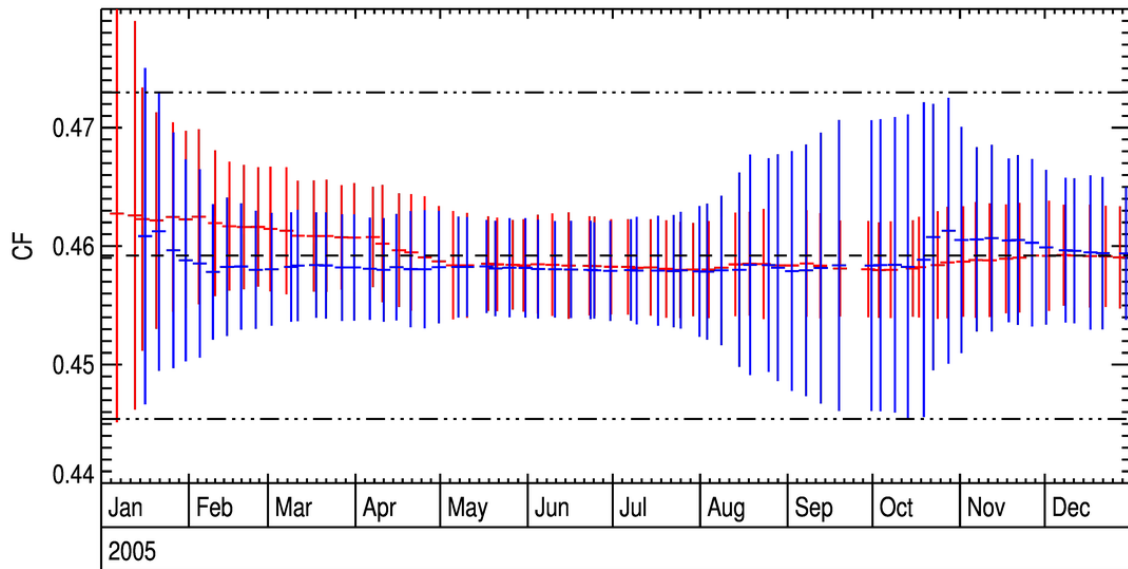


Figure 77: Calibration coefficient in $Wm^{-2}sr^{-1}\mu m^{-1}/DC$ for Meteosat-8 VIS0.8 band derived in 2005 over land (red) and ocean (blue). The black horizontal dashed line is mean calibration coefficient obtained over Libya-4 CEOS PICS. The dotted lines represent the $\pm 3\%$ uncertainties.

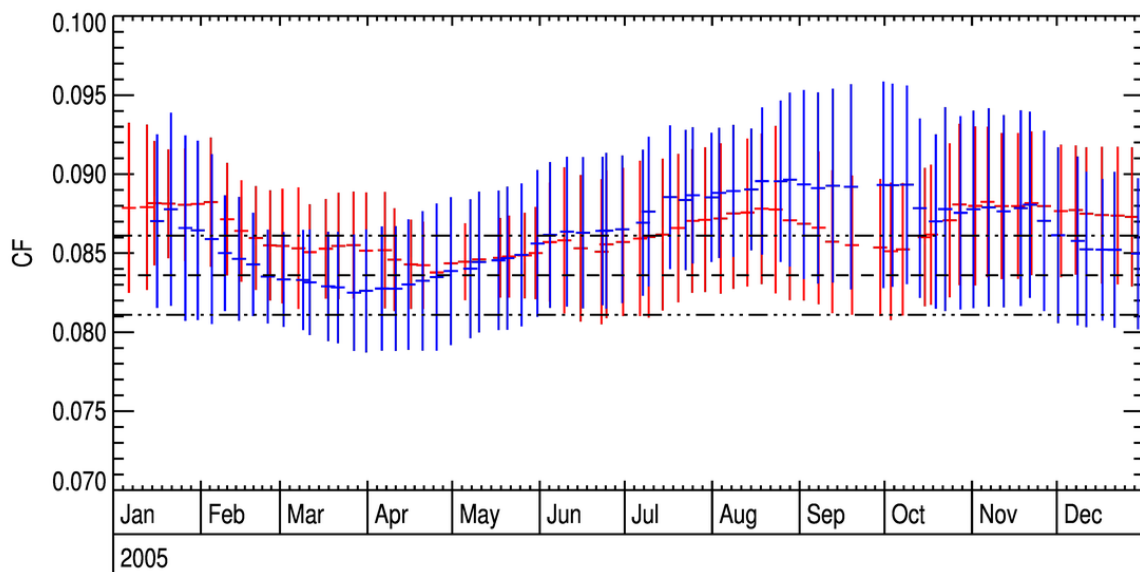


Figure 78: Calibration coefficient in $Wm^{-2}sr^{-1}\mu m^{-1}/DC$ for Meteosat-8 NIR1.6 band derived in 2005 over land (red) and ocean (blue). The black horizontal dashed line is mean calibration coefficient obtained over Libya-4 CEOS PICS. The dotted lines represent the $\pm 3\%$ uncertainties.

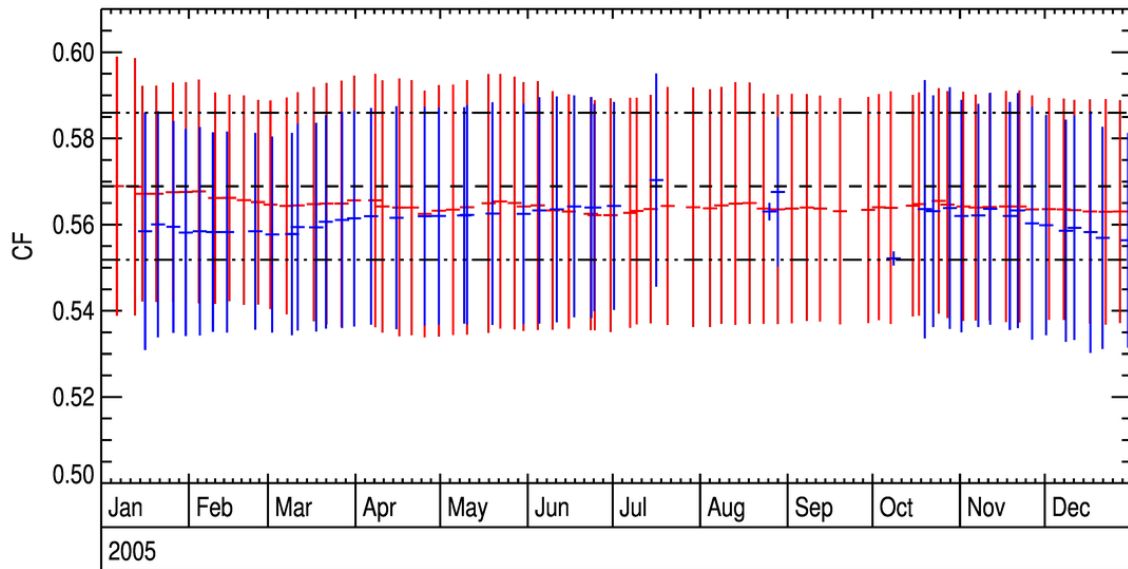


Figure 79: Calibration coefficient in $Wm^{-2}sr^{-1}\mu m^{-1}/DC$ for Meteosat-8 HRVIS band derived in 2005 over land (red) and ocean (blue). The black horizontal dashed line is mean calibration coefficient obtained over Libya-4 CEOS PICS. The dotted lines represent the $\pm 3\%$ uncertainties.

6.2.2.2. IODC (2016 - 2017)

Seven months of MSG1 data acquired over the over Indian Ocean between September 2016 and March 2017 have been processed applying the standard identification parameters and RM values. Results for band VIS0.6 are given in Figure 80. Calibration coefficients derived over land DCC converge more rapidly to stable values than over the ZDS (Figure 76). It has not been possible to identify DCC pixels over before mid-November. It is recommended to increase the time of day when slots are processed. The estimated uncertainty over sea is taking very large value at the beginning of the processing period and reaches values similar to the one derived over land after two months. Calibration coefficients derived over land and sea agree with 0.1%, indicating that the COT over these two surface types is identical. Similar conclusions hold for the VIS0.8 band (Figure 81) with a slightly higher discrepancy of 0.34% between mean calibration coefficient derived over sea and land. Results in the NIR1.6 band (Figure 83) show important temporal variations over sea, which indicate possible temporal variations of the cloud ice crystal radius. Additional analysis would be needed to confirm these results, processing a longer period. In the HRVIS band (Figure 84), there is a very good agreement between the coefficient derived over land and sea.

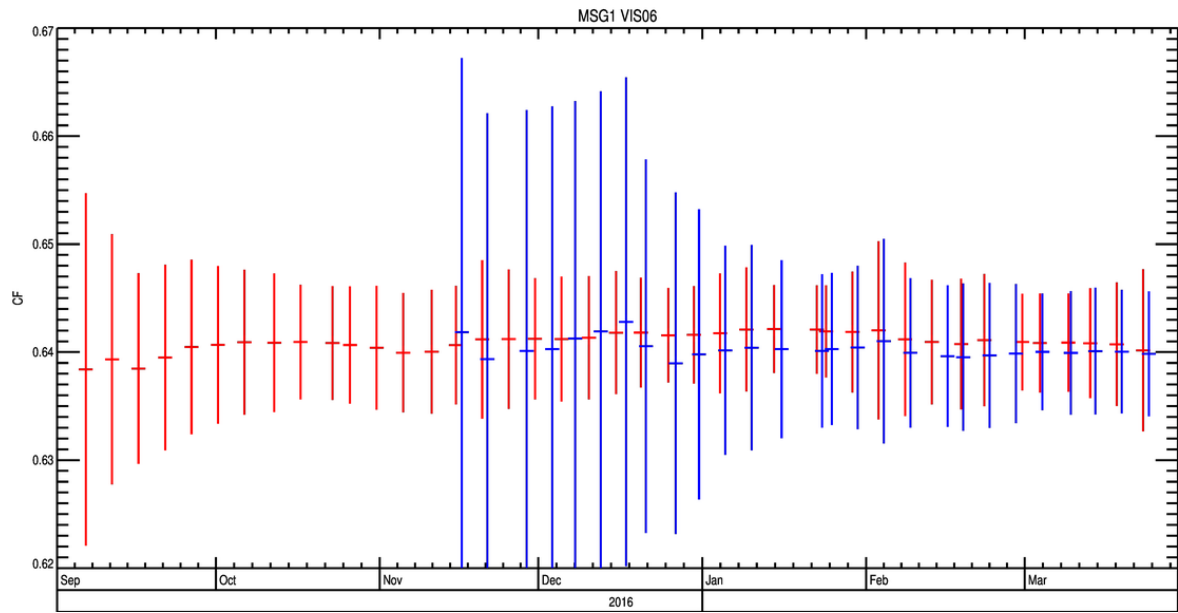


Figure 80: Calibration coefficient in $Wm^{-2}sr^{-1}\mu m^{-1}/DC$ for IODC Meteosat-8 VIS0.6 band derived during the Sept. 2016 – March 2017 period over land (red) and ocean (blue).

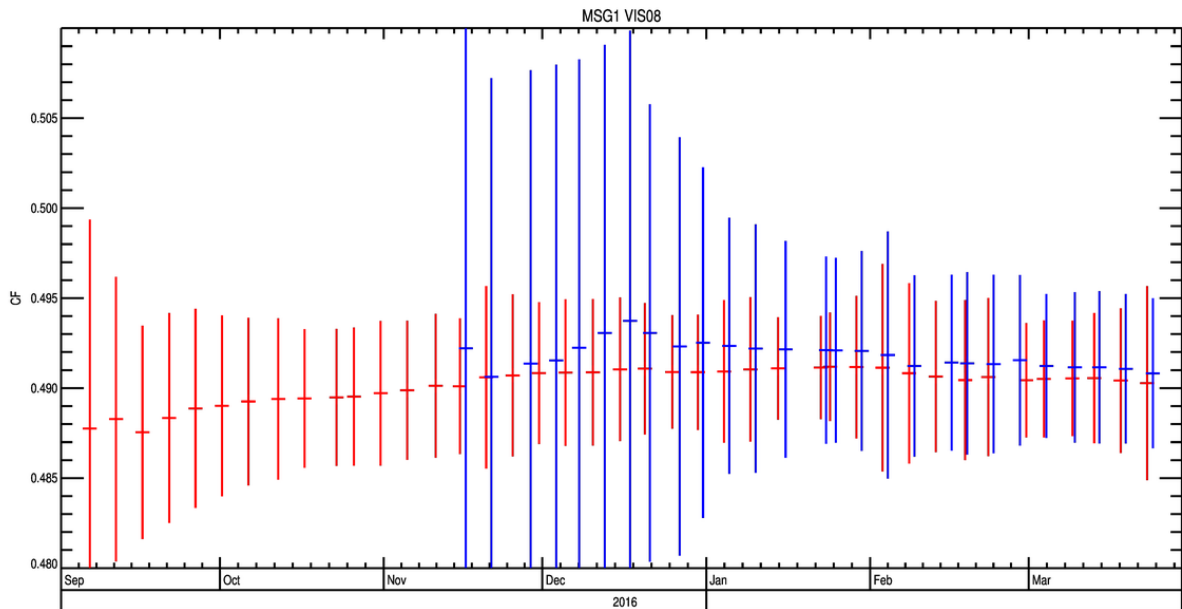


Figure 81: Calibration coefficient in $Wm^{-2}sr^{-1}\mu m^{-1}/DC$ for IODC Meteosat-8 VIS0.8 band derived during the Sept. 2016 – March 2017 period over land (red) and ocean (blue).

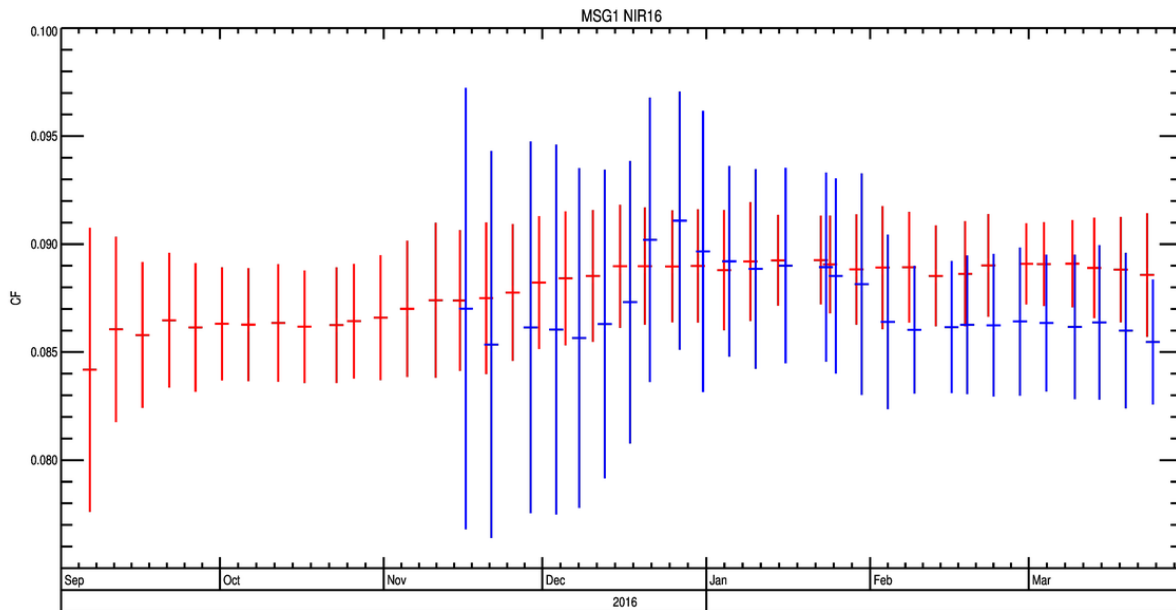


Figure 82: Calibration coefficient in $Wm^{-2}sr^{-1}\mu m^{-1}/DC$ for IODC Meteosat-8 NIR1.6 band derived during the Sept. 2016 – March 2017 period over land (red) and ocean (blue).

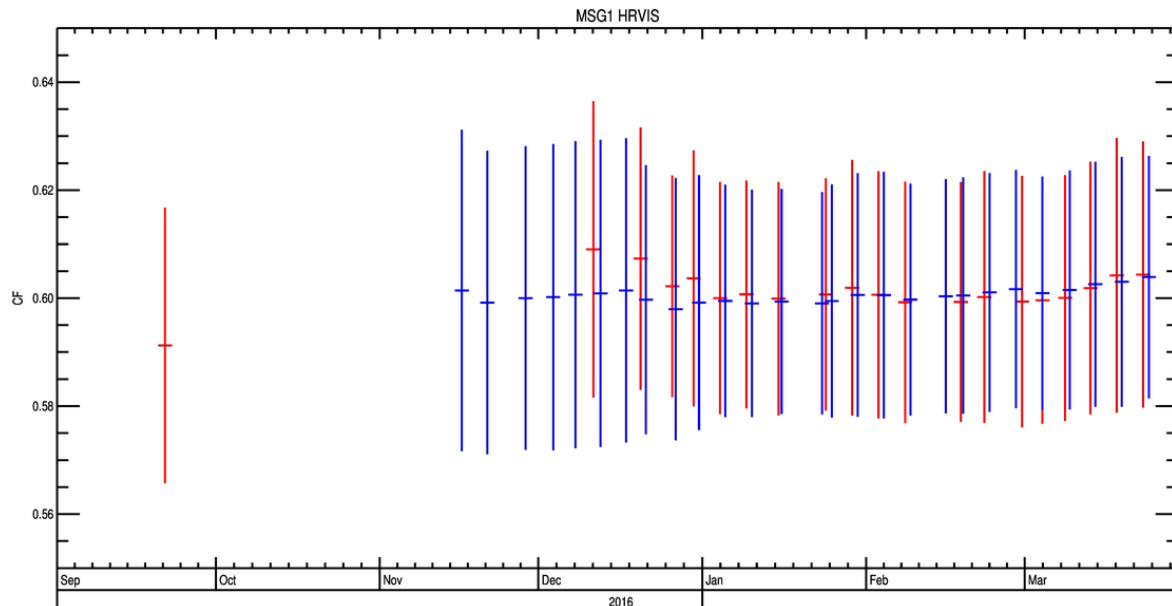


Figure 83: Calibration coefficient in $Wm^{-2}sr^{-1}\mu m^{-1}/DC$ for IODC Meteosat-8 HRVIS band derived during the Sept. 2016 – March 2017 period over land (red) and ocean (blue).

6.2.3. Meteosat-10 data (ZDS – Land and Sea)

The times series for the calibration coefficient of Meteosat-10, are created for the period ranging from 2013 to 2015. One series is made using calibration coefficients over land (in red) while the other uses sea-borne DCC pixels. Results are given in Figure 84 to Figure 87. The temporal drift is in very good agreement with the one obtained over Libya-4. The solar channels now slightly overestimate the calibration coefficients derived over Libya-4 but this difference is not significant. It illustrates the uncertainty associated with these calibration targets. There is also a very good agreement between the DCC calibration coefficients derived over land and sea. On the average, the difference obtained over these two surface types does not exceed 0.20%. The seasonal patterns in the NIR1.6 band, the intensity of which changes from year to year, has been discussed in Section (6.1).

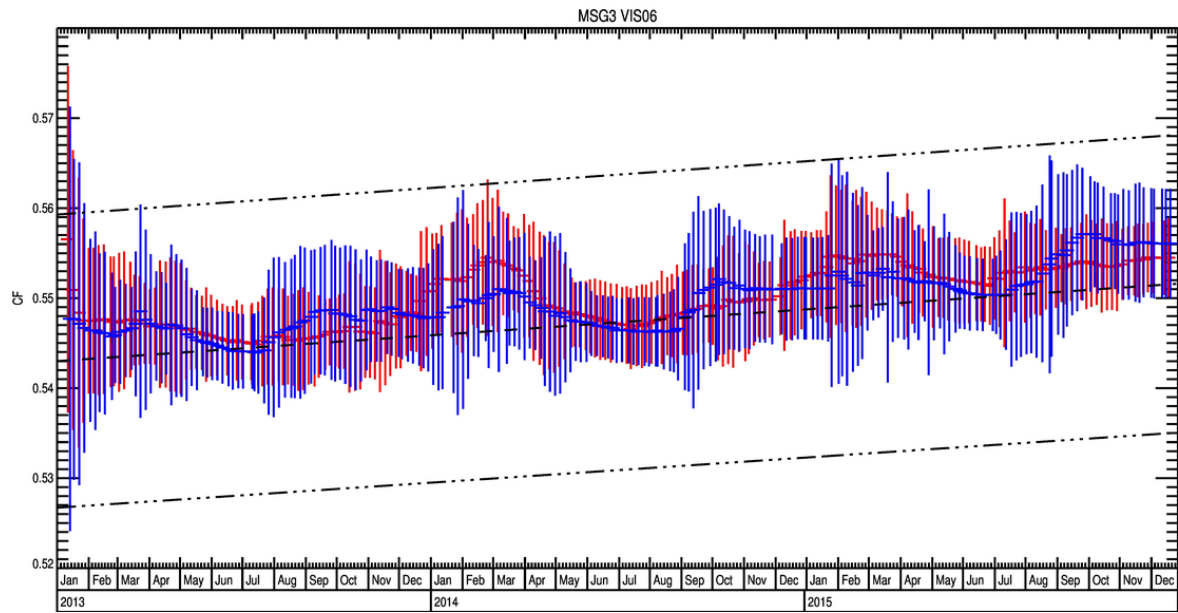


Figure 84 - Calibration coefficient in $Wm^{-2}sr^{-1}\mu m^{-1}/DC$ for Meteosat-10 VIS0.6 band derived in 2013-2015 over land (red) and ocean (blue). The black dashed line gives the value of the mean calibration coefficient obtained over Libya-4 CEOS PICS. The dotted lines represent the $\pm 3\%$ uncertainties.

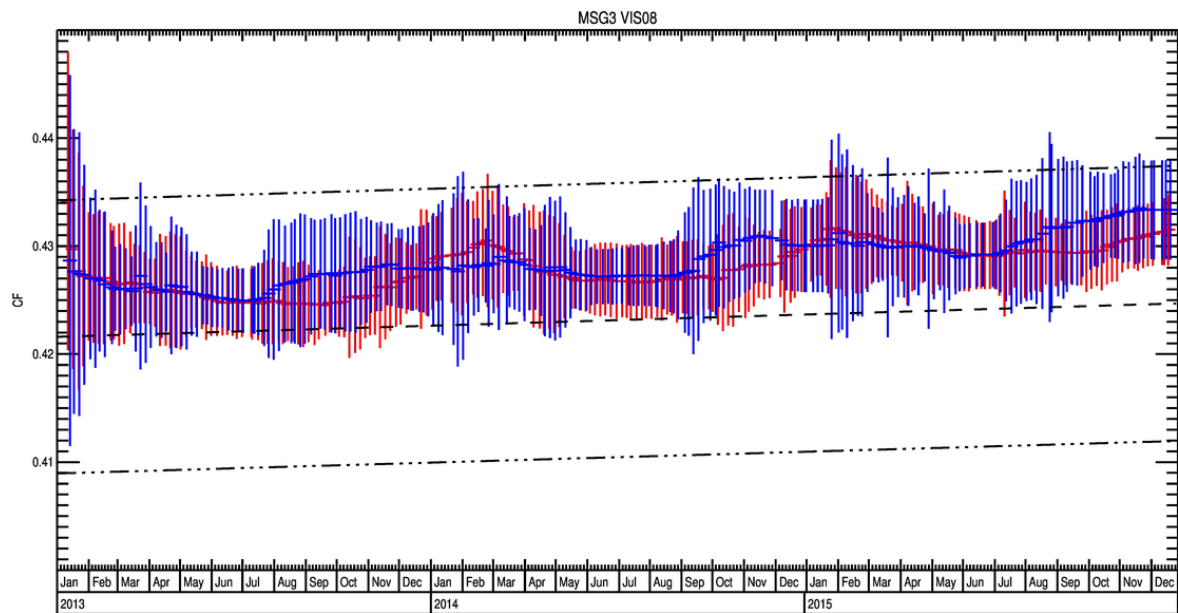


Figure 85 – Same as Figure 84, for the VIS0.8 band.

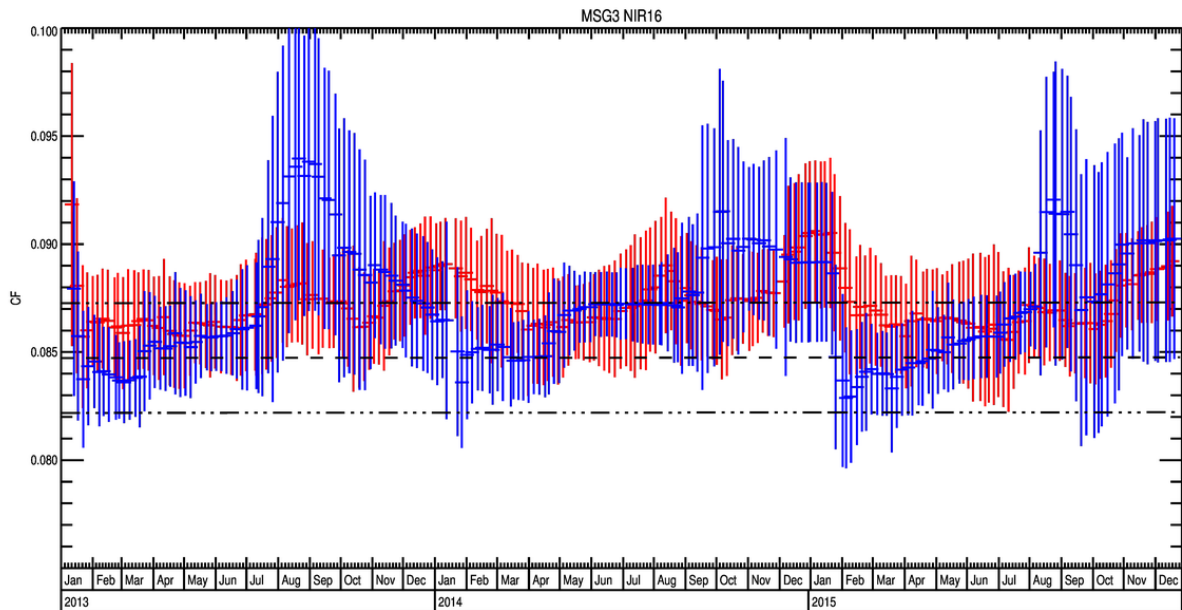


Figure 86 - Same as Figure 84, in the NIR1.6 band.

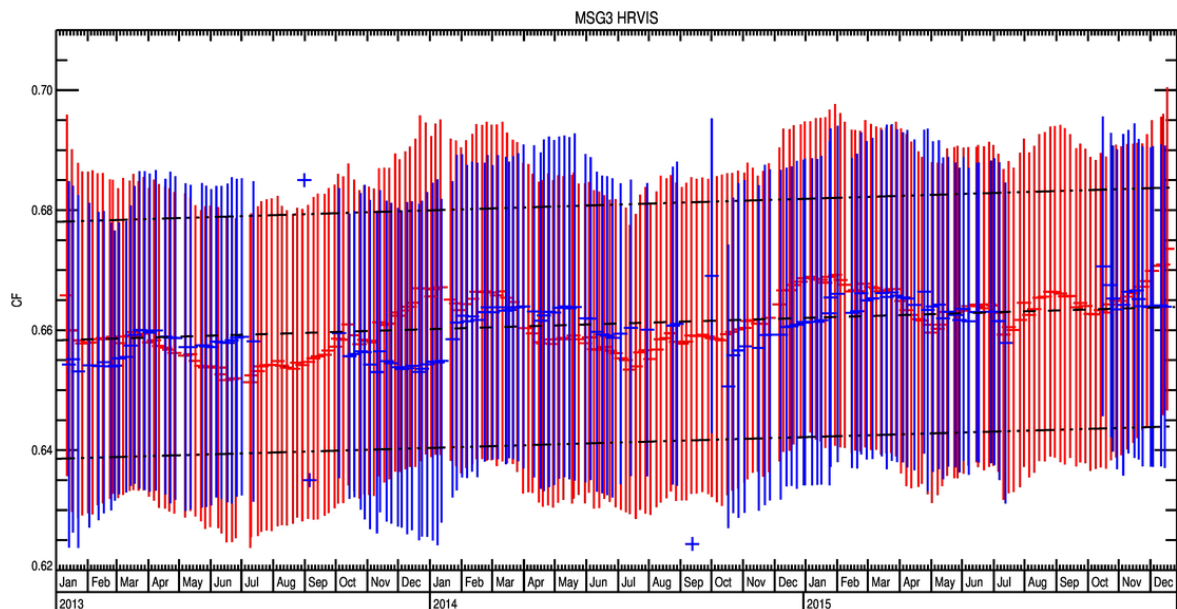


Figure 87 - Same as Figure 68, in the HRVIS band.

The values of the calibration coefficient degradation derived in Figure 84 to Figure 87 have been summarized in Table 6-3. Calibration drift derived over DCC is higher than over desert. This might be due to some non-linearity effects of the sensor response that increase with time.

Target	DCC land	DCC sea	Libya-4
	VIS0.6		
Daily degradation (1)	0.873	0.930	0.786
Daily degradation uncertainty (1)	0.222	0.271	3.214
Yearly relative degradation (%)	0.585	0.624	0.528
	VIS0.8		
Daily degradation (1)	0.560	0.638	0.283

Daily degradation uncertainty (1)	0.161	0.196	2.024
Yearly relative degradation	0.481	0.549	0.245
NIR1.6			
Daily degradation (1)	0.059	0.116	0.003
Daily degradation uncertainty (1)	0.108	0.118	0.031
Yearly relative degradation (%)	0.248	0.497	0.011
HRVIS			
Daily degradation (1)	0.959	0.891	0.510
Daily degradation uncertainty (1)	1.178	1.408	3.451
Yearly relative degradation (%)	0.534	0.496	0.283

Table 6-3: Met-10 degradation rate derived during the 2013-2015 era over DCC-land, DCC-sea and Libya4. (1) Daily degradation is given in $Wm^{-2}sr^{-1}\mu m^{-1}/DC (10^{-5}) / day$

6.3. COMPARISON WITH OTHER SSCC TARGETS

6.3.1. Overview

The objective of this is to compare DCC results with those derived over sea and bright desert (Libya-4) targets for Meteosat-10 (MSG-3). Pixel identification over these two target types has been taken from SSCC version 4.10. Simulated radiances have been however performed differently. Over sea, the same input parameters have been used, .i.e, atmospheric and sea surface properties but with the LibRadtran V2 model instead of 6S. LibRadtran gaseous transmittance is based on HITRAN 2012 as oppose to HITRAN96 for 6S and includes therefore additional molecules. In addition, Libradtran implement a better numerical scheme for the coupling between scattering and gaseous transmittance. For TOA simulation over Libya-4, the RTMOM model has been used with surface and atmospheric properties described in Govaerts et al. (2013) instead of Govaerts et al. (2004).

6.3.2. Accuracy of the Libya-4 TOA radiance simulations

In order to compare DCC calibration results with those derived over Libya-4, it is important to assess in an independent way the accuracy of these simulations over bright deserts. Many observations have been acquired over that site by very accurately calibrated radiometers such as AQUA/MODIS and Envisat/MERIS. Hence, data acquired by these instruments over Libya-4 have been simulated, paying a special attention to the difference between observation and simulation according to the viewing and illumination geometries.

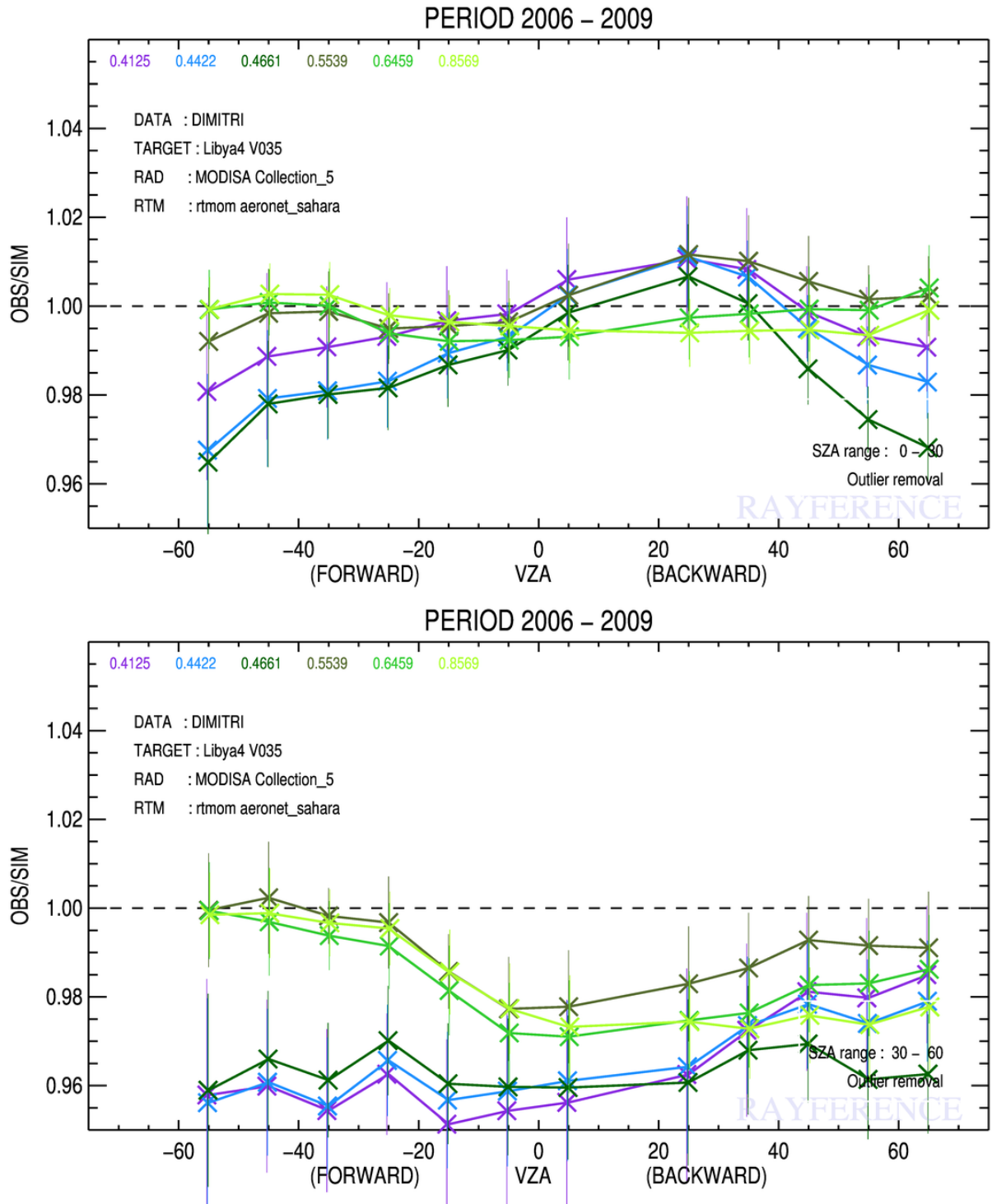


Figure 88: Mean ratio between ACQUA/MODIS observations acquired over Libya4 between 2006 and 2009 and simulations as a function of the viewing directions. Top panel: sun zenith angles in the 0 – 30° interval. Bottom panel : sun zenith angles in the 30 – 60° interval.

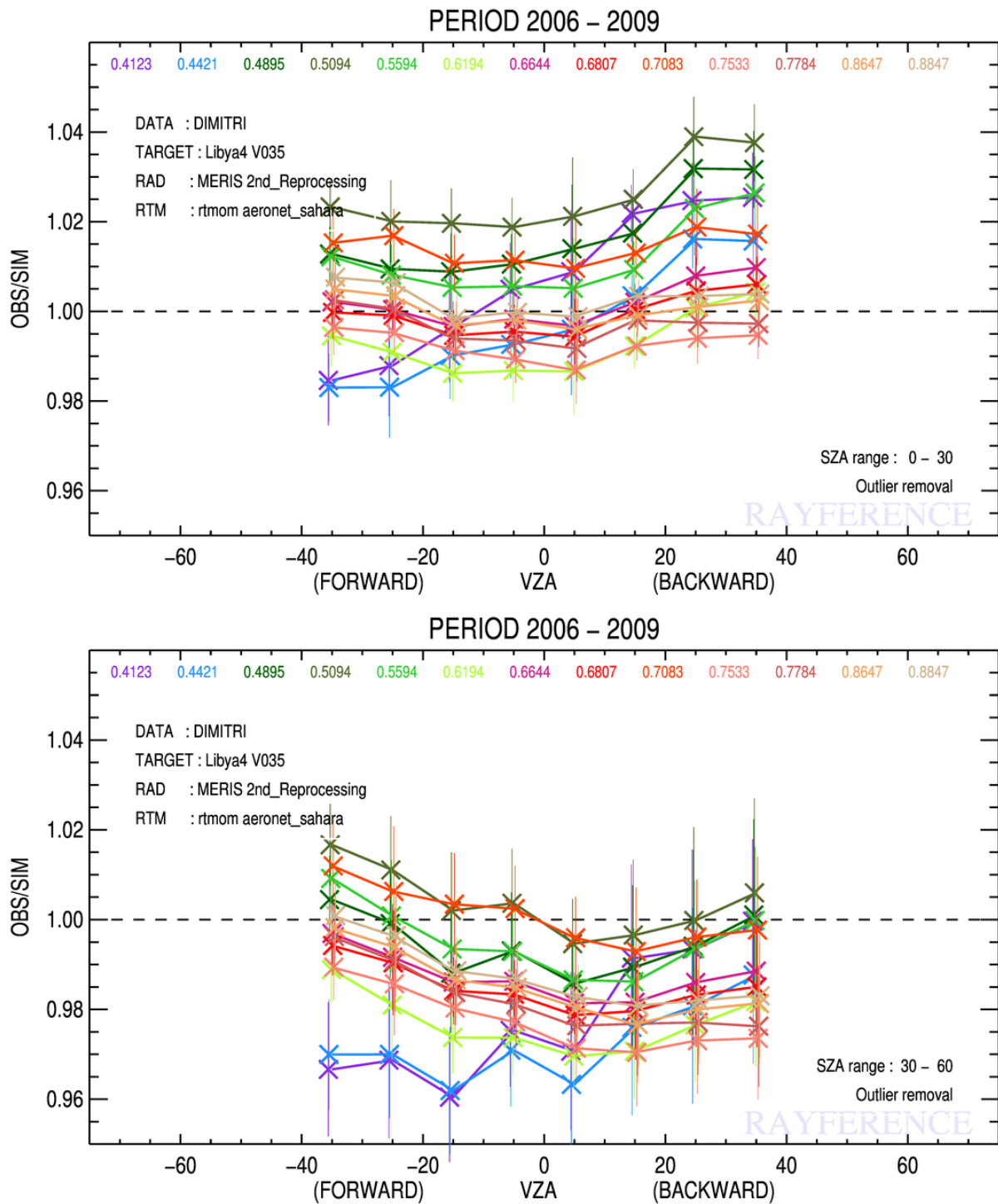


Figure 89: Same as Figure 88 but for MERIS observations.

Acqua/MODIS and MERIS time series over Libya-4 have been taken from ESA DIMITRI calibration tool for the 2006-2009 period. It represents several hundredths of observations. Each observation has been simulated using the same atmospheric and surface description as for SEVIRI simulations. The ratio between observations and simulations have been analysed as a function of the viewing angles discriminating sun zenith angle (SZA) smaller and larger than 30°. Results are shown on Figure 88 for MODIS and on Figure 89 for MERIS.

On the average, simulation matches observations within $\pm 2\%$ for spectral bands located in the $0.6 - 0.8 \mu\text{m}$ spectral interval where the bulk of the radiation contributes to the signal in the [HR]VIS band. Additionally, there are no clear trends as a function of the viewing angles. BRDF effects are therefore well represented.

A closer look at the results shows that discrepancies between observations and simulations increase as the wavelength decreases and SZA increases. In the blue spectral region, discrepancies might exceed 2%, in particular when SZA exceeds 30° and viewing angles 40° . It is therefore recommended to restrict viewing and illumination zenith angles to 40° to contain averages discrepancies between observations and simulations under $\pm 2\%$.

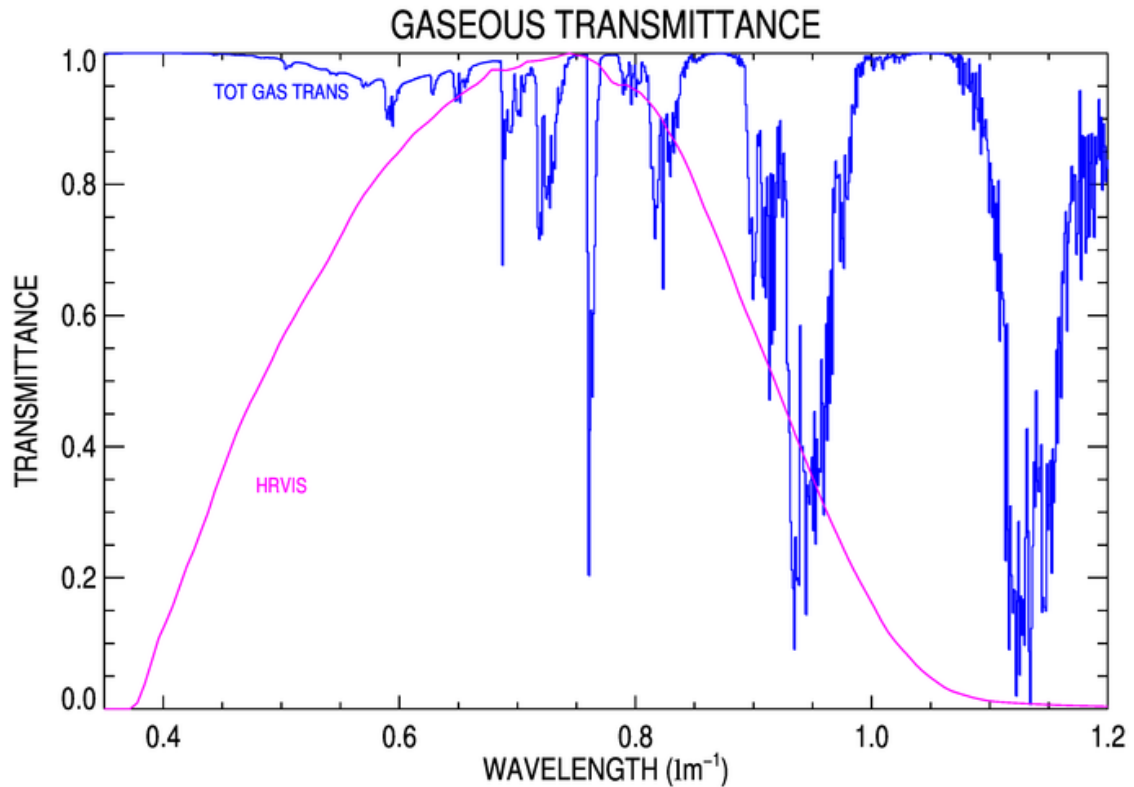
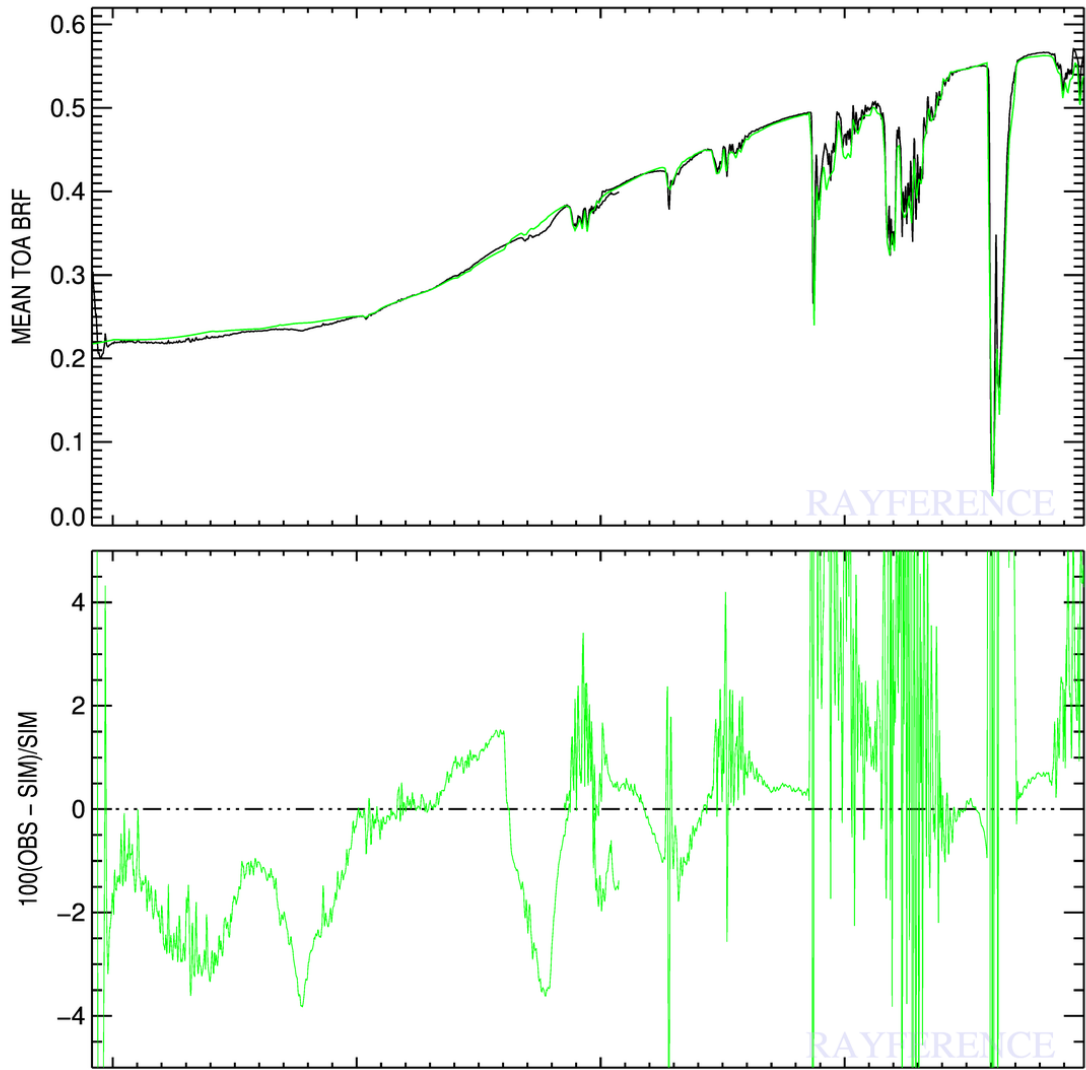


Figure 90 - Total gaseous transmittance within the $0.4 - 1.1 \mu\text{m}$ spectral region.

The conclusion of these comparisons do not directly apply to the HRVIS band. Most of MODIS and MERIS bands located within the MVIRI/VIS band interval $0.4 - 1.1 \mu\text{m}$ fall within so-called “window” regions, i.e., where the molecular absorption is very low. This region is affected by some severe absorption essentially due to water vapour and oxygen (Figure 90). Hence, to evaluate TOA simulation over absorption regions, GOME observations have also been simulated.



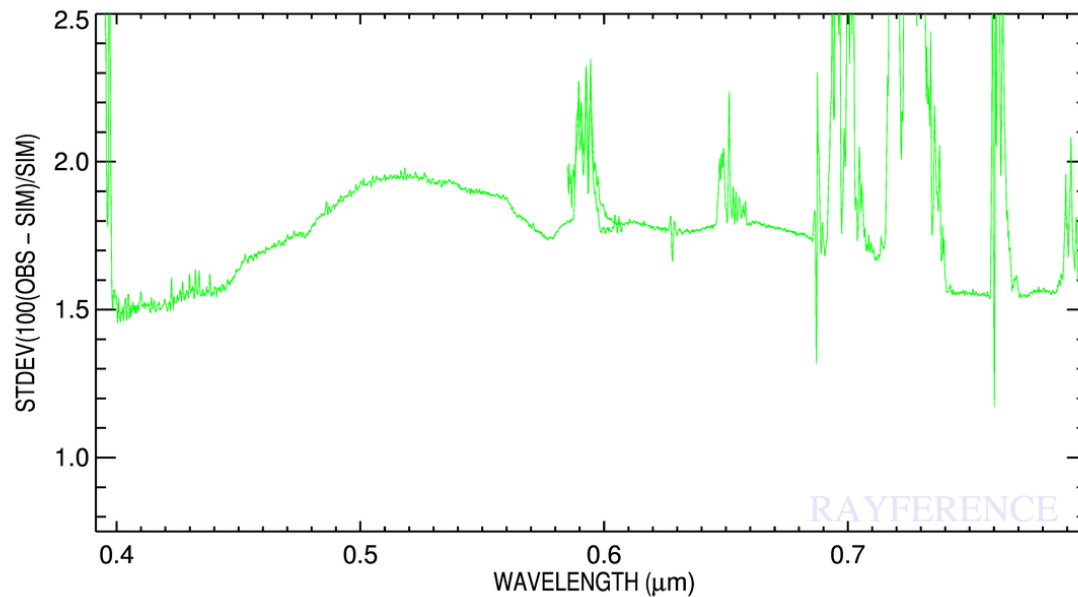


Figure 91: Comparisons with GOME 2b band -3 and -4 (black) and simulation (green). Top panel: TOA BRF. Medium Panel: relative bias between observations and simulations in per cent. Bottom panel: Standard deviation of the relative bias in percent.

The spectral behavior of the simulated TOA radiance within the HRVIS band has been analysed against GOME-2b (Global Ozone Monitoring Experiment-2) observations provided by EUMETSAT. The Libya-4 site corresponds to one GOME pixel that has a resolution of about $80\text{km} \times 20\text{km}$. More than 100 cloud-free observations have been acquired during the selected period. To minimize the surface anisotropic effects resulting from the sand dunes, only data acquired with a viewing and sun azimuth angles smaller than 40° have been kept.

The GOME-2 is an optical spectrometer, fed by a scan mirror which enables across-track scanning in nadir, as well as sideways viewing for polar coverage and instrument characterisation measurements using the moon. GOME-2 senses the Earth's backscattered radiance and extra-terrestrial solar irradiance in the ultraviolet and visible part of the spectrum (240 nm – 790 nm) at a high spectral resolution between 0.26 nm – 0.51 nm. There are 4096 spectral points from 4 detector channels transferred for each individual GOME-2 measurement. On MetOp-B, on which GOME-2 observations used in this study is flying, the footprint size is 80×40 (Metop-B). Only GOME-2B band-3 (401-600nm) and -4 (590 – 790nm) have been used in this study.

Results are presented in Figure 91. For each GOME band, the following statistics have been computed:

- The mean observed and simulated data (top panel);
- The mean relative bias between observations and simulations (medium panel);
- The standard deviation of the relative difference between observations and simulations (bottom panel).

A first look at the results show a good agreement between simulations and observations to the exception of spectral regions dominated with high molecular absorption. In the 350 – 500nm spectral region, simulated TOA BRF are slightly overestimated due to an underestimation of NO_2 absorption contribution. Close to the 465nm, 565nm and 650nm spectral region, simulated TOA BRF overestimates GOME observations by several percent resulting from the absence of the O_4 molecule in the estimation of the gaseous transmittance. Around 560nm, there is a sharp transition in the mean bias from about +2% to -3%. A detail of the molecular transmittance in that spectral region is shown on Figure 92.

The relative standard deviation is about 1.5%–2% in band-3 and 1.0%–1.5% in band-4 to the exception of region with low transmittance corresponding to higher standard deviation values.

The overall relative bias between the three considered instruments and the corresponding simulations restricting viewing and illumination angles to a maximum value of 40° is shown on Figure 93. The relative bias slightly differs according to the radiometer but remains below $\pm 1\%$ in most of the spectral regions.

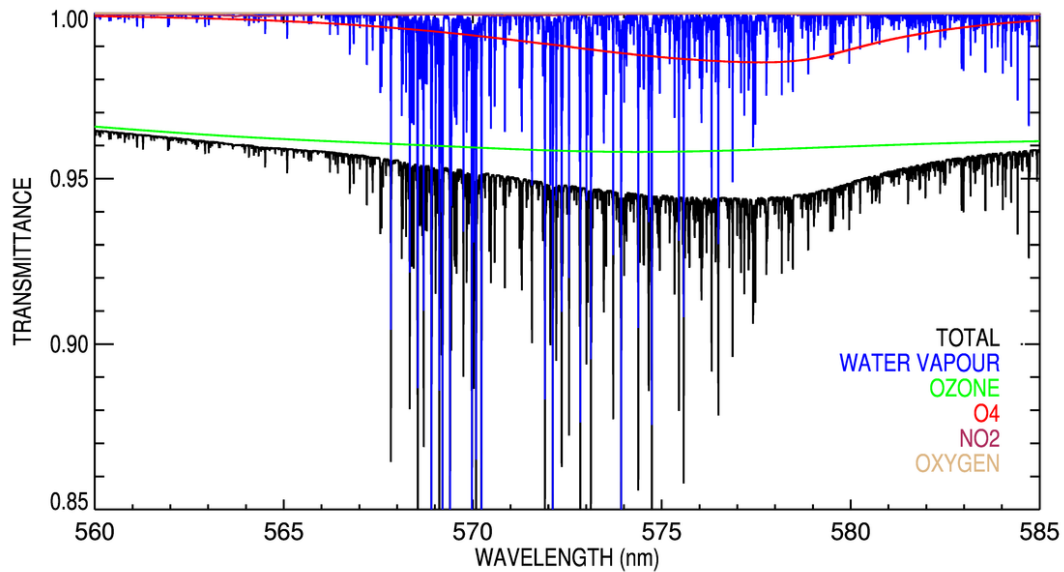


Figure 92: Details of molecular transmittance in the 560 – 585nm spectral interval.

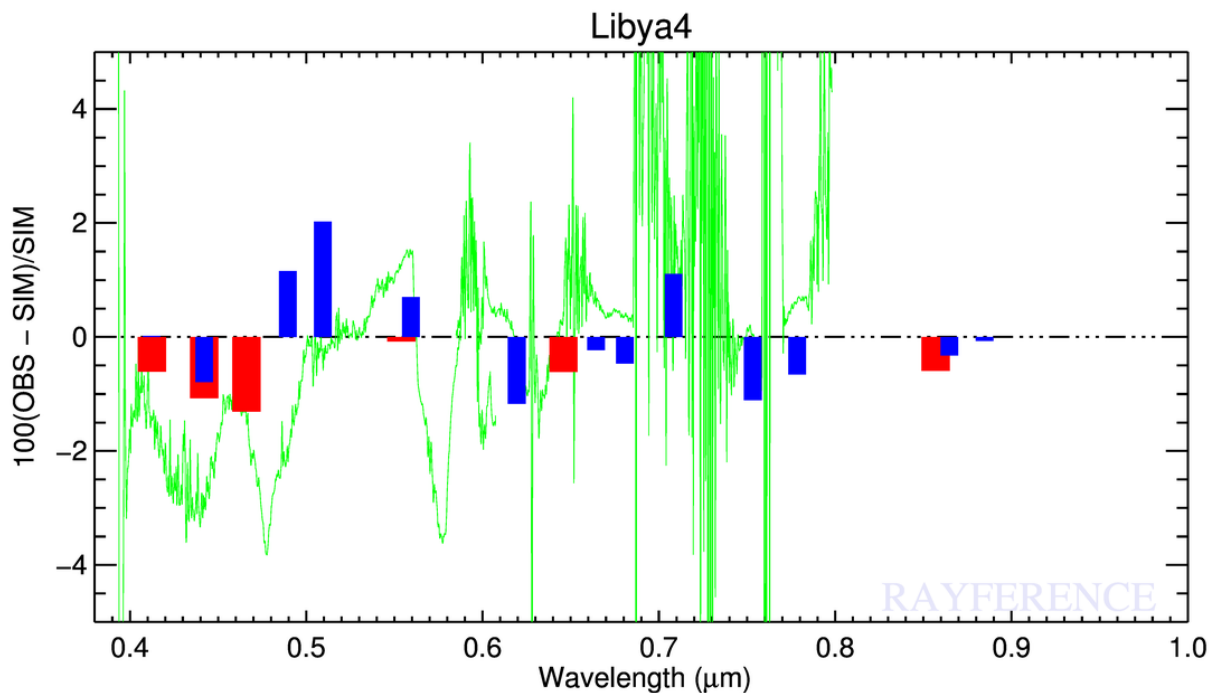


Figure 93: Overall relative bias between observations and simulations for MODIS (red), MERIS (blue) AND GOME-2b (green). Illumination and viewing zenith angles are restricted to a maximum value of 40° .

6.3.3. Results

For the purpose of this comparison, a 5-day Meteosat-10 period has been processed covering the 116 – 120 time frame in year 2003. Results are shown in Figure 94 and Table 6-4. The slope of the DC – simulated TOA radiance regression line provide the overall calibration coefficient for this period and the X-axis intercept an estimation of the space count. As can be seen from Table 6-4, there is a very good agreement between results obtained of DCC and Libya-4. Values derived over sea slightly exceed values derived over the two other target types, particularly in bands VIS0.6 and VIS0.8. This might indicate that the residual optical thickness used in SSCC is too large, leading to too high simulated TOA radiances. This discrepancy will be further discussed in Section (8).

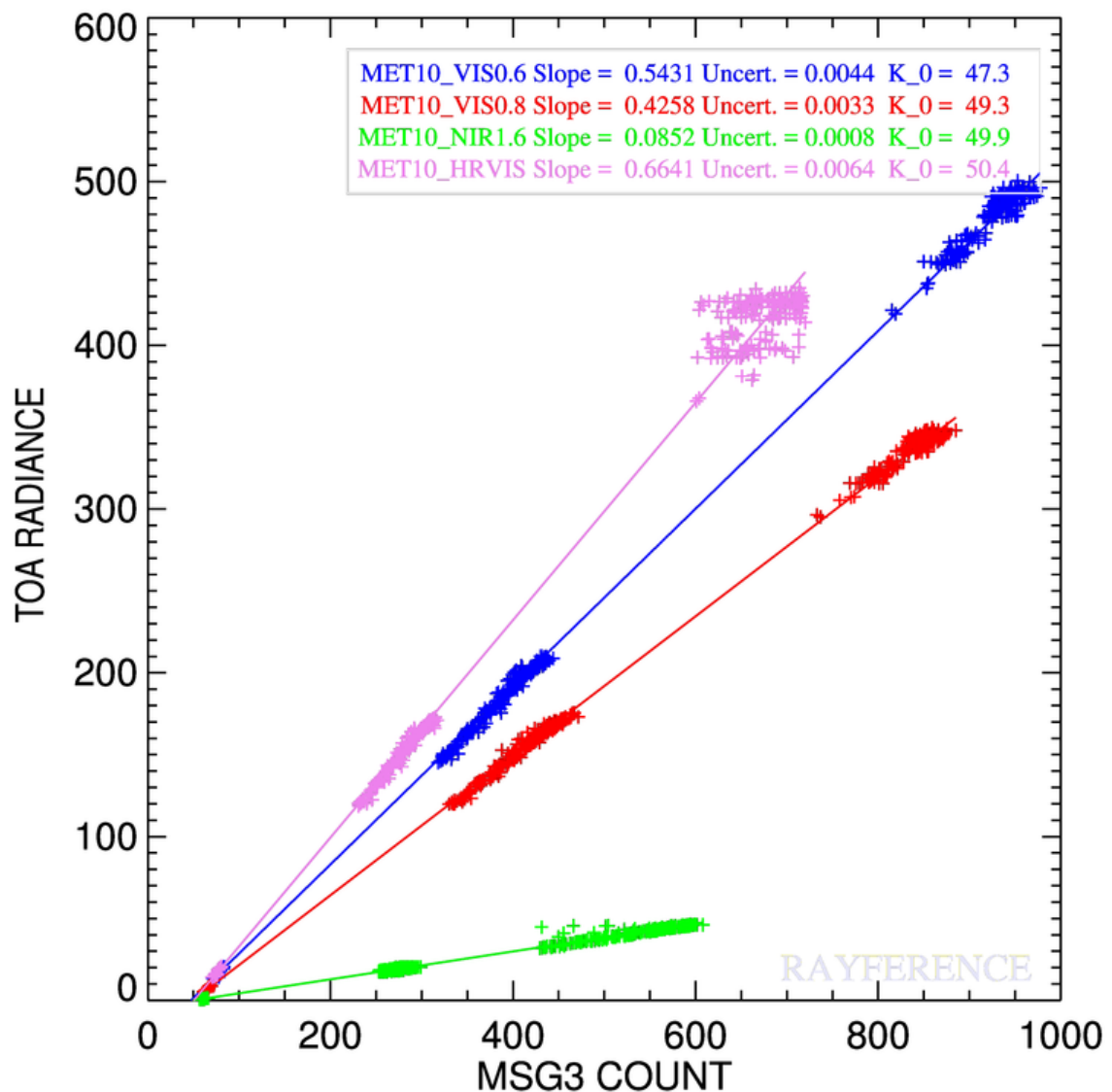


Figure 94 – Example of overall scatterplot of MSG3 count values against simulated radiances in band VIS0.6 (blue), VIS0.8 (green), NIR1.6 (green) and HRVIS (violet) for Meteosat-10 in 2003 for day-of-the-year 116-120. The slope provides the calibration coefficient expressed in $Wm^{-2}\mu m^{-1}sr^{-1}/DC$ over sea, Libya-4 and DCC. In the NIR band, count values over Libya-4 exceed the DCC values.

Table 6-4 – Comparison of DCC calibration results derived of sea, Libya-4 and DCC for Meteosat-10 in 2013 for day-of-the-year 116-120. Calibration coefficients are given in $\text{Wm}^{-2}\mu\text{m}^{-1}\text{sr}^{-1}/\text{DC}$. The offset column provides the retrieved space count value.

Band	Sea	Libya-4	DCC	Slope	Slope Uncert.	Offset	Offset Uncert.
VIS0.6	0.5992	0.5464	0.5454	0.5431	0.0044	47.30	0.597
VIS0.8	0.4437	0.4263	0.4270	0.4258	0.0033	49.28	0.467
NIR1.6	0.0878	0.0854	0.0854	0.0852	0.0008	49.90	0.422
HRVIS	0.6590	0.6621	0.6683	0.6641	0.0064	50.37	0.704

7. TOWARDS INTEGRATION IN THE VICARIOUS CALIBRATION SYSTEM SSCC

The detailed description of the implementation of the proposed algorithm in SSCC has been described in an updated version ASD and will not be repeated in the report. Only the overall integration strategy is described. Figure 95 summarises the overall SSCC flowchart.

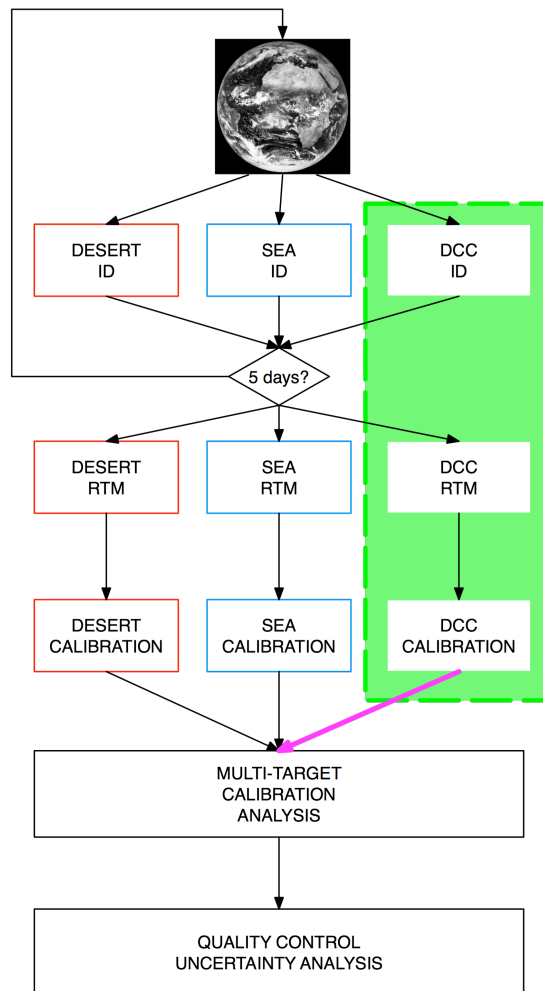


Figure 95: SSCC overall flowchart.

The green shaded area corresponds to the new module for the DCC processing. When a new image is processed, identification process over bright deserts, sea and DCC takes place during the 5-day accumulation period. During that period, potential DCC cloud identification process takes place, including the steps described in Section (4.1).

At the end of this 5-day period, the TOA radiances corresponding to the identified pixels are simulated. For DCC, these radiances are pre-computed in LUTs for each solar channel as a function of the SZA, VZA, RAA, COT, ice particle radius. Currently, it is not foreseen to include the total column ozone as a dimension of the LUT, though it might be worthwhile to foreseen this possibility.

The calibration coefficients derived over DCC are saved in order to be accumulated during a 30-day period. After this 30-day DCC accumulation period and when at least 3000 potential DCC pixels have been identified, the DCC multi-spectral histogram analysis is taking place. From the DCC pixels that successfully passed this last test, those belonging to the current SSCC 5-day period and extracted from the histogram for the multi-target calibration analysis (magenta arrow in Figure 95). The pixels older than 30 days are then removed from the histogram, keeping however at least 3000 pixels in the histogram.

The overall calibration coefficient in each spectral band is defined as the slope of the regression line as shown in Figure 94.

Finally, two methods are proposed for the estimation of the overall quality indicator:

- A first method based on an estimator for the common mean assuming that a common calibration coefficient mean is shared by all kinds of targets (sea, desert, DCCs over sea and DCCs over land) and can be estimated using the estimator of Graybill and Deal (1957).
- A second method based on the comparison of paired of calibration coefficients as currently performed in SSCC.

8. RECOMMENDATIONS AND WAY FORWARD

8.1. OVERVIEW

This report presents the use of DCC targets as the third calibration target as originally foreseen in SSCC. It has been seen that it is possible to derive calibration coefficients over DCC with an estimated uncertainty of about $\pm 1.5\%$ in the VIS0.6 and VIS0.8 channels and $\pm 3.0\%$ in the NIR1.6 and HRVIS bands. In the NIR1.6 band, this uncertainty might exceed this value during some period of the year.

As no access to SSCC was granted in the framework of this study, it has not been possible to perform tests on the integration of the DCC method in SSCC and to decide what would be the recommended method for the overall quality indicator and uncertainty estimation.

The recommendations are organised into three parts. The first one deals with additional sensitivity analysis on the DCC method that goes beyond the scope of this limited study. It essentially concerns the calibration of the NIR1.6 band, the effects of the molecular concentration above the DCC. The second category of recommendations concerns the integration of the DCC method within SSCC. The last one addresses potential future SSCC improvements that could be included in the framework of its adaptation to MTG/FCI.

8.2. FURTHER IMPROVEMENTS OF THE DCC METHOD

R01 : Adjustment of the daily time window. For the ZDS, the daily time range has been set to 10:00 – 14:00 UTH and 07:30 – 12:30 for the MSG1 IODC mission. These time ranges have been defined according to the nominal sub-satellite points with the idea to minimize the number of Meteosat images to order at the UMARF. It is however recommended to adjust this time range according to the actual location of the search area accounting for the eastern and western part of these areas. The impact of increasing this temporal range on the HRVIS band calibration should be investigated. In case enough DCC pixels can be identified, it is recommended to include this band in the multi-spectral filtering.

R02 : Cloud Optical Thickness. In the solar channels, COT is the most important parameter. The possible seasonal variation of this parameter might be investigated. However, it is not recommended to use Meteosat-derived product for the characterization of this parameter, unless this characterization essentially relies on IR channels

R03 : Micro-physical properties in band NIR1.6. This band is highly sensitive to the ice particle radius but also to the vertical structure of this parameter. Further analyses would be needed on this parameter to decrease the calibration of that band with DCC but also seasonal variations.

R04 : Cloud top height. The sensitivity to the cloud top height has been shown in Section (3.4.6.2). Lowering the cloud affects the radiance as it increases the amount of absorbing molecule above the cloud. The current study assumes a cloud top height fixed at 17km all year long. The benefit of using a tropopause height climatology might be explored in case there is need to decrease the uncertainty of the current method. Introducing a new parameter will increase the dimension of the LUTs and should therefore be considered carefully.

R05 : Atmospheric vertical profile. The current RM assumes a standard tropical vertical profile for the atmosphere. No sensitivities have been performed so far concerning this profile. The use of an actual temperature, pressure and humidity profile would prevent the use of LUTs for the DCC radiance estimation. It could be envisaged only if enough computing power can be dedicated to SSCC.

R06 : Molecular absorption above DCC. The influence of the molecular absorption above the DCC is closely related to the actual DCC height addressed in R04. The same conclusion concerning the increase of the LUT complexity should also be considered.

R07 : IODC data. Only 6 months of MSG1 data over the Indian Ocean have been processed due to the limited available time series. Recommendation R01 certainly applies in this case, particularly over the ocean search window.

8.3. INTEGRATION WITHIN SSCC

R10 : Estimation of the overall calibration coefficient. It has been recommended to use the slope of the regression line considering all valid pixels during a 5-day period as overall calibration coefficient in each band. It has not been possible to verify this recommendation, as it was not possible to run SSCC. Additionally, the current characterization of the desert targets provides an underestimation of the calibration coefficient, particularly in the VIS0.6 band. This type of target should therefore be improved first before including the DCC method into SSCC.

R11 : Estimation of the overall quality indicator. Two different methods have been proposed as overall quality indicator. As for R10, it has not been possible to evaluate these two methods in actual situation.

8.4. POTENTIAL SSCC IMPROVEMENTS

R20 : Improve desert BRF characterization. The characterization of the bright desert surface BRF has been performed in the early 2000 when only limited observation over these site where available. It should be the priority number one for the adaptation of SSCC to the calibration monitoring of MTG/FCI. Over Libya-4, it has been shown that an estimated uncertainty of $\pm 2\%$ can be reach on an annual basis. A further decrease of this uncertainty would require the use of 3D radiative transfer modelling.

R21 : Improve sea pixel identification. Calibration coefficients derived over sea are still subject to a very height uncertainty. The identification mechanism should be revisited following a similar multi-spectral histogram analysis as for DCC including also an updated characterization of the aerosol optical thickness.

R22 : Improve radiation transfer modelling. SSCC still relies on a pretty old version of 6S. It is therefore suggested to use a better RTM, including polarization and including gaseous transmittance calculation based on the latest version of HITRAN.

R23 : Multi-mission capabilities. It is highly recommended to keep the multi-mission capabilities of SSCC that secures the temporal consistency of the calibration among the various generations of the Meteosat missions. It is however recommended to include a new working modes in SSCC. The current working mode concerns the estimation of calibration coefficients of uncalibrated radiometers as MVIRI and SEVIRI. The second one concerns the monitoring of calibrated instruments such as the OLCI or STSTR radiometers. It would allow to compare SSCC reference simulations against these radiometers.

R24 : Uncertainty propagation. Uncertainty estimation has been established neglecting the cross terms. In the context of FIDUCEO, the importance of the non-diagonal terms concerning the uncertainty of the sensor spectral response characterization plays an important role.